Vibration characterization of an active magnetic bearing supported rotor

J. Bean

20266332

Dissertation submitted in fulfilment of the requirements for the degree *Master of Engineering in Mechanical Engineering* at the Potchefstroom campus of the North-West University

Supervisor: Prof. G. van Schoor
Co- supervisor: Mr. N. Bessinger

Month and year: November 2011

Declaration

I, the undersigned, hereby declare that the work done in this project is my own original work.

.....

Jaco Bean

18 November 2011

Potchefstroom

Summary

The McTronX Research group at the Potchefstroom campus of the North-West University, aims to establish a knowledge base on active magnetic bearing (AMB) systems. Up to date, the group has established a firm knowledge base on various topics related to AMB systems. A recent focus was the design and development of a high speed AMB supported rotor system called the rotor delevitation system (RDS) to analyse rotor drops. During the testing phase of the RDS, the machine exhibited vibrations, of which the origins were unknown.

The research presented in this dissertation sets out to characterize the vibrations of the RDS, which is the group's first attempt to fulfil the need for characterizing vibrations in an AMB supported rotor. Emphasis is placed on characterizing the natural response of the RDS rotor, stator and integrated system. The research project is defined in terms of four main objectives: rotor and stator characterization, modelling, system characterization and rotor dynamic diagnostics.

A comprehensive literature study introduces the fundamental concepts regarding vibrations of single and multiple degree of freedom systems. These concepts include; natural frequencies, damping, machine vibrations, rotor dynamics and modelling techniques. These modelling techniques are introduced to verify the experimental methodology used to determine the natural frequencies. A critical overview of the literature contextualises the theory with the research investigation.

For the RDS rotor and stator characterization, a modal analysis process also known as the "*bump test*" is implemented in order to validate the bending natural frequencies of the rotor and stator. A simulation model of the RDS is constructed in the finite element (FE) package *DyRoBeS*®. The model is verified with a numerical and an analytical model and validated with the measured bending natural frequencies of the RDS rotor. For the system characterization, a number of modal analysis processes are implemented, which validates the rigid body natural frequencies of the RDS. These frequencies are also used to validate the FE simulation. The origins of the synchronous vibration harmonics are verified by formulating and evaluating hypotheses according to different modal analysis processes.

From the RDS rotor modal analysis it was identified that a bending natural frequency of the rotor is situated at approximately 443.33 Hz. This was verified using the FE simulation model. During the system modal analyses, it was identified that only one rigid body natural frequency, situated at approximately 62 Hz, is excited. This frequency increases with the differential gain control parameter of the system up to approximately 140 Hz. After evaluating two hypotheses regarding the origins of the synchronous

vibrations harmonics, it was verified that non-circularity of the rotor at the measuring positions is the cause.

Overall the objectives of the study were addressed by characterizing the natural frequencies of the rotor, stator and RDS system. This include the mode forms of the rigid body and bending natural frequencies of the system. The results of the verification and validation methods correlated, which imply these methods are reliable to identify the origins of vibrations in rotor-bearing systems.

The differential gain control parameter of the AMBs control the equivalent damping in the RDS. An increase in this parameter should lead to a decrease in amplitude and frequency of the maximum vibration, and vice versa. However, it was noted that an increase in this parameter caused a linear increase in the rigid body natural frequency. The literature indicates that this effect can only be caused by an increase in system stiffness. It is therefore recommended to evaluate the stiffness of the system as a function of the differential gain control parameter.

Keywords: *Vibration characterization, active magnetic bearings, natural frequencies, rotor dynamics.*

Acknowledgements

I firstly want to thank our heavenly Father for the mercy and strength bestowed upon me.

I would also like to acknowledge the following people for their contributions during the course of this dissertation:

- Karina Buys for her love, patience, understanding and never-ending support,
- Attie, Marieta and Hanno Bean for their love and support,
- Prof. George van Schoor for his guidance, advise and support,
- Jannik Bessinger and Jan Janse van Rensburg for their guidance, advise and support,
- Angelique Combrinck for her time spent on editing this dissertation,
- McTronX research group colleagues for their friendship, support, advise and laboratory assistance.

Table of contents

List of figures

List of tables

List of abbreviations

AAMB	Axial active magnetic bearing
ACC	Accelerometer
ADES	AMB drive electronic system
AMB	Active magnetic bearing
BD	Blower disc
CM	Centre of mass
FE	Finite element
FFT	Fast Fourier transform
IM	Induction motor
KE	Kinetic energy
PBMR	Pebble bed modular reactor
PE	Potential energy
RAMB	Radial active magnetic bearing
RDS	Rotor delevitation system
SDOF	Single degree of freedom
TD	Thrust disc
TDOF	Two degree of freedom

Chapter 1 Introduction

1.1 Background

From as early as the first musical instruments, people became interested in the theory of vibrations. String instruments, such as harps, were even found in Egyptian tombs from about 3000 B.C. Musicians and philosophers formulated rules and laws regarding the production of sound. These laws were used to improve their instruments and were passed down from generation to generation. From these laws some of the fundamental concepts related to the theory of vibrations, as understood today, were formulated [1].

Vibrations form part of everyday life and can either be beneficial or detrimental. This can be noted in nature as well as engineering. The orb web spider utilises vibrations to locate its pray after being trapped in the web, whereas earthquakes can cause damage to structures. Most engineering applications experience vibrations in a detrimental manner, for example the failure of the Tacoma Narrows Bridge in 1940 [2].

Vibration characterization has become standard procedure in the design and development of engineering systems due to the devastating effects that vibrations can have on machines and structures. The effective characterization of machine or structure vibrations results in increased machine or structure life, as well as greater energy transmission or efficiency [3].

Machine vibrations can be divided into three main categories: free (natural), forced and self-excited vibrations. Free vibration occurs in the absence of external forces. Forced vibration is caused by externally induced forces continually supplying energy to a system. Self-excited vibration refers to periodic and deterministic oscillations, where the exciting force is independent of the vibration [1]. By dividing machine vibrations into the three main categories, it is possible to determine if the vibrations can be eliminated or if the vibrations are inherent to the machine.

Lateral or bending vibrations of shafts and rotors, caused by unbalance, form the most critical aspect of modern day machine vibrations [4]. Machines utilising rotors or shafts consist of bearings separating the rotating parts from the stationary parts, and are referred to as rotor-bearing systems. Figure 1-1 illustrates a typical rotor-bearing system with radial bearings at the rotor ends and an unbalance mass at the centre of the rotor.

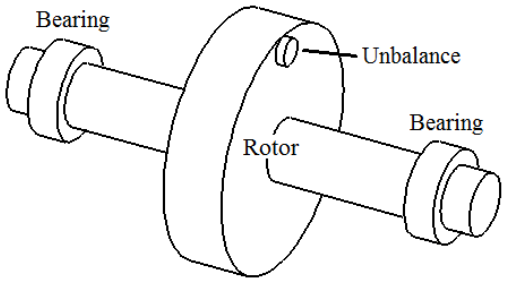

Figure 1-1: Rotor-bearing system with unbalance

The unbalance machine vibrations can be compared to a child swinging a rock tied to a string as illustrated in Figure 1-2 [5]. As the child swings the rock above his head, a centrifugal force, created by the rotating rock, pulls his hand. The child induces a reaction force, keeping the rock on the circular path.

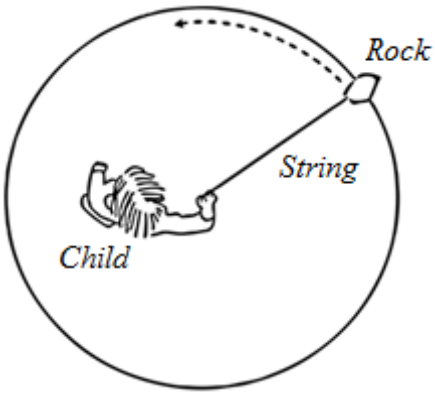

Figure 1-2: Child swinging a rock [5]

If the circular path of the rock is replaced with the rotor, illustrated in Figure 1-1, the rock becomes the unbalance of the rotor. Rotation of the rotor then induces a rotating centrifugal force on the bearing. The rotation of the unbalance force results in a bearing deflection[1], and vibration ensues.

The engineering application of rotor-bearing systems comprise numerous configurations. All of these configurations have two things in common: rotors and bearings. Typical bearings include journal bearings, roller element bearings and active magnetic bearings. Each bearing has certain advantages and disadvantages which make them suitable for specific applications. Active magnetic bearings are typically used in high speed, non-lubricated and high temperature applications.

[1] All materials have an elestic property and deflects under an applied load [9].

1.1.1 Active magnetic bearings

Active magnetic bearings (AMBs) work on the principle of suspending a mass by means of a magnetic force. By using AMBs in rotor bearing applications, contact between the rotating and stationary parts is prevented. Advantages of AMBs include [6]:

- frictionless operation,
- high rotational speeds, and
- manipulation of rotor dynamics.

A simplified model describing the operation of an AMB can be seen in Figure 1-3. The sensor measures the error in the position of the rotor relative to the reference position. The controller then derives and sends an error-based control signal to the power amplifier which generates the corresponding control current in the electromagnet. A force is then applied by the electromagnet which corrects the position of the rotor [6].

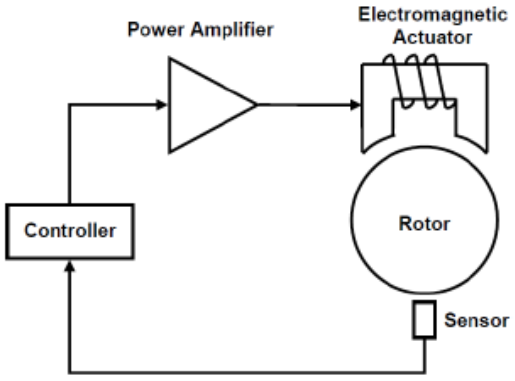

Figure 1-3: Simplified AMB model [6]

1.1.2 Rotor delevitation system

The McTronX research group of the North-West University designed and manufactured a rotor-bearing system called the rotor delevitation system (RDS). The RDS uses AMBs to suspend a rotor. The system is based on a helium circulator that operates at a rotational speed of 25,500 r/min. Due to budget constraints, the operational speed of the RDS was limited to 19,000 r/min.

The aims of the RDS project were the adaptation of a rotor for AMB levitation, as well as the corresponding auxiliary bearing design for safe delevitation of the rotor, in the event of an AMB failure. Overall, the two aims of the RDS project were successfully accomplished. From the vibration analysis, some discrepancies between the simulated and measured results were noted [7]. The discrepancies can be summarised as:

- The frequency of the first bending mode of the RDS rotor was experimentally measured to be 30 Hz above the theoretically simulated frequency,
- an experimental steady-state harmonic analysis was performed and two unaccounted for natural frequencies were observed at approximately 100 Hz and 140 Hz, and
- a cascade plot of the RDS rotor was constructed, which identified a number of synchronous vibration harmonics of unknown origin.

1.2 Problem statement

The purpose of this project is the vibration characterization of an active magnetic bearing supported rotor system. Emphasis is placed on characterizing the natural response of the RDS rotor, stator and integrated system.

A simulation model of the RDS needs to be constructed in a computer software package in order to simulate the natural response of the RDS rotor and integrated system. Operational vibrations need to be characterized by implementing a rotor dynamic diagnostic procedure on the RDS. Alterations on the system will not form part of this study because the RDS is a high precision machine.

The problem statement can be summarised in four main objectives as illustrated in Figure 1-4. Each of these objectives has its own sub-problems and limitations.

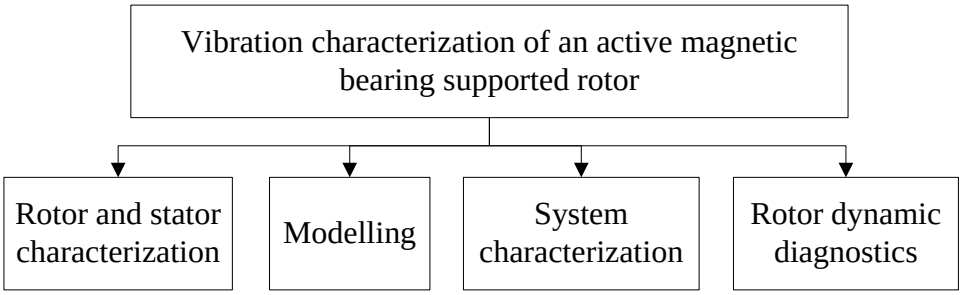

Figure 1-4: Project breakdown

1.3 Objectives and methodology

The objectives are defined from the project statement as a rotor and stator natural response investigation, modelling of the RDS rotor and integrated system, an investigation into the response of the integrated system and a rotor dynamic diagnostic process.

1.3.1 Rotor and stator characterization

The characterization of the RDS rotor and stator natural response includes the natural frequencies of the rotor and stator as well as the mode forms of the rotor.

The natural frequencies of the rotor and stator will be characterized by implementing a vibration analysis technique known as a "*bump test*". The mode forms of the rotor will be identified by scaling the bump test data and sketching the mode forms by comparing the phase angles of the data.

1.3.2 Modelling

In order to verify the mode forms of the experimentally characterized natural frequencies, a simulation model of the RDS rotor has to be constructed to simulate the mode forms of the rotor. The simulation model should also be able to simulate the bearing specifications of the integrated RDS. The simulation model has to be verified in terms of the rotor and bearing stiffness.

A finite element (FE) simulation model of the RDS will be constructed in the computer software package *DyRoBeS*® by incorporating the geometric measures and material properties of the rotor assembly in the package. The model will then be verified in terms of rotor stiffness by comparing the first bending natural frequency of the simulation model to the fundamental frequency (first bending natural frequency) approximated by conventional beam theory and Rayleigh's energy method. The experimentally measured natural frequencies and mode forms of the RDS rotor will then be verified by comparing the results of the bump test to the simulated results.

The RDS bearing specifications will then be included in the simulation model in order to simulate the integrated natural frequencies. The integrated model will then be verified in terms of bearing stiffness by comparing the rigid body natural frequencies of the simulation model to the rigid body natural frequencies approximated by a two degree of freedom (TDOF) analytical model.

1.3.3 System characterization

The integrated RDS natural frequencies, which might not have been identified by the rotor and stator natural frequencies, need to be experimentally identified. This includes the rigid body natural frequencies of the RDS.

The natural frequencies will be identified by implementing the bump test on the integrated RDS. The frequencies will then be verified by comparing the experimental results to the simulated results of the RDS FE model.

1.3.4 Rotor dynamic diagnostics

The origins of the synchronous harmonic vibrations present during operation, have to be characterized according to relevant literature.

The origins of the harmonics will be characterized by implementing a rotor dynamic diagnostic procedure, formulating hypotheses identifying the origins of the harmonics and evaluating these hypotheses. This process will be repeated until the origins of the harmonics are identified.

1.4 Dissertation overview

Chapter 2 provides a literature study regarding the necessary theory to conduct the research project. The literature study constitutes vibration concepts, damped vibration, active magnetic bearings, rotor dynamics and rotor dynamic diagnostics.

Chapter 3 covers the RDS rotor and stator natural response investigation. The chapter commences with the validation of the geometric and material properties of the RDS rotor. The procedure that is used to statically determine the bending natural frequencies of the rotor and stator, as well as the results are also discussed in this chapter.

Chapter 4 explains a FE simulation model of the RDS. The numerical and analytical models used to verify the RDS FE model are also included in this chapter. The chapter concludes with the verification of the experimental rotor natural response and a summary of the model results.

Chapter 5 provides the characterization of the integrated RDS system. The procedure that is used to determine the integrated RDS system natural frequencies, as well as the results are discussed. The integrated RDS natural frequencies are also verified using the RDS FE simulation model. The chapter concludes with a rotor dynamic diagnostic procedure used for characterizing rotor dynamic phenomena or faults. Hypotheses regarding the system vibrations are formulated and evaluated. The test procedures used to evaluate the hypotheses, as well as the results and verification of the hypotheses are discussed.

Chapter 6 concludes the dissertation by summarising the findings made from the research project as well as the effectiveness of the procedure that was used to characterize the vibrations on the RDS. Recommendations are also made for further research on the RDS.

Chapter 2 Literature study

This chapter aims to provide the reader with the literature needed to characterize vibrations in AMB supported rotors. Concepts throughout the chapter include: natural frequencies, damping, mode forms, rotor dynamics, active magnetic bearings and rotor dynamic diagnostics. The chapter concludes with a critical overview of the literature to contextualise the theory.

2.1 Vibration

Any motion repeating itself after a time period is called a vibration or oscillation. The motion is a result of the continuous interchange between kinetic and potential energy. Consider a mass, m, supported by a linear-elastic spring, with stiffness k, as illustrated in Figure 2-1(a). As the system vibrates the mass compresses the spring to the position in Figure 2-1(b), where the total system energy is stored in the spring (potential energy)[2]. The mass then accelerates to the unloaded position of the spring, Figure 2-1(c), where the total system energy is fully transferred into speed of the mass (kinetic energy)[3]. Passing the unloaded position, the mass alternatively stretches the spring to the position in Figure 2-1(b), where the total system energy is again stored in the spring (potential energy) [1].

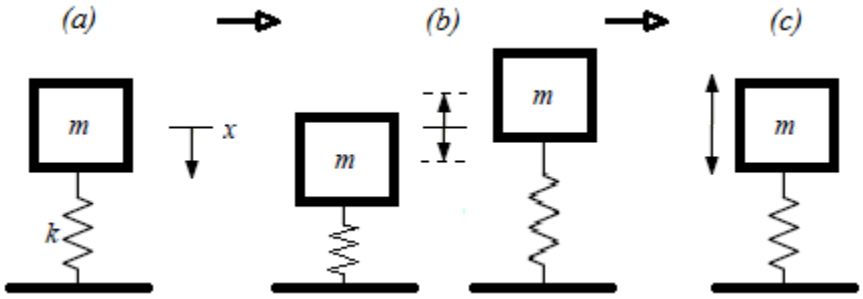

Figure 2-1: (a) Mass-spring system with x the plane of motion, (b) system orientation of maximum compressed and stretched spring, (c) system orientation of maximum mass speed

All matter can be approximated by the system illustrated in Figure 2-1(a), sharing two common characteristics: a mass and elastic property. For this reason, all systems exhibit the ability to vibrate and every vibrating system has a number of natural frequencies [8].

[2] Potenial energy (PE) is energy resulting from an elastic member (elastic PE) or elevated state (gravitational PE) [8].
[3] Kinetic energy (KE) is energy resulting from the motion of an object (velocity) [8].

2.1.1 Natural frequency

The term natural frequency can be defined as the frequency at which a system oscillates after an initial disturbance without any external forces [1]. This frequency requires great attention as the vibration amplitude is exaggerated when a system operates near or at a natural frequency [8]. As mentioned in section 1.1, the process of characterizing system natural frequencies has become inevitable. Modern vibration theory eases the process of identifying natural frequencies.

The characterization process can be primarily discussed using the system illustrated in Figure 2-1(a). The differential equation governing the response of the system to an initial displacement disturbance can be written as [1]:

$$m\ddot{x} + kx = 0 \tag{2-1}$$

where $\ddot{x}$ denotes the acceleration of the system vibration. Solving the governing equation results in the natural frequency ω_n given by [1]:

$$\omega_n = \sqrt{\frac{k}{m}} \tag{2-2}$$

If the system in Figure 2-1(a) is subjected to a harmonic force[4], as illustrated in Figure 2-2, external energy is supplied to the system. The governing equation (2-1) becomes invalid because of this external force [1].

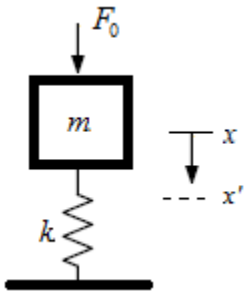

Figure 2-2: Mass-spring system subjected to harmonic force

The differential equation governing the response of the system to the harmonic force can be redefined from (2-1) as [1]:

$$m\ddot{x} + kx = F_0 \cos(\omega t) \tag{2-3}$$

[4] A sinusoidal force having a frequency that is an integral multiple of the frequency of a periodic force to which it is related [8].

where F_0 denotes the maximum force amplitude and ω denotes the frequency at which the force is applied. The natural frequency of the system remains the same as defined in (2-2). After solving the differential equation, the maximum vibration amplitude of the system can be defined as [1]:

$$X = \frac{\delta_{st}}{1-\left(\frac{\omega}{\omega_n}\right)^2} \tag{2-4}$$

where $\delta_{st} = F_0/k$ is the static deflection of the system under the force F_0. If the force frequency ω coincides with the natural frequency ω_n of the system, the denominator will be zero and the vibration amplitude will be infinite. In most practical systems, vibrations gradually decay over a certain time period because kinetic or potential energy dissipates into other forms of energy. This phenomenon is referred to as damping [1].

2.1.2 Damping

All systems exhibit an amount of damping. The consideration of damping is crucial for the accurate prediction of vibration response in dynamic systems. Characterizing damping in dynamic systems can become quite tedious for complex systems. Therefore, it is important to first understand the origin of the damping mechanism, to choose a suitable damping model and finally to determine the damping values (model parameters) [9]. The three primary forms of damping mechanisms include [1]:

- Internal or material damping[5],
- coulomb or dry friction damping[6], and
- viscous or fluid damping[7].

In some dynamic systems, external damping elements are included to improve the damping characteristics of the system. These extra damping elements can be divided into two groups: passive dampers, and active dampers. Passive dampers supply extra damping to a system through means of motion without utilising an external power source or actuator. Active dampers on the other hand, function on the principle of controlling the motion of a system by using power supplied by an external source [9].

[5] Energy dissipation within the material due to friction between the internal planes [1].
[6] Energy dissipation caused by the the relative motion of components in a machanical structure that have common points of contact [8].
[7] Energy dissapation due to drag forces and associated dynamic interactions when a machanical structure moves in a fluid [8].

For simplified mathematical modelling of damping in a dynamic system, an equivalent viscous damping term is usually used [9]. Referring back to Figure 2-2, if damping is included in the system, the differential equation governing the response of the system becomes [1]:

$$m\ddot{x} + c\dot{x} + kx = F_0 \cos(\omega t) \tag{2-5}$$

where c denotes the equivalent damping of the system and $\dot{x}$ denotes the velocity of the system vibration. The damped frequency of vibration for the free vibrating system can be defined from (2-2) as [1]:

$$\omega_d = \sqrt{1-\zeta^2}\,\omega_n \tag{2-6}$$

where $\zeta = \frac{c}{2m\omega_n}$ is the damping ratio of the system. The maximum vibration amplitude of the damped system to the harmonic force can be defined as [1]:

$$X = \frac{\delta_{st}}{\left\{\left[1-\left(\frac{\omega}{\omega_n}\right)^2\right]^2 + \left[2\zeta\frac{\omega}{\omega_n}\right]^2\right\}^{1/2}} \tag{2-7}$$

From (2-7) it should be clear that the vibration amplitude will be finite when the harmonic force frequency coincides with the natural frequency, unlike in (2-4) [1]. This may seem beneficial to the system, but the force transmitted to the foundation is still the same. It is therefore good practice to avoid natural frequencies [7].

Equation (2-5) defines damping in a system as velocity-dependent. As the frequency of the excitation force increases, the velocity increases and finally the damping also increases. A reaction force, resulting from a combination of the stiffness and damping of the system aims to isolate the foundation from transferred vibration, induced by the excitation force. The system reaction force to the excitation can be described with a dynamic stiffness term as:

$$k_{dynamic} = \frac{F_0}{X} \tag{2-8}$$

The dynamic stiffness can be illustrated by considering the system shown in Figure 2-2 with the information given in Table 2-1.

Table 2-1: Single degree of freedom system information

m	k	c	F_0
2 kg	20 000 N/m	200 N/m	$0.001\omega^2$ N

As the frequency of the excitation force varies, the dynamic stiffness of the system also varies. This phenomenon can be seen in Figure 2-3 illustrating the dynamic stiffness as a function of excitation force frequency. The receptance of the system describes the ratio between the transmitted vibration to the applied force as a function of frequency [9]. The receptance curve of the system will thus be the inverse of Figure 2-3 and is illustrated in Figure 2-4.

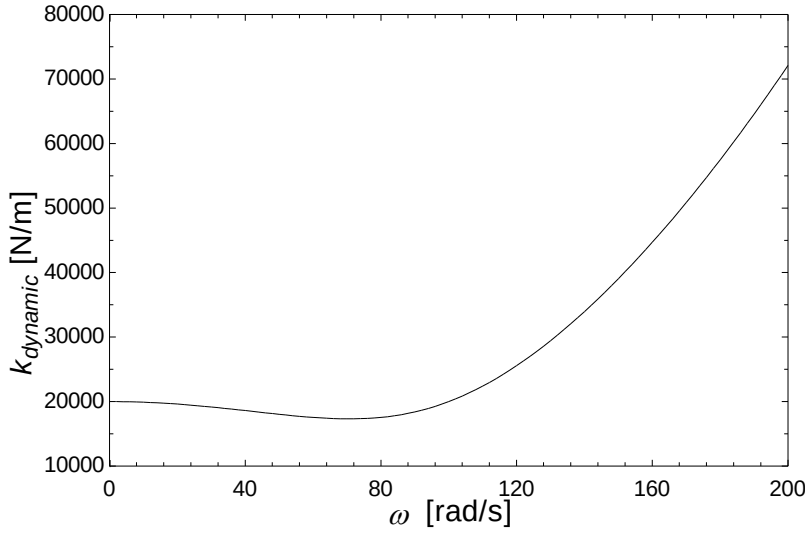

Figure 2-3: Dynamic stiffness as a function of excitation force frequency for the system in Figure 2-2 with damping

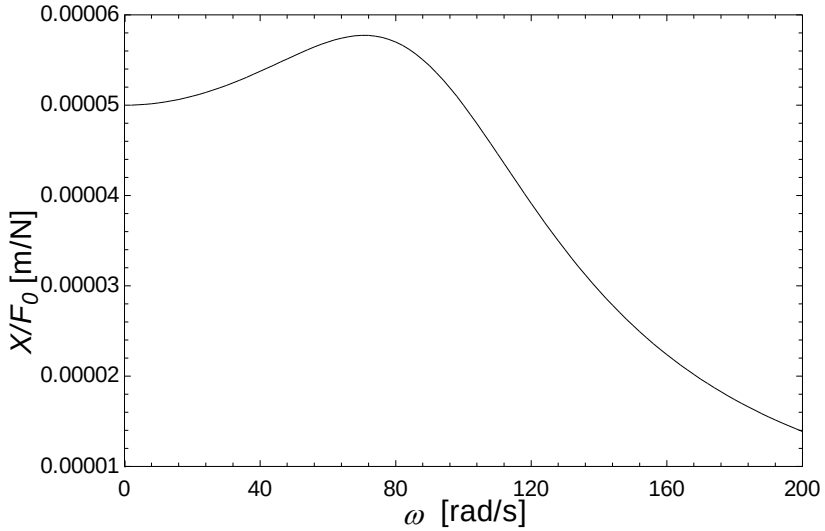

Figure 2-4: Receptance as a function of excitation force frequency for the system in Figure 2-2 with damping

The estimation of damping values can be a very complex process. Damping in systems usually arises from a combination of the three forms of damping. The overall damping value is generally not equal to the sum of the individual damping values when acting independently. It is however acceptable to assume linear viscous damping when estimating damping in systems [9].

2.1.3 Damping measurement

Damping can generally be estimated by either using a time-response or a frequency-response record of the system vibration. Estimation methods associated with the time-response record include the logarithmic decrement method and the step response method. Estimation methods associated with the frequency-response record include the magnification factor method and bandwidth method [9]. These methods are discussed in the following sub-sections.

2.1.3.1 Logarithmic decrement method

When a damped system is excited using an impulse excitation, its time-response takes the form of a time decay as illustrated in Figure 2-5 [9].

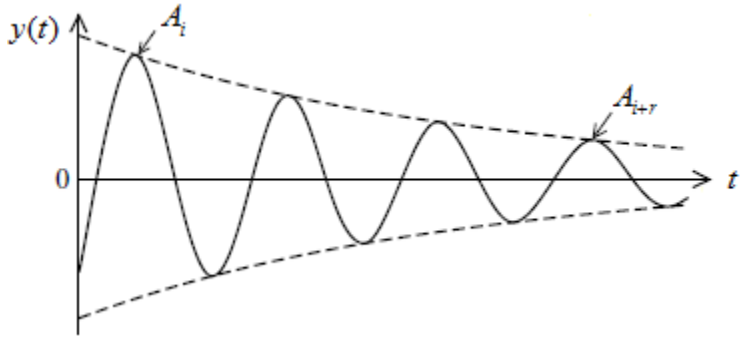

Figure 2-5: Time-response record of damped system to impulse excitation [9]

If it is assumed that A_i represents the amplitude of a peak noted in the time-response at a time interval and A_{i+r} represents the amplitude of a peak noted r cycles[8] later in the time-response, the logarithmic decrement of the system δ can be defined as [9]:

$$\delta = \frac{1}{r}\ln\left(\frac{A_i}{A_{i+r}}\right) \tag{2-9}$$

[8] One cycle of a vibrating system refers to the oscillation of the body from its undisturbed state to its extreme state (maximum PE), back to its equilibriam (maximum KE), then to its extreme state in the opposite direction (maximum PE), back to its equilibrium position (maximum KE) [1].

From the logarithmic decrement, the damping ratio ζ of the system can be defined as [9]:

$$\zeta = \frac{1}{\sqrt{1+\left(2\pi/\delta\right)^2}} \tag{2-10}$$

This method is considered as the most popular time-response method used to estimate damping of a system [9].

2.1.3.2 Step response method

The response of a damped system to a unit step excitation is illustrated in Figure 2-6, where M_p is the response at peak time, T_p [9].

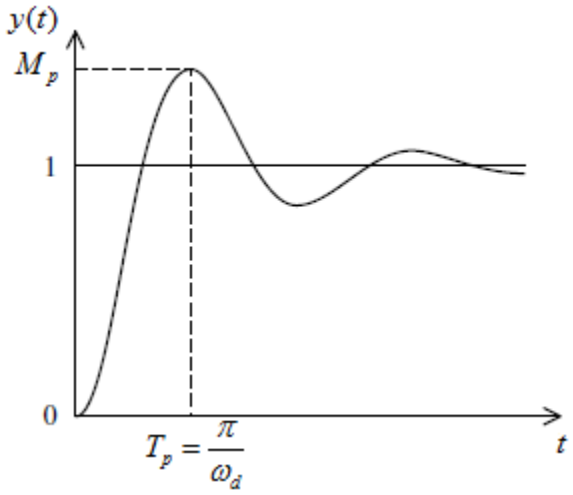

Figure 2-6: Time-response record of damped system to unit step excitation [9]

The percentage overshoot of the response is given by [9]:

$$PO = \left(M_p - 1\right) \times 100\% \tag{2-11}$$

If any of the parameters M_p, T_p or PO is known, the damping ratio of the system can be estimated as [9]:

$$\zeta = \sqrt{1-\left(\frac{\pi}{T_p\omega_n}\right)^2} = \frac{1}{\sqrt{1+\frac{1}{\left[\frac{\ln\left(M_p-1\right)}{\pi}\right]^2}}} = \frac{1}{\sqrt{1+\frac{1}{\left[\frac{\ln\left(PO/100\right)}{\pi}\right]^2}}} \quad (2\text{-}12)$$

2.1.3.3 Magnification factor method

The frequency-response of a system to an excitation is illustrated in Figure 2-7, where Q represents the magnification factor and ω_r represents the frequency of frequency-response at the resonance frequency [9].

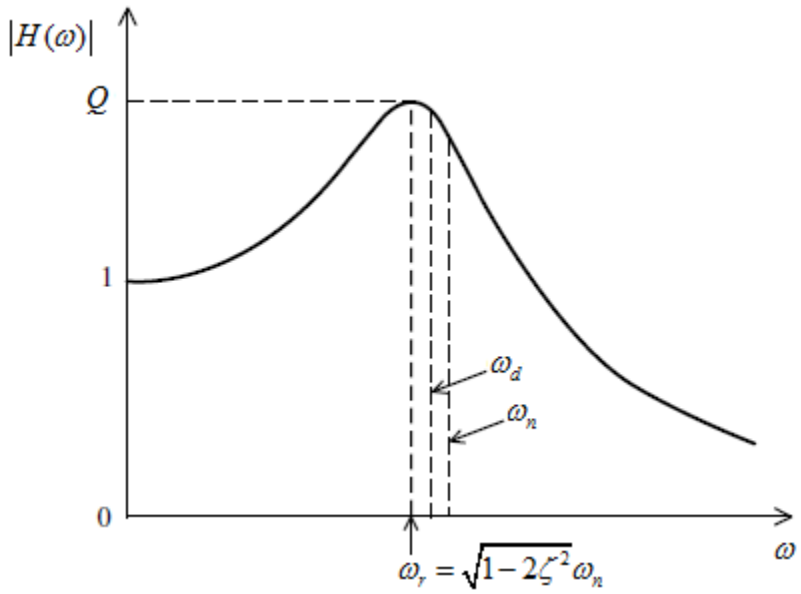

Figure 2-7: Frequency-response record of damped system to an excitation [9]

The magnification factor of the system can be defined in terms of the damping ratio of the system as [9]:

$$Q = \frac{1}{2\zeta\sqrt{1-\zeta^2}} \tag{2-13}$$

This equation can be used to estimate the damping ratio of the system, given that the magnification factor is known.

2.1.3.4 Bandwidth method

Consider the frequency-response record illustrated in Figure 2-7. If Q represents the magnitude of the frequency-response at the resonance frequency ω_r, then ω_1 and ω_2 represents the frequencies at which the frequency-response magnitude is $\frac{Q}{\sqrt{2}}$, as illustrated in Figure 2-8 [9].

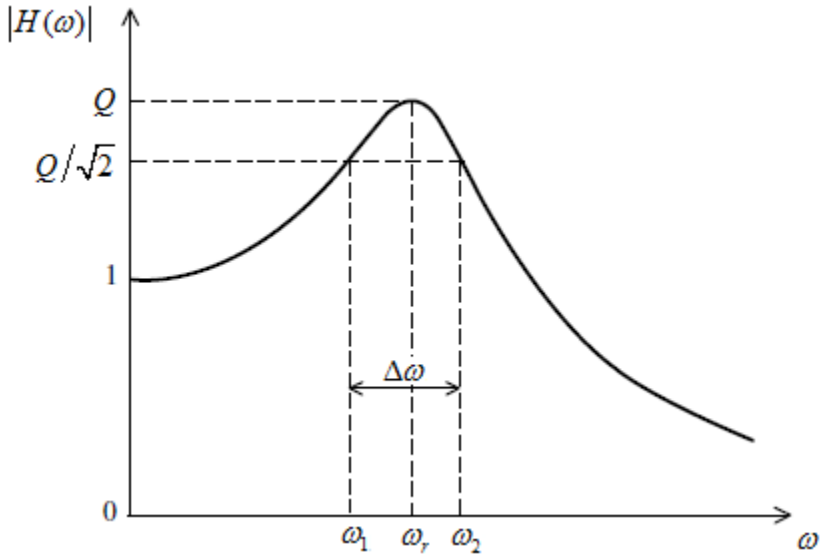

Figure 2-8: Frequency-response record of damped system to an excitation [9]

The damping ratio of the system can be estimated by using the bandwidth, $\Delta\omega = \omega_2 - \omega_1$, of the frequency-response as [9]:

$$\zeta = \frac{\Delta\omega}{2\omega_r} \tag{2-14}$$

Systems as illustrated in Figure 2-1(a) and Figure 2-2 are called single-degree-of-freedom (SDOF) systems since only a single motion is considered, the translation motion in the vertical plane. The number of natural frequencies related to a system is directly proportional to the number of degrees-of-freedom used to describe the response of the system. For this reason SDOF systems contain only one natural frequency. The literature discussed so far also apply to systems with more degrees-of-freedom. A rotor-bearing system is a typical example of a system with more degrees-of-freedom [1].

2.2 Vibrations in turbomachinery

Rotor-bearing systems, also referred to as turbomachinery, experience vibrations axially, laterally and torsionally [10]. The response of turbomachinery is excitation-dependent. For example, when dynamically analysing the vibrations of a tractor drive shaft or gearbox, torsional vibrations are considered. The reason being the torsional forces transferred by the drive shaft or gears in the gearbox [7].

High speed turbomachinery, such as turbines and blowers, are concerned with lateral vibrations [11]. Lateral forces induced by the unbalance of the rotor excite vibrations in the system. Referring back to Figure 1-1, and looking from an axial point of view, Figure 2-9 illustrates the unbalance rotation of a rotor. The force created by the mass unbalance can be defined as [12]:

$$F_u = me\omega^2 \tag{2-15}$$

where F_u is the unbalance force, m is the mass of the rotor, e is the eccentricity of the centre of mass C_M to the geometric centre C_G and ω is the rotating speed of the rotor [12].

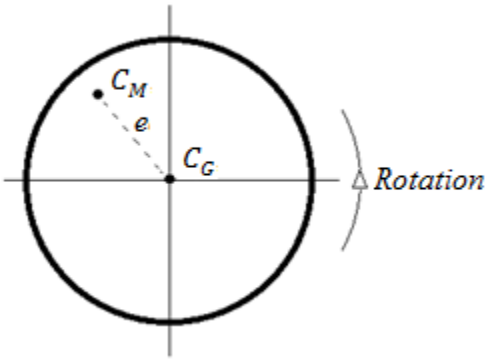

Figure 2-9: Illustration of rotor unbalance

From (2-15) it is clear that the unbalance force increases exponentially as the speed of the rotor increases. High speed turbomachinery experience excessive lateral vibrations as the speed of the system increases. The analysis of vibrations in rotating machines is usually referred to as rotor dynamics [13].

2.3 Rotor dynamics

Rotor-bearing systems are continuous systems consisting of an infinite number of degrees-of-freedom, unlike the systems shown in Figure 2-1(a) and Figure 2-2 [1]. This results in rotor-bearing systems having an infinite number of natural frequencies, with each a specific mode form. However, only a few are taken into consideration when designing or analysing a system. Modern rotor-bearing systems are designed to

operate at speeds that are sufficiently spaced from any natural frequency of the system. Natural frequencies outside the bandwidth of the operating speed are neglected [3].

The mode form of a natural frequency is the deflection curve of the system at the natural frequency [8]. The first two mode forms are referred to as rigid body modes and are illustrated in Figure 2-10. These two mode forms are simply dependent on the bearing stiffness since the rotor is considered as rigid compared to the stiffness of the bearings [10].

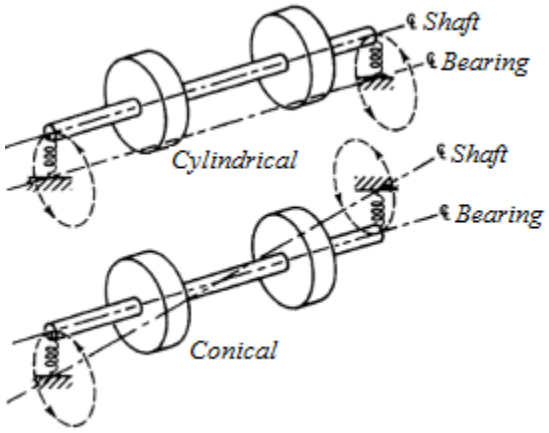

Figure 2-10: Rigid body modes [10]

Similar to all mechanical systems, rotor-bearing systems also exhibit damping. With reference to (2-15), the unbalance force increases as the speed of the system increases. As the system reaches sufficient speed, the bearing reaction stiffness becomes infinite according to Figure 2-3. The flexibility stiffness of the rotor stays constant. At speeds where the reaction stiffness of the bearings becomes greater than the stiffness of the rotor, the unbalance force tends to bend the rotor rather than compressing or elongating the bearings. Natural frequencies, dependent on the stiffness of the rotor, are known as bending natural frequencies. Figure 2-11 illustrates the bending mode forms of the first two bending natural frequencies for a rotor-bearing system [14].

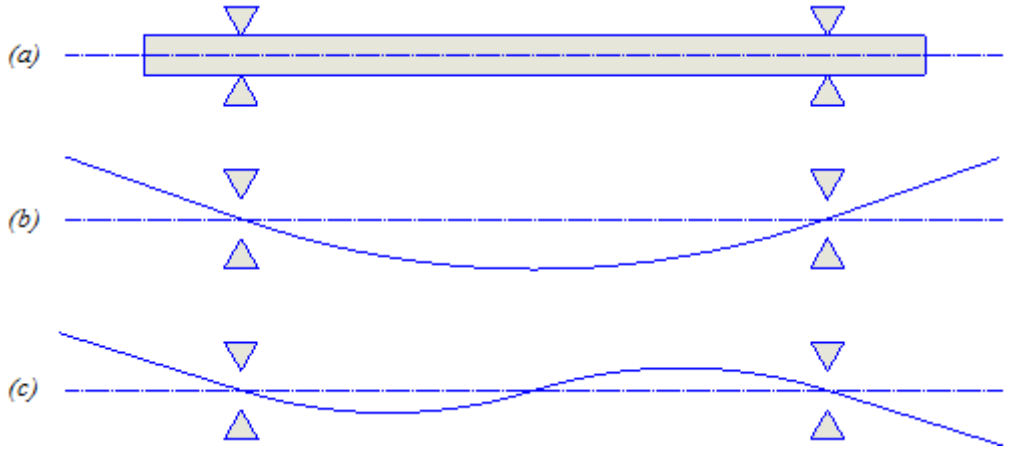

Figure 2-11: First two bending mode forms of a rotor-bearing system. (a) Rotor-bearing system with rigid supports, (b) first bending mode form, (c) second bending mode form [14]

The difference between rigid body modes and bending modes can be summarised by comparing the effect of bearing stiffness on the natural frequencies, as illustrated in Figure 2-12 [11]. From the figure, a variation in bearing stiffness results in different rigid body natural frequencies, although the bending natural frequencies stay constant.

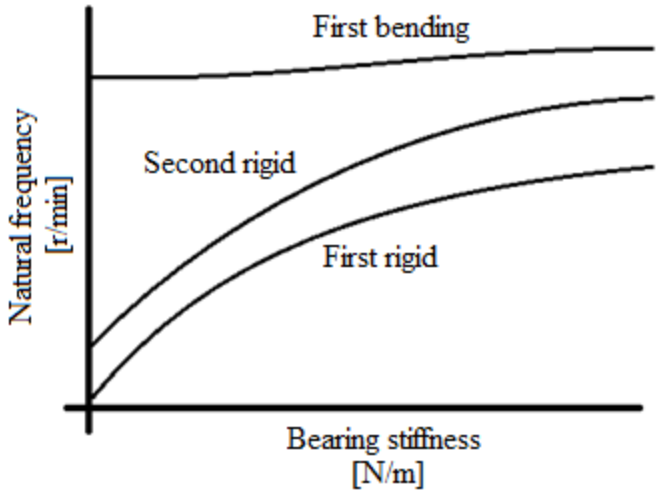

Figure 2-12: Effect of bearing stiffness on natural modes [11]

Bearing technology directly influences rotor dynamics, as illustrated in Figure 2-12, for example. Bearing technology has advanced immensely during the last few years. Various types of bearings have been developed each with its own advantages, disadvantages and applications. Typical high speed rotor-bearing systems utilise roller element bearings, oil film bearings or active magnetic bearings.

2.4 Active magnetic bearings

Section 1.1 presented the working principle and advantages of AMBs in rotor bearing systems. Figure 1-3 also illustrated the typical layout of an AMB. In terms of bearing properties, AMBs do not share the same characteristics as most conventional bearings. Figure 2-13(b) illustrates the nonlinearity in the force-position relation of AMBs, compared to the linearity of conventional roller-element bearings shown in Figure 2-13(a) [6].

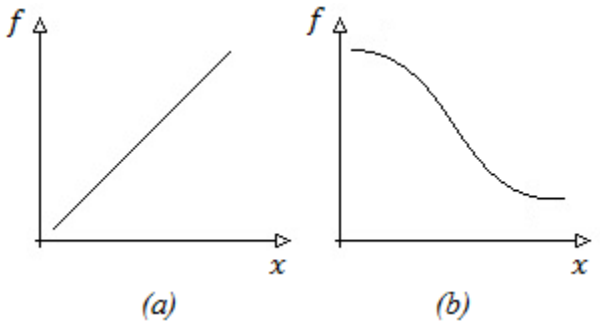

Figure 2-13: Force-position relation of (a) conventional bearings, (b) AMBs [6]

In order to design a rotor-bearing system utilising AMBs, the force-position relation of AMBs are linearized by taking a tangent slope k_s to the nonlinear relation as illustrated in Figure 2-14 [6]. If A represents the operating point of the AMB, it is clear that for an increase in vibration of the system the error in the force-position relation increase. Analysis of these system vibrations therefore become inevitable.

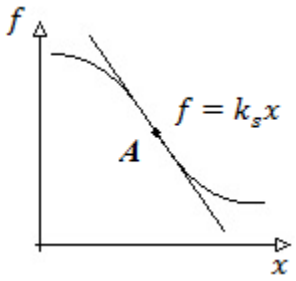

Figure 2-14: Linearized force-position of AMB for rotor-bearing design [6]

2.5 Modelling techniques

Rotor-AMB systems can become quite complex due to the material properties required and the layout of these systems. Numerous analytical and numerical techniques have been developed to assist in the vibration analysis of rotor-bearing systems. Most of these techniques approximate a continuous system as a discrete system[9].

[9] A discrete or lumped parameter system is a system with a finite number of degrees-of-freedom [1].

Typical techniques include:

- Finite element method,
- Rayleigh's energy method, and
- two-degree-of-freedom (TDOF) method.

2.5.1 Finite element method

The finite element method is a numerical method used for solving governing differential equations. The method is based on replacing an actual system with several elements interconnected at certain points, while assuming each of the elements behave as a continuous structural member called a *finite element*. A convenient approximate solution to the differential equations governing the elements is then determined. The solutions of the elements can be made to converge, by reducing the element size, to the solution of the actual system[10] [1].

This method is usually incorporated into a computer package to reduce computational time and reduce calculation errors. *DyRoBeS*® is a computer software package which uses the finite element method for complete rotor dynamic analysis and bearing performance calculations. The name of the package *DyRoBeS*® is derived from the phrase *Dynamics of Rotor-Bearing Systems* [15].

2.5.2 Rayleigh's energy method

Rayleigh's energy method is a numerical method based on the continuous interchange between kinetic and potential energy of the rotor. The method gives an estimated value of the first bending natural frequency, also known as the fundamental frequency, of a discrete system [1]. If a rotor-bearing system is approximated as a pin-supported beam with acting forces, as illustrated in Figure 2-15, Rayleigh's method defines the first bending natural frequency as [16]:

$$\omega_n^2 \simeq g \frac{\sum Wy}{\sum Wy^2} \tag{2-16}$$

where g denotes the gravitational constant, W denotes the forces acting on the beam and y the deflection of the beam at the positions of the acting forces.

[10] Refer to [1] for detail discription on the finite element method.

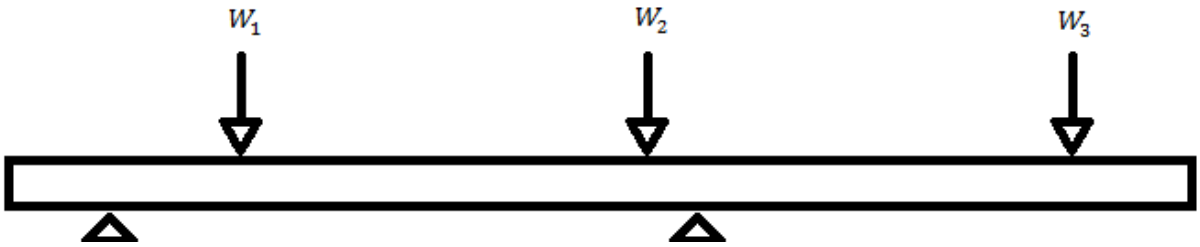

Figure 2-15: Rayleigh's approximation of a rotor-bearing system as a pin-supported beam with acting forces

2.5.3 TDOF method

The TDOF method is an analytical method describing the response of a rotor-bearing system with the translational and rotational motion of the centre of mass of the system. For illustration purposes, consider the lateral view of a simple rotor-bearing system, as illustrated in Figure 2-16. The system consists of a rotor with mass m_{eq}, mass moment of inertia J_{eq}, and two bearings with stiffness k_1 and k_2 situated at positions l_1 and l_2 from the centre of mass CM of the system [1].

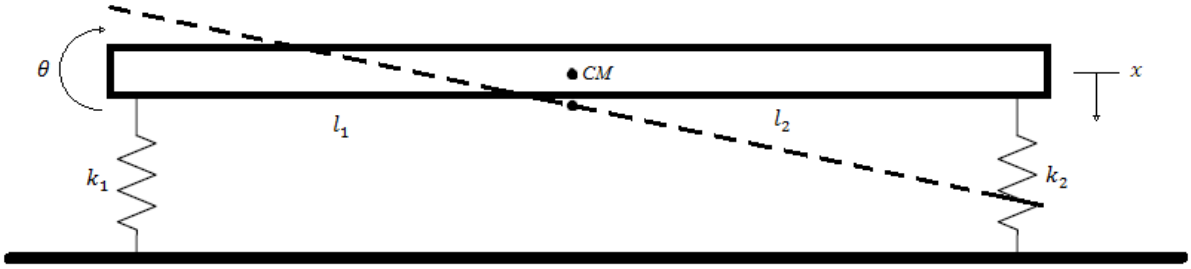

Figure 2-16: Two degree of freedom system approach

The equations of motion, describing the translation and rotation motion of the rotor to an initial translation disturbance, can be defined as [1]:

$$\begin{aligned} m_{eq}\ddot{x} + k_1\left(x - \theta l_1\right) + k_2\left(x + \theta l_2\right) &= 0 \\ J_{eq}\ddot{\theta} - k_1\left(x - \theta l_1\right)l_1 + k_2\left(x + \theta l_2\right)l_2 &= 0 \end{aligned} \tag{2-17}$$

where x and θ are the translation and rotation motion respectively and $\ddot{x}$ and $\ddot{\theta}$ are the translation and rotation acceleration respectively. If it is assumed that m_{eq} and J_{eq} have harmonic motions, the response of C_m can then be defined as [1]:

$$\begin{aligned} x(t) &= X\cos(\omega t) \\ \theta(t) &= \Theta\cos(\omega t) \end{aligned} \tag{2-18}$$

The translation and rotational acceleration can be defined from (2-18) as [1]:

$$\ddot{x} = \frac{d^2}{dt^2} x(t) = -\omega^2 \cdot \left(X \cos(\omega t) \right)$$
$$\ddot{\theta} = \frac{d^2}{dt^2} \theta(t) = -\omega^2 \cdot \left(\Theta \cos(\omega t) \right) \quad (2\text{-}19)$$

Rearranging (2-17) and using the definition of (2-19), the response of the system can be written in matrix form as:

$$\begin{bmatrix} \left(-m_{eq}\omega^2 + k_1 + k_2\right) & \left(-k_1 l_1 + k_2 l_2\right) \\ \left(-k_1 l_1 + k_2 l_2\right) & \left(-J_{eq}\omega^2 + k_1 l_1^2 + k_2 l_2^2\right) \end{bmatrix} \begin{Bmatrix} X \\ \Theta \end{Bmatrix} = \begin{Bmatrix} 0 \\ 0 \end{Bmatrix} \quad (2\text{-}20)$$

The rigid body natural frequencies of the rotor-bearing system, illustrated in Figure 2-16, can be calculated by setting the determinant of (2-20) equal to zero and solving the equation [1].

The three methods discussed in sections 2.5.1, 2.5.2 and 2.5.3 are summarised in Table 2-2, by comparing the capability of each method to simulate the natural frequencies of a rotor-bearing system.

Table 2-2: Mode form calculation capabilities of vibration analysis techniques

Method	Rigid body natural frequencies	Bending natural frequencies
Finite element method	Yes	Yes
Rayleigh's energy method	No	Yes
TDOF method	Yes	No

2.6 **Rotor dynamic diagnostics**

According to [12], the reliability of present day rotating systems are more crucial than ever. Due to the evolution in engineering and material science, rotor-bearing systems become lighter, operate at higher speeds and for longer time periods. In most processing and manufacturing environments, approximately half of the operating costs are dedicated to maintenance [9]. In order to minimise maintenance costs, machine diagnostics through vibrations analysis are used to determine the health and identify any faults in machinery. Table 2-3 summarises some common rotor dynamic faults with their vibration characteristics.

Table 2-3: Common rotor dynamic faults with their vibration characteristics

Rotor dynamic fault:	Characteristics:
Bent shafts	Vibration components are noted in radial and axial direction. Axial vibrations may be higher than radial vibrations. Harmonics present in the vibration spectrum can be used to locate bent as [12]: • Dominant synchronous (1X rpm) vibration = bent in vicinity of rotor centre. • Dominant second synchronous harmonic (2X rpm) vibration = bent in vicinity of rotor ends.
Unbalance	For all types of unbalance induced vibrations, a prominent synchronous (1X rpm) vibration will dominate the vibration spectrum [12][3]. The unbalance can occur in a single plane (static unbalance) or in multiple planes (couple unbalance). A combination of these two are referred to as dynamic unbalance [12][10]. The unbalance results in a rotating vector force that occurs every once-per-cycle, producing the classic 1X rpm vibration [10].
Misalignment	Two types of misalignment can be defined [12]: • Angular misalignment: Shafts coupled with an angle between the centrelines. Typical characteristics include: high axial vibrations, high synchronous (1X rpm) vibrations with lower second synchronous harmonic (2X rpm) vibrations. Coupling faults are usually misidentified with angular misalignment. • Parallel misalignment: Shafts coupled with parallel centrelines although a offset occurs between the centrelines. Typical characteristics include: high axial vibrations and large second synchronous harmonic (2X rpm) vibration [10]. Parallel misalignment are rarely encountered, but in the rare case that it is encountered it is usually in a combination of angular misalignment.
Looseness	Looseness almost always produce higher harmonics of the synchronous vibration (2X rpm, 3X rpm ,....). If the looseness is directional the vibration spectrum will vary for different radial angled measurements [10].
Electric fault	Electrical faults occur due to unequal electromagnetic force acting on the rotor or stator [12]. The unequal magnetic force is usually a result of: open or short

	windings of the rotor or stator. High synchronous (1X rpm) vibration amplitudes throughout the operating speed of rotor are expected. Response differs when electrical power is turned off.
Shaft cracks	The main principle during shaft cracks is that the shaft looses stiffness in the plane perpendicular to the crack [12]. Shaft cracks usually produce two effects [3][13]: • a bending stiffness reduction aligned with the shaft crack direction and • the shaft tends to bow corresponding to the crack direction. The first effect almost always produce a second (2X rpm) synchronous vibration harmonic, whereas the second effect produce a high synchronous (1X rpm) vibration [12][3]. Shaft cracks also produce different vibration spectra for different radial align measurements.
Rotor rubs	Rotor rubs are usually confused with mechanical looseness as these two faults produce the same symptoms. This rotor dynamic fault tends to excite one or more natural frequencies. If N is the operating speed of a rotor and Nc is a natural frequency of the system, rotor rubs may generate frequencies of [12]: • 1X when N < Nc, • ½ X or 1X when N > 2Nc, • 1/3 X, ½ X or 1X when N > 3Nc, and • ¼ X, 1/3 X, ½ X or 1X when N > 4Nc.
Resonance	Resonance is typically diagnosed as systems operating at "*critical speeds*". These frequencies correlate with the natural frequencies of a system. A sharp increase in the synchronous vibration (1X rpm) is measured with a definite shift in phase [13].
Non-circularity	This rotor dynamic fault arises from the non-circularity of rotors, where measurements are taken. Due to the periodic variation in the radius of the rotor, the measurements will measure a periodic variation in the air gap between the rotor and the sensing interface. Harmonics occur due to frequency components measured as multiples of the synchronous vibration. This fault can be identified by capturing the variation in the air gap between the rotor and the sensing interface [17].

2.7 **Rotor delevitation system**

Section 1.1 introduced a rotor-bearing system designed by the McTronX research group of the North-West University. The system, referred to as the RDS, is based on a helium circulator using AMBs to suspend a rotor up to a rotational speed of 19000 r/min.

Circulators are used in nuclear reactors to circulate coolants through the reactor. The high temperature helium-gas cooled nuclear reactor, called the Pebble Bed Modulator Reactor (PBMR), is a typical nuclear reactor design employing circulators. For this nuclear reactor design, the helium is circulated through the reactor into a heat exchanger, where steam is heated and passed through turbines driving power generators. The PBMR relies on a high amount of helium being circulated within the primary helium flow cycle. For this reason the circulators should be of high speed and should not contaminate the helium. The use of AMBs is thus essential [18].

A lateral cross section view of the RDS is illustrated in Figure 2-17. The cross section view clearly indicates the:

- Radial AMBs (RAMBs) used to suspend the rotor laterally,
- the axial AMB (AAMB) controlling the axial position of the rotor,
- the induction motor (IM) used to drive the rotor, and
- the blower disc serving as a dummy impeller.

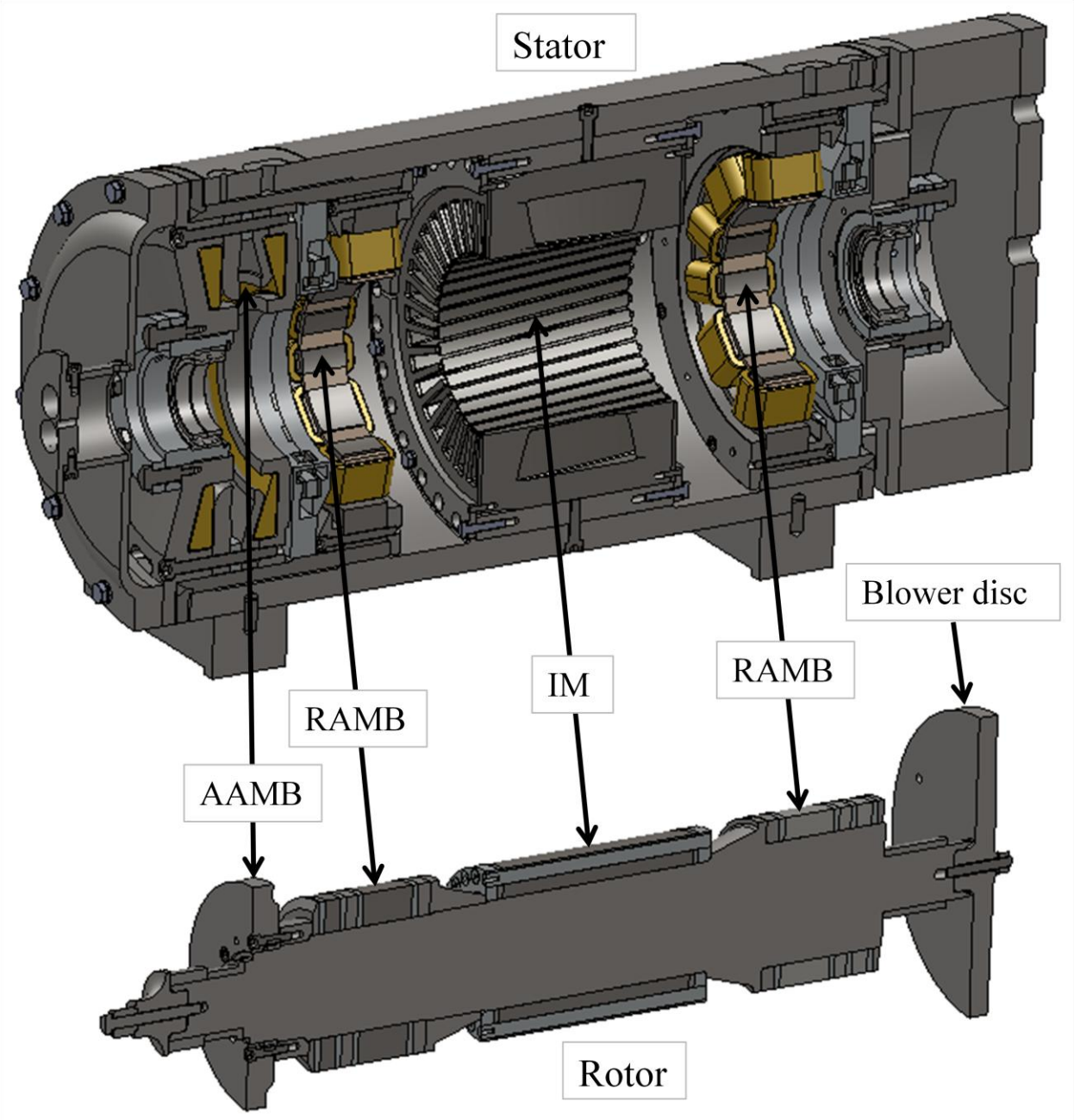

Figure 2-17: Lateral cross section view of the RDS

2.8 Critical literature overview

Throughout the course of Chapter 2, it became evident that the characterization of system vibration is a tedious and complex process. This process involves the consideration of numerous mechanical concepts. The purpose of this section is to contextualise the existing literature with respect to the research objective formulated for this study. From the problem statement it can be discerned that the theoretical aspects of the study include vibration characterization and rotor-AMB systems.

With reference to vibration characterization, the chapter commences with the fundamental concepts regarding vibrations discussed in section 2.1. The natural frequency characteristics of vibrating systems are introduced, followed by the implications of damping. Various techniques are introduced which are used to estimate damping in systems by either using time-response or frequency-response history of the vibration. As the effective vibration analysis of a system begins with an accurate time-response history of the system, it is decided that a time-response technique will be used for estimating damping [19]. The preferred method chosen was the logarithmic decrement method because this method is the most popular [9].

With respect to rotor-AMB systems, the chapter continued with an introduction into the field of machine vibrations and discussed the fundamental concepts regarding rotor dynamics. The literature defines machine vibrations as excitation dependent and therefore, only lateral rotor vibrations are considered for this research investigation. Axial and torsional vibrations will be ignored.

Three types of modelling techniques are introduced, which can be used to assist vibration analysis. As all three techniques approximate the system as a discrete system, it is decided to make use of all three models to improve the accuracy of the model.

The finite element model will form the primary model, as this model produces the most accurate approximation of the system. This is due to the number of finite elements that can be chosen by the analyser. The numerical model will only be used to verify the finite element model in terms of rotor stiffness, since this model approximates the system in a simplified manner. The analytical model will be used to verify the finite element model in terms of bearing stiffness, as this model approximates the actual system in two-degrees-of-freedom, whereas the actual system is continuous.

Section 0 presented some of the common rotor dynamic problems and their characteristics. Due to the physical layout of the RDS, some of these problems are irrelevant to the system. Bent shafts, misalignment and rotor rubs cannot produce harmonics of the synchronous speed in the RDS. The reason for this is due to the rotor not having any contact with the stator. According to [7], numerous harmonics

of the running speed vibration are excited, implying the rotor dynamic problems may include: looseness, electrical faults, shaft cracks and non-circularity. Due to the fact that most of the assembly components of the RDS rotor are shrunk fitted to the rotor, and that the RDS utilises AMBs, looseness and electrical problems will not be evaluated.

This chapter supplied the reader with a literature study regarding vibration characterization in AMB supported rotors. The chapter concluded with a critical overview placing the literature in context within the research aims of this dissertation. The next chapter provides the specifications needed to construct a simulation model of the RDS.

Chapter 3 Rotor and stator characterization

This chapter aims to provide the specifications needed to construct a simulation model of the RDS. The geometric measures and material properties of the rotor are validated, followed by the characterization of the natural frequencies and mode forms of the RDS rotor. The chapter concludes with the characterization of the RDS stator natural frequencies and remarks summarising the findings of the chapter.

3.1 Geometric and material properties

The only controllable parameters, defining a finite element simulation model of the RDS, are the geometric and material properties of a system. These parameters are essential to the accuracy and are validated using experimental results. Throughout this chapter it is evident that focus is primarily placed on the characterization of the RDS rotor. The reason for this is that rotor-bearing systems are concerned with the lateral vibrations of the rotor.

3.1.1 Rotor geometric measurements

The geometric measurements of the RDS rotor are validated by spot checking the documented measurements [7] through a number of random spot checks on the rotor. Figure 3-1 illustrates the positions randomly allocated for spot checking.

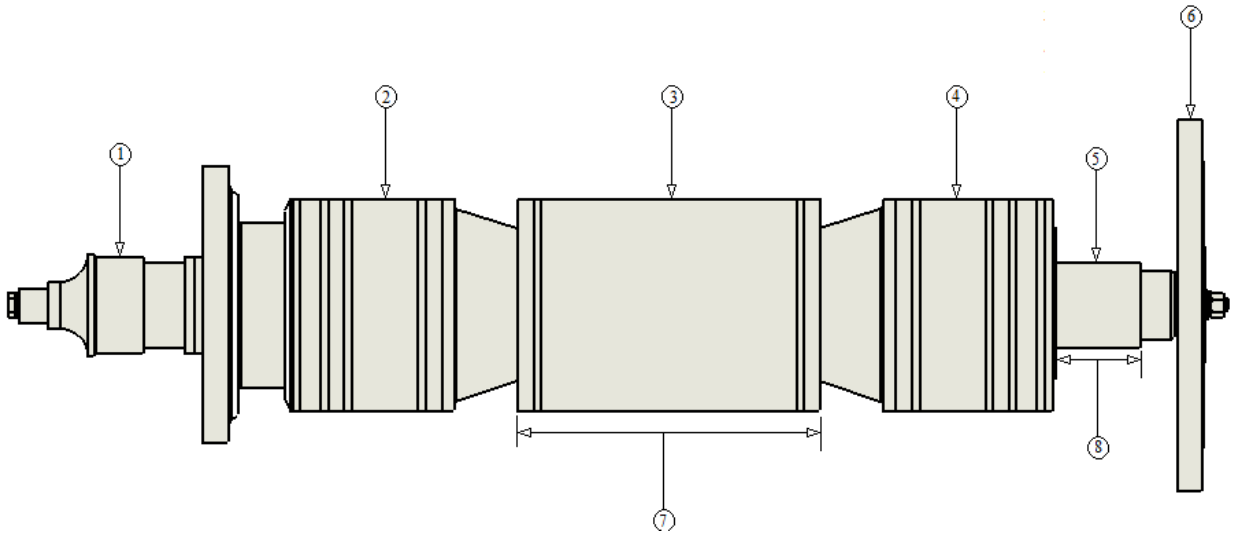

Figure 3-1: Positions for spot checking measurements on the RDS rotor

The spot checking measurements are taken with an AMNI-TECH 300x0.01 electronic digital calliper, which has an accuracy to the nearest 100^{th} of a millimetre. Table 3-1 summarises the documented and experimental measurements, as well as the error of the experimental measurements with respect to the documented measurements.

Table 3-1: Comparison between documented and spot measurements of the RDS rotor

Measuring station	Documented measurement [mm]	Spot measurement [mm]	Error %
1	56	55.88	0.21
2	123	122.93	0.03
3	123	123.17	0.14
4	123	123.06	0.05
5	49.7	49.71	0.02
6	216.5	216.43	0.03
7	50	50.33	0.66
8	177	176.96	0.02

Table 3-1 indicates that the documented measurements are validated by the experimental measurements and can be taken as reliable for constructing a simulation model. The documented measurements, used for spot checking the measurements, can be found in Appendix A.

3.1.2 Material properties

During the manufacturing process of the RDS, sample material of the different components was kept for testing purposes. The simulation model, presented in Chapter 4, utilise only the density, elastic and shear modulus of the materials and therefore only these properties are considered. The material densities of the sample materials are used to validate the documented material densities. The documented modulus of elasticity of the sample materials can however not be validated due to insufficient test equipment and budget constraints.

Figure 3-2 illustrates a lateral cross section view of the RDS rotor, colour coded according to the materials used to assemble the rotor. Table 3-2 summarises the documented and measured densities, as well as the error of the measured densities with respect to the documented densities.

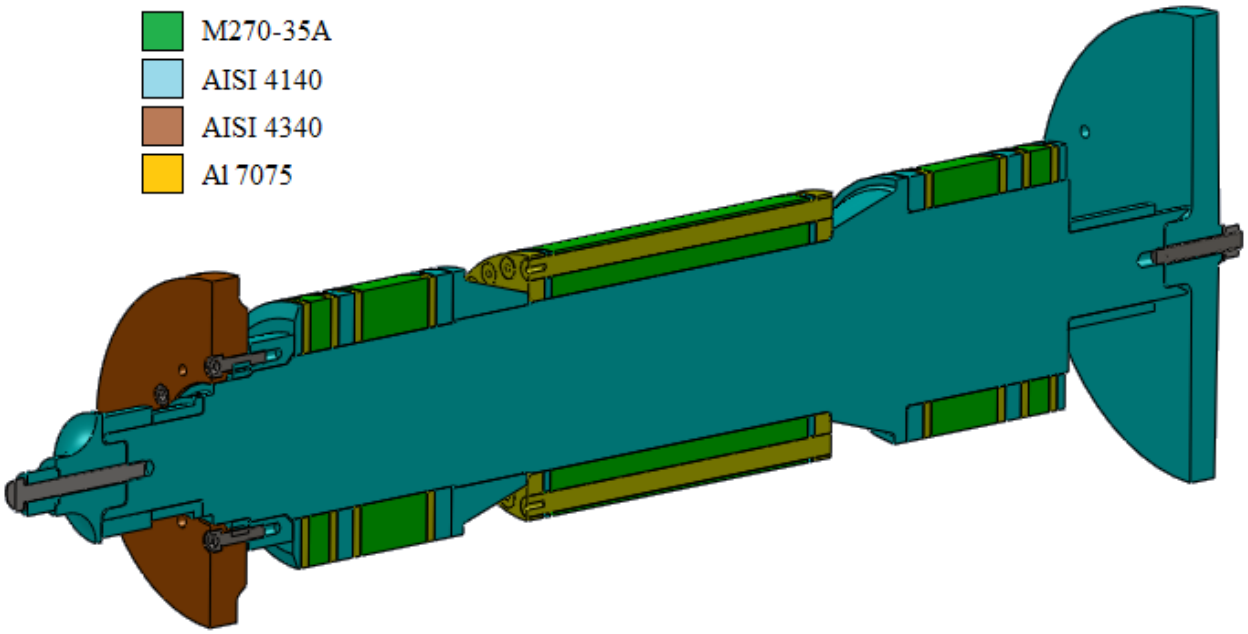

Figure 3-2: Lateral cross section view of the RDS rotor colour coded according to the four assembly materials

Table 3-2: Comparison between documented and measured material densities of the RDS rotor

RDS rotor components	Material	Documented density [kg/m^3]	Measured density [kg/m^3]	Error %
RDS rotor excluding: lamination packs, AAMB thrust runner, isolating spacers and IM rotor-bars	AISI4140 (En19) T-conditioned	7850	7857.5	0.10
AAMB thrust runner	AISI4340 (En24) T-conditioned	7850	7853.3	0.04
Isolating plates and IM-bars	Al7075-T6	2700	2698.8	0.04
Lamination packs	M270-35A	7650	6818.91	10.86

Table 3-2 indicates that the documented densities are validated and can be taken as reliable for constructing a simulation model. However, the material density of M270-35A has a significant error compared to the other materials. This is as a result of the structure of the material.

The M270-35A material is used for lamination sheets on the RDS rotor, for electromagnetic purposes and thus has a complex composition. The sheets consist of a thin layer of ferrous steel, isolated on both sides

with a silicon-based coating. The sheets have a nominal thickness of 0.35 mm and a thickness deviation of ± 0.03 mm [20].

3.2 RDS rotor modal analysis

Determining the bending natural frequencies of a rotor is an excellent way to test the accuracy of a simulation model [10]. The influence of bearing stiffness is prevented by using this technique. As mentioned previously, a rotor-bearing system has an infinite number of natural frequencies. When a rotor freely vibrates, the different vibration frequencies superimpose into one resultant system vibration.

The resultant system vibration can however be decomposed into the individual vibration signals. This can be done by calculating the Fast Fourier Transform (FFT) of the system vibration. Each of the decomposed vibration signals has a specific amplitude, phase and frequency. This method is used to identify the bending natural frequencies and mode forms of the RDS rotor [7].

The free vibration response of a rotor can be measured by hanging the rotor from slings attached to the roof, equipping the rotor with accelerometers and exciting the rotor horizontally with a soft hammer. The sling length should at least be one third of the rotor length to ensure negligible horizontal stiffness [10]. This procedure is also defined as the "*hammer / bump test*" [9].

3.2.1 Experimental procedure

As mentioned in section 2.3, the mode form of a natural frequency is the deflection curve of the system at the natural frequency. It is however impossible to identify the mode form of a system by measuring the response of the system at a single location [10].

Thirteen measuring stations are defined over the length of the rotor in order to experimentally identify the RDS rotor bending natural frequencies and mode forms. Since only four accelerometers are available for testing, the test procedure needs to be repeated in order to include all measuring stations. This is done by keeping two of the accelerometers stationary[11] and relocating the other two (floating[12]) accelerometers to different measuring stations. The tests are normalised by comparing the amplitudes of the stationary accelerometers for the different tests [10].

The test procedure is defined as [7]:

1. Suspend the rotor horizontally with slings hanging from the roof in order to eliminate any added stiffness to the rotor,

[11] The acceleromaters kept stationary throughout the model analysis are referred to as the stationary stations.
[12] The acceleromaters relocated to different measuring positions are referred to as floating stations.

2. excite the rotor horizontally by hitting the rotor with an object (preferably a plastic hammer to eliminate double tapping),
3. measure the response of the rotor with the accelerometers at the measuring stations,
4. calculate the FFT of each measured signal separately,
5. calculate the modulus of the complex FFT values,
6. construct the vibration spectrum of the rotor by plotting the modulus of the FFT values against frequency,
7. normalise the data for every test by using the modulus of the stationary accelerometers,
8. calculate the phase angles at the natural frequencies, and
9. calculate the mode form of the rotor at the natural frequencies.

3.2.2 Experimental setup

Figure 3-3 schematically illustrates the experimental setup for the rotor modal analysis [7]. Stations (1) and (13) are the stationary stations, for normalisation purposes, and stations (2) to (12) the floating stations. For illustration purposes the floating accelerometers are placed at stations (4) and (12).

From Figure 3-3 it should be clear that the thrust runner of the RDS rotor is removed from the rotor for the modal analysis tests. This is due to the disassembly possibility of the RDS. If the thrust runner of the RDS has to be disassembled from the stator, the AAMB section in the stator have to be disassembled. This means the calibration of the system can be jeopardised. For this reason, the thrust runner is disassembled from the rotor and left in the stator.

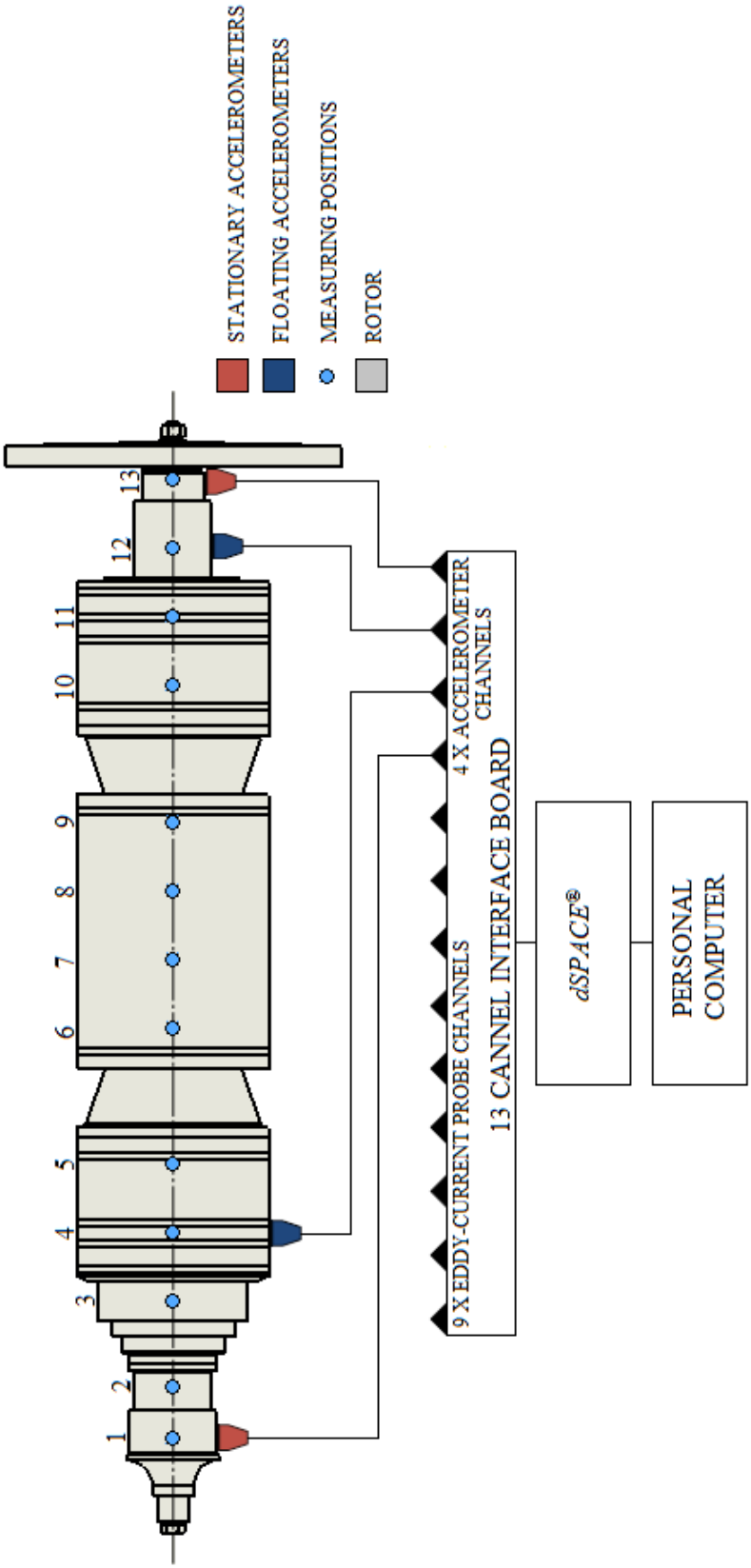

Figure 3-3: Schematic illustration of rotor modal analysis experimental setup

The axial position of measuring station (1) is taken as the zero reference position. Table 3-3 summarises the axial distance of each measuring station relative to station (1).

Table 3-3: Axial position of measuring stations

Station#	1	2	3	4	5	6	7	8	9	10	11	12	13
Axial position [mm]	0	33	88	132	176	264	308	352	396	484	528	572	616

Four AC292-2C accelerometers are used to measure the response. These accelerometers have a dynamic range of ± 80 g with a sensitivity of 100 mV/g and a frequency-response range of 0.3-15000 Hz. The data sheet of the accelerometers can be found in Appendix C. The accelerometers are mounted onto the rotor by silver soldering nuts onto stainless steel hose clamps and clamping the accelerometers to the rotor [7].

dSPACE® is a real time development tool for fast prototyping. The *dSPACE*® controller is used for data capturing. The analogue signals generated by the accelerometers are fed to an interface board, where the signals are conditioned to the correct input for the *dSPACE*® controller. After conditioning the signals, the analogue signals are converted to digital signals by the *dSPACE*® controller and captured on a personal computer using the *ControlDesk*® graphical user interface [7]. The results obtained from the rotor modal analysis are discussed in the following section.

3.2.3 RDS rotor modal analysis results

A total of six tests are performed and for each test the floating accelerometers are placed at different measuring stations. Figure 3-4 illustrates the rotor suspended horizontally with slings hanging from the roof and the accelerometers mounted with stainless steel hose clamps.

Figure 3-4: Illustration of rotor modal analysis test setup

The first step in the data analysis process entails calculating the FFT of the data sampled by each accelerometer. This is done by using the built in FFT-function of *MATLAB*®. The modulus of each transformed signal is plotted against frequency. For illustration purposes the vibration spectrum of test number 6, calculated in *MATLAB*®, is given in Figure 3-5. Test number 6 has the configuration of the two floating accelerometers at stations (8) and (9).

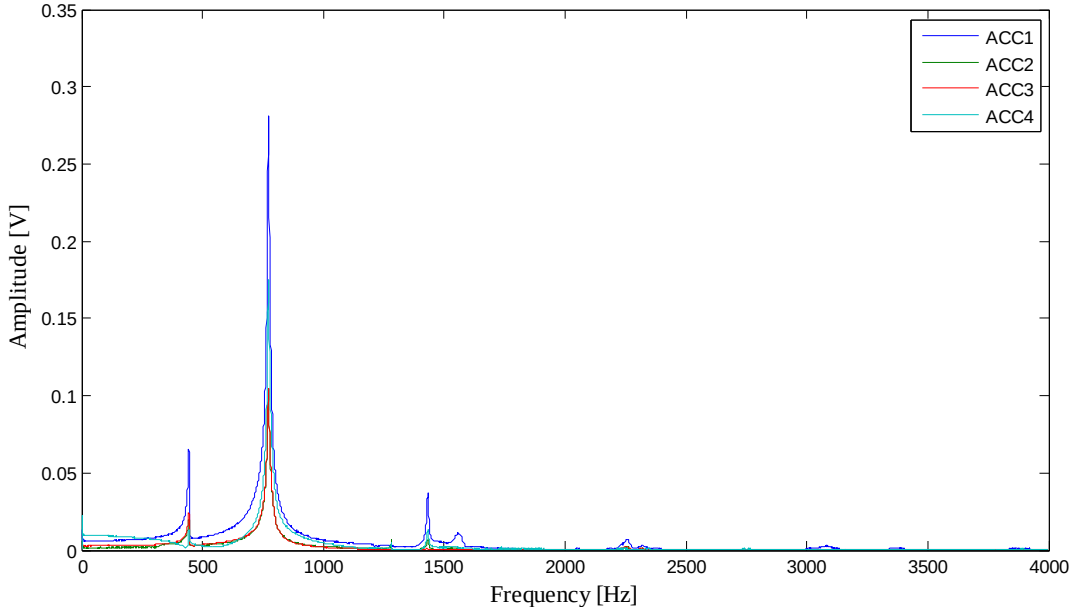

Figure 3-5: Vibration spectrum of 6th rotor modal analysis test

The peaks noted in Figure 3-5 correspond to the bending natural frequencies of the RDS rotor. It is clear that the first peak is situated at a frequency of approximately 444 Hz. From previous research it was established that this is a blower disc natural frequency [7]. This frequency is still investigated in order to validate the previous findings. As an indication of repeatability the first four bending natural frequencies of each test are summarised in Table 3-4. Figure 3-6 compares the bending natural frequencies summarised in Table 3-4.

Table 3-4: First four bending natural frequencies of the RDS rotor for each modal analysis test

Test #	1	2	3	4	5	6
First bending natural frequency [Hz]	443	443	443.5	443.5	443.5	443.5
Second bending natural frequency [Hz]	771.5	774.0	775.0	775.0	775.5	773.5
Third bending natural frequency [Hz]	1429.5	1431.0	1432.0	1433.5	1432.5	1433.5
Fourth bending natural frequency [Hz]	2313.0	2261.0	2263.0	2261.0	2264.0	2259.0

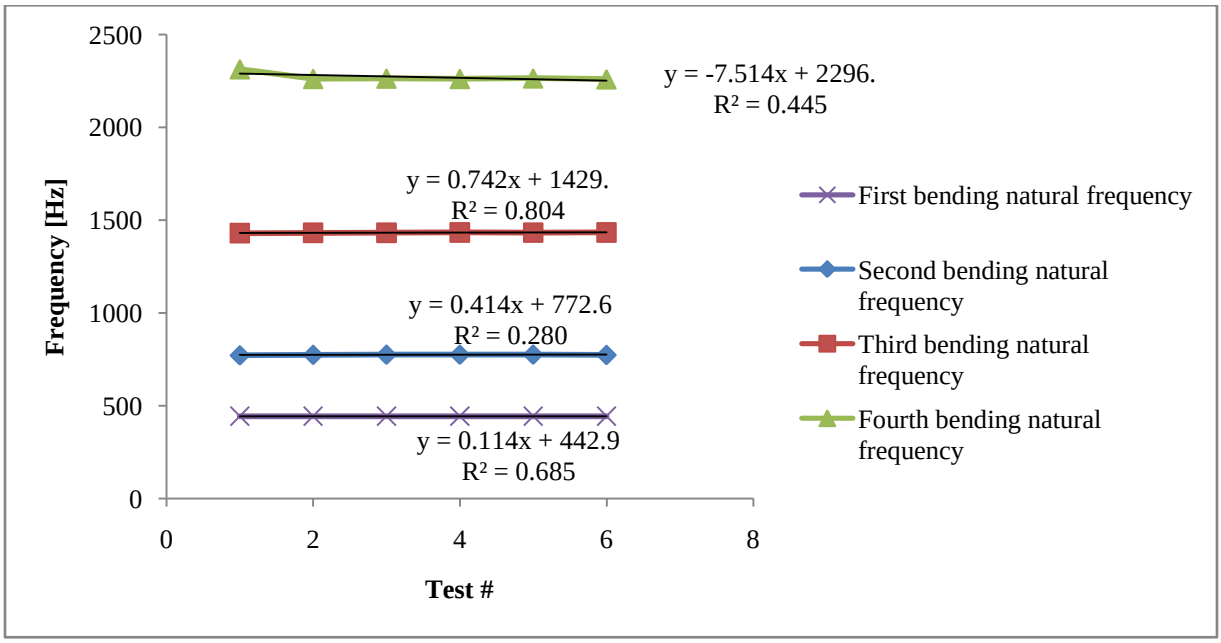

Figure 3-6: Comparison of bending natural frequencies from different tests on the RDS rotor

The results show respectable repeatability. The standard deviations of the first four bending natural frequencies of the RDS rotor are summarised in Table 3-5.

Table 3-5: Standard deviation of first four bending natural frequencies of the RDS rotor

Natural frequency	Average [Hz]	Standard deviation [Hz]
First bending	443.333	0.258
Second bending	774.091	1.463
Third bending	1432.014	1.549
Fourth bending	2270.190	21.056

For the first bending natural frequency noted in Figure 3-5, the modulus of each accelerometer for all the tests are summarised in Table 3-6.

Table 3-6: Modulus reading of the accelerometers for each test at the first bending natural frequency

Test #	ACC 1	ACC 2	ACC 3	ACC 4
1 (1_2_12_13)	0.060809	0.048803	0.00867	0.013986
2 (1_3_11_13)	0.066989	0.036939	0.02777	0.014677
3 (1_4_10_13)	0.070537	0.028314	0.03093	0.016148
4 (1_5_8_13)	0.08208	0.014866	0.02947	0.016761
5 (1_6_9_13)	0.070449	0.00805	0.02743	0.015511
6 (1_7_8_13)	0.06567	0.0199	0.0242	0.012508

The normalisation process is based on the principle of scaling the modulus of the floating accelerometers by using the ratio between the stationary accelerometers. This process requires a reference data set which is allocated to test number one. By comparing the first modulus readings of each test to the first modulus reading of the reference test, a multiplication factor (MF_i) can be determined. For each test, the inscriptions are then multiplied by the factor to scale the data set. The multiplication factor can be defined as:

$$MF_i = \frac{N_c}{M_i}, i = 2,3,\cdots,6 \tag{1}$$

where MF_i is the multiplication factor for test i, N_c is the first modulus reading of the reference data set and M_i is the first modulus reading of the test i. For illustration purposes, consider the data set of test number two summarised in Table 3-6. The multiplication factor for test number two can be calculated as:

$$MF_2 = \frac{N_c}{M_2} = \frac{0.060809}{0.066989} = 0.907746$$

Multiplying the modulus readings of test two with the multiplication factor MF_2, results in the normalised data set are summarised in Table 3-7.

Table 3-7: Normalised data of test number 2 in Table 3-6

Test #	MF_2	ACC 1	ACC 2	ACC 3	ACC 4
2 (1_3_11_13)	0.907746	0.060809	0.033531	0.02521	0.013323

This process is applied to all the tests and the results are summarised in Table 3-8.

Table 3-8: Normalised data for the first bending natural frequency of the RDS rotor

Test #	MF_i	ACC 1	ACC 2	ACC 3	ACC 4
1 (1_2_12_13)	1	0.060809	0.048803	0.00867	0.013986
2 (1_3_11_13)	0.907747	0.060809	0.033531	0.02521	0.013323
3 (1_4_10_13)	0.862087	0.060809	0.024409	0.02666	0.013921
4 (1_5_8_13)	0.740851	0.060809	0.011014	0.02183	0.012417
5 (1_6_9_13)	0.863161	0.060809	0.00695	0.02368	0.013389
6 (1_7_8_13)	0.925978	0.060809	0.01843	0.0224	0.011582

Note that the first and last modulus readings are constant for each test since these two accelerometers were kept stationary for each test. The data can now be used to generate the mode form of the first bending natural frequency. The phase angle also needs to be considered when constructing the mode form since the modulus is the absolute value of the computed transformed signal.

The phase angle of accelerometer one reading for each test is used as the reference when calculating the phase relation of the remaining readings. The reason for this is that accelerometer one is kept stationary for all the tests and the phase angle will vary for each test. The phase angle of the remaining accelerometer readings will either be in phase with the reference phase angle or 180° out of phase.

A sign convention can be defined based on this reference condition. If the phase of the modulus is in phase with the reference phase angle, the value of the modulus will be kept positive. On the other hand, if the phase angle of the modulus is 180° out of phase with the reference phase angle, then the modulus will become negative [7]. After applying the sign convention to the normalised data of Table 3-8, the polarised data can be summarised as illustrated in Table 3-9.

Table 3-9: Normalised and polarised data for the first bending natural frequency of the RDS rotor

Test #	ACC 1	ACC 2	ACC 3	ACC 4
1 (1_2_12_13)	0.060809	0.048803	-0.00867	0.013986
2 (1_3_11_13)	0.060809	0.033531	-0.02521	0.013323
3 (1_4_10_13)	0.060809	0.024409	-0.02666	0.013921
4 (1_5_8_13)	0.060809	0.011014	-0.02183	0.012417
5 (1_6_9_13)	0.060809	-0.00695	-0.02368	0.013389
6 (1_7_8_13)	0.060809	-0.01843	-0.0224	0.011582

By plotting the polarised data of Table 3-3 according to the axial positions of the measuring positions given in Table 3-9, the mode form of the RDS rotor at the first bending natural frequency can be characterized as in Figure 3-7.

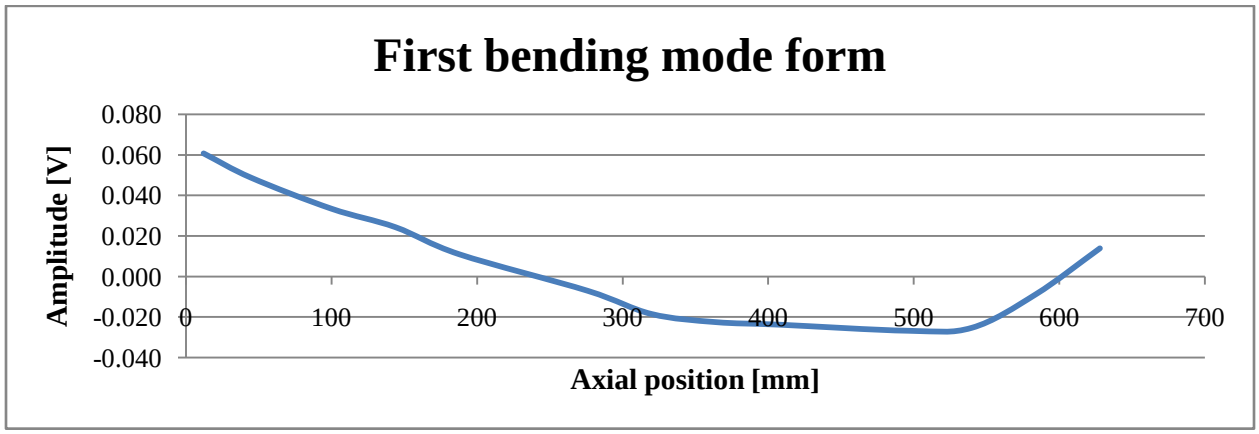

Figure 3-7: Mode form of the RDS rotor at the first bending natural frequency @ 443.333 Hz

Figure 3-7 clearly indicates that it is impossible to identify this frequency as a blower disc natural frequency. This frequency induces a lateral bending mode form and as such, it is impossible to identify it as a blower disc natural frequency. The same procedure used to construct the mode form of the first bending natural frequency is also used to identify the mode form of the second bending natural frequency illustrated in Figure 3-8.

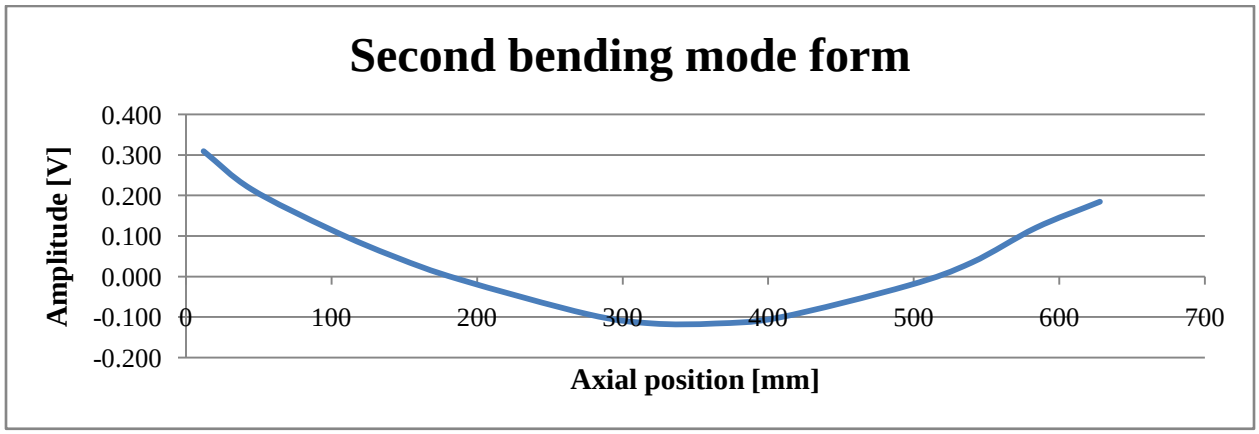

Figure 3-8: Mode form of the RDS rotor at the second bending natural frequency @ 774.091 Hz

By comparing Figure 3-7 and Figure 3-8 it should be clear that insufficient data is available in order to determine which one of these two frequencies is in fact the first bending mode. This contradicting with the findings of [7], identifying the first bending mode to be at approximately 778 Hz.

3.3 **RDS stator modal analysis**

The same method used to identify the rotor bending natural frequencies is also used to identify the stator bending natural frequencies. The experimental setup is different due to the locations available for sensing. Figure 3-9 identifies the four locations available for sensing; two of the locations in a horizontal manner and two in a vertical manner.

The stator is suspended by lifting it with two slings attached to the stator in a vertical manner. Since the stiffness of the slings will influence the response of the stator in a vertical manner, only the two horizontal locations are used for measuring the response of the stator.

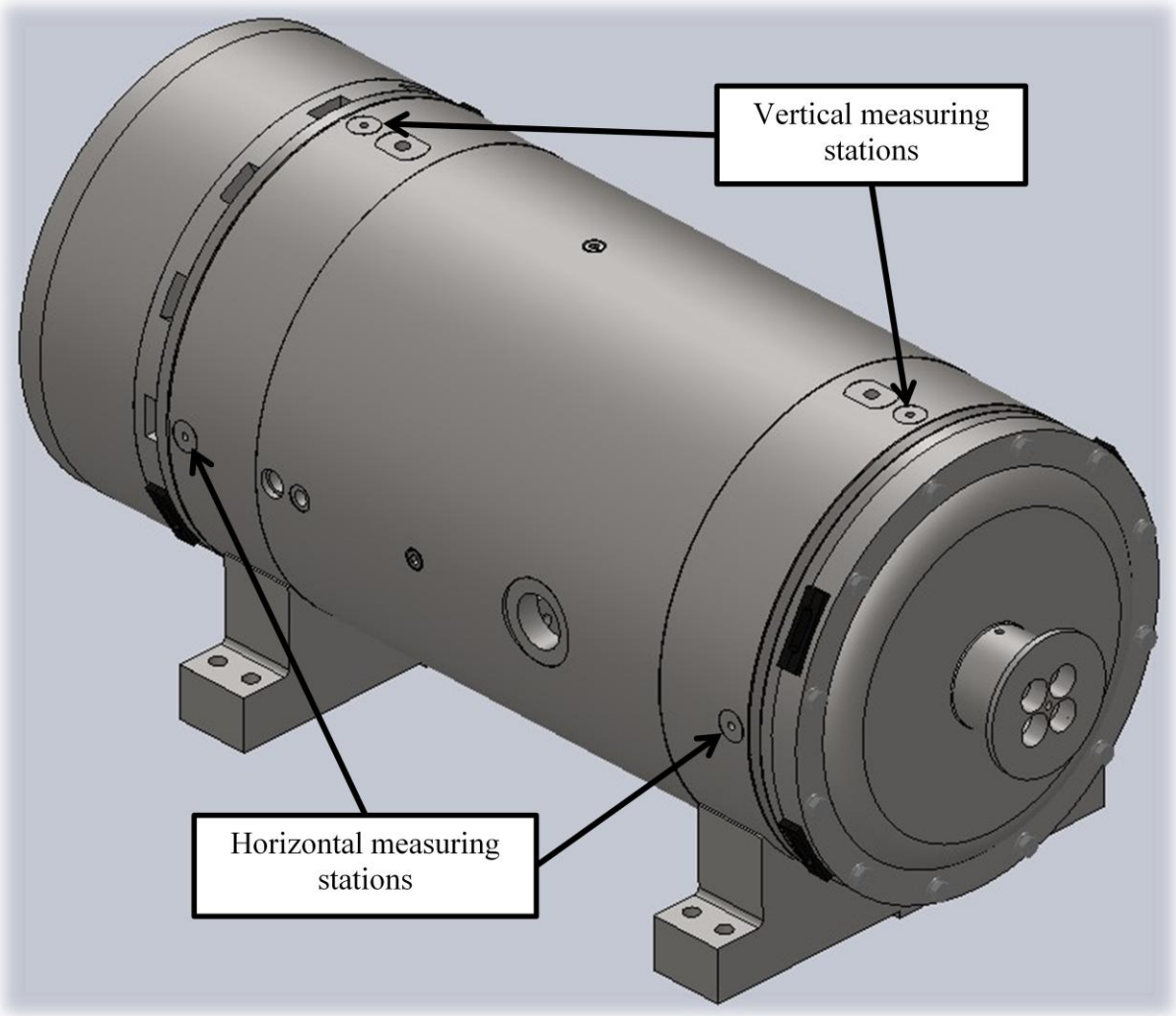

Figure 3-9: Stator measuring positions

3.3.1 RDS stator modal analysis results

A total of four tests are performed. For each test the accelerometers are kept at the same measuring stations and the stator is excited by using a plastic hammer. The reason for performing more than one test is to evaluate the repeatability of the bending natural frequencies.

The FFT of each signal is determined by using the built in FFT-function of *MATLAB*®. The modulus of each transformed signal is plotted against frequency. The vibration spectrum of test number 1, calculated in *MATLAB*®, is given in Figure 3-10.

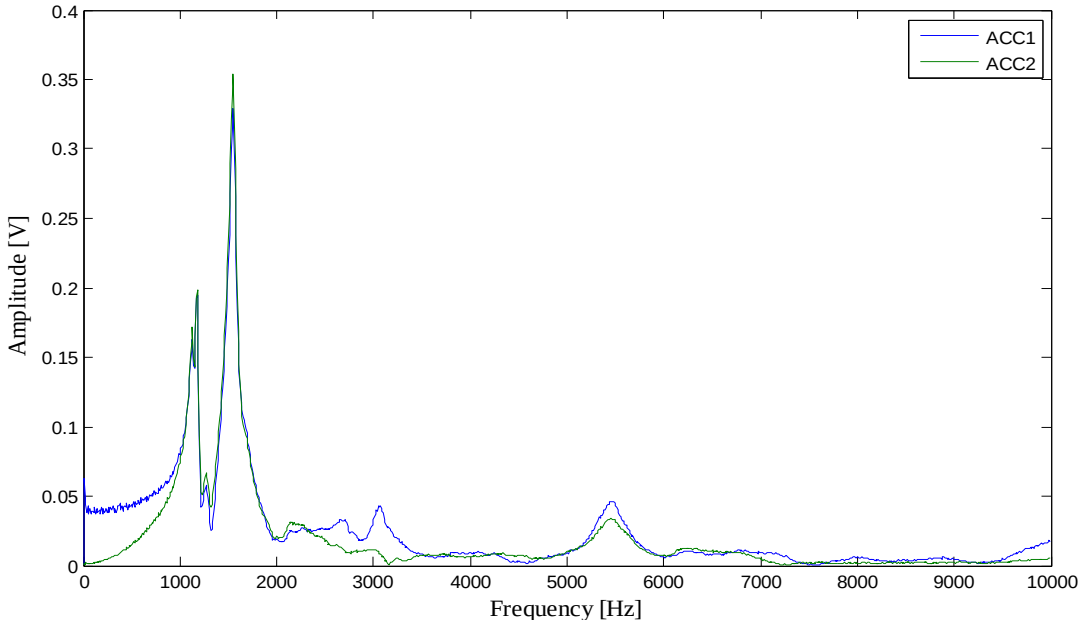

Figure 3-10: Vibration spectrum of 1st stator modal analysis test

Each of the peaks in Figure 3-10, corresponds to a bending natural frequency of the stator. As an indication of repeatability, the first two bending natural frequencies of each test are summarised in Table 3-10. Figure 3-11 compares the bending natural frequencies summarised in Table 3-10.

Table 3-10: First two bending natural frequencies of the RDS stator for each modal analysis test

Test #	1	2	3	4
First bending natural frequency [Hz]	1180	1190	1140	1170
Second bending natural frequency [Hz]	1550	1540	1550	1550

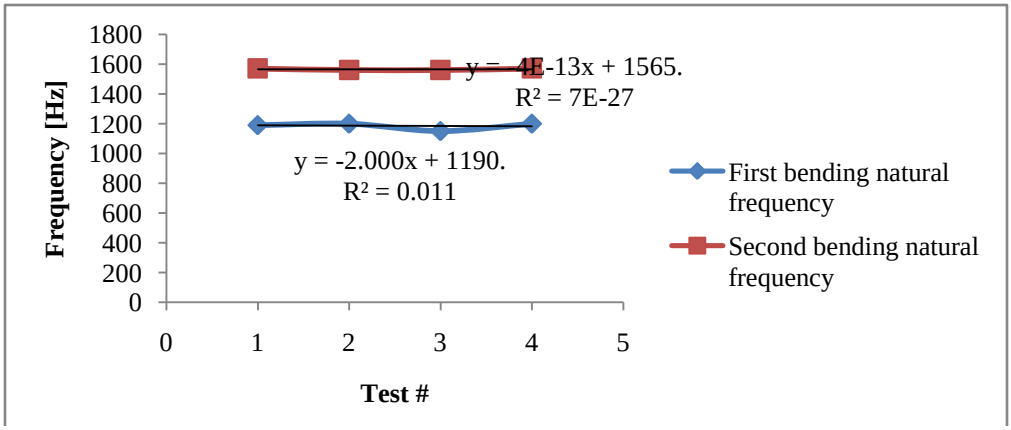

Figure 3-11: Comparison of bending natural frequencies from different tests on the RDS stator

The standard deviation of the first two bending natural frequencies of the RDS stator are summarised in Table 3-11. From Table 3-11, the first two bending natural frequencies agree satisfactorily.

Table 3-11: Standard deviation of first two bending natural frequencies of the RDS stator

Natural frequency	Average [Hz]	Standard deviation [Hz]
First bending	1170	21.6
Second bending	1547.5	5.0

The results summarised in Table 3-11 clearly identifies that the first bending natural frequency of the stator, at approximately 1170 Hz, is well outside the maximum operating speed of the rotor which is 317 Hz.

3.4 Concluding remarks

The geometric measurements and material densities of the RDS rotor were validated throughout this chapter. The elastic modulus of the materials could not be validated due to instrumentation and budget constraints. This chapter also investigated the natural response of the RDS rotor and stator. The bending natural frequencies of the RDS rotor and stator were validated using two modal analysis processes previously discussed. The mode forms of the RDS rotor bending natural frequencies could not be validated due to insufficient data.

This chapter validated the specifications needed to generate an accurate simulation model of the RDS. The geometric measurements and material densities were validated according to documented information. Two modal analysis processes were implemented to validate the bending natural frequencies of the RDS rotor and stator. The next chapter provides a simulation model of the RDS.

Chapter 4 Modelling

This chapter aims to discuss a finite element simulation model of the RDS. The chapter commences with a brief introduction followed by the processes used to verify and validate the finite element model as well as a discussion regarding the results. The chapter concludes with the verification of the RDS rotor natural response and remarks summarising the findings of the chapter.

4.1 Vibration modelling

Vibration modelling is one of the key concepts in vibration characterization. Models are used as approximation tools to evaluate vibrating systems. The origins of vibrations, and whether vibrations can be eliminated can be determined using the models.

Simulation models rely primarily on four aspects [1]:

- Mathematical modelling,
- formulation of governing equations,
- solution of the governing equations, and
- interpretation of the results.

Section 2.5 introduced three typical solution techniques used to assist vibration simulation. In order to verify the accuracy of a simulation model, the results are compared to other simulation models simulating the same system, however, utilising a different solution technique. The results of the verified simulation model are then compared to experimental results of the actual system to validate the accuracy of the simulation model.

4.2 RDS simulation model

The development of a reliable simulation model of the RDS entails three models: a finite element (FE) model, a numerical model and an analytical model. A FE model of the RDS is constructed in the computer software package known as *DyRoBeS*®. A simplified numerical model based on Rayleigh's energy method is constructed by using conventional beam theory and the principle of superposition. Finally, an analytical model is constructed by approximating the RDS as a two-degree-of-freedom system describing the behaviour of the rotor's centre of mass. The processes used to verify and validate the simulation model of the RDS are illustrated in Figure 4-1.

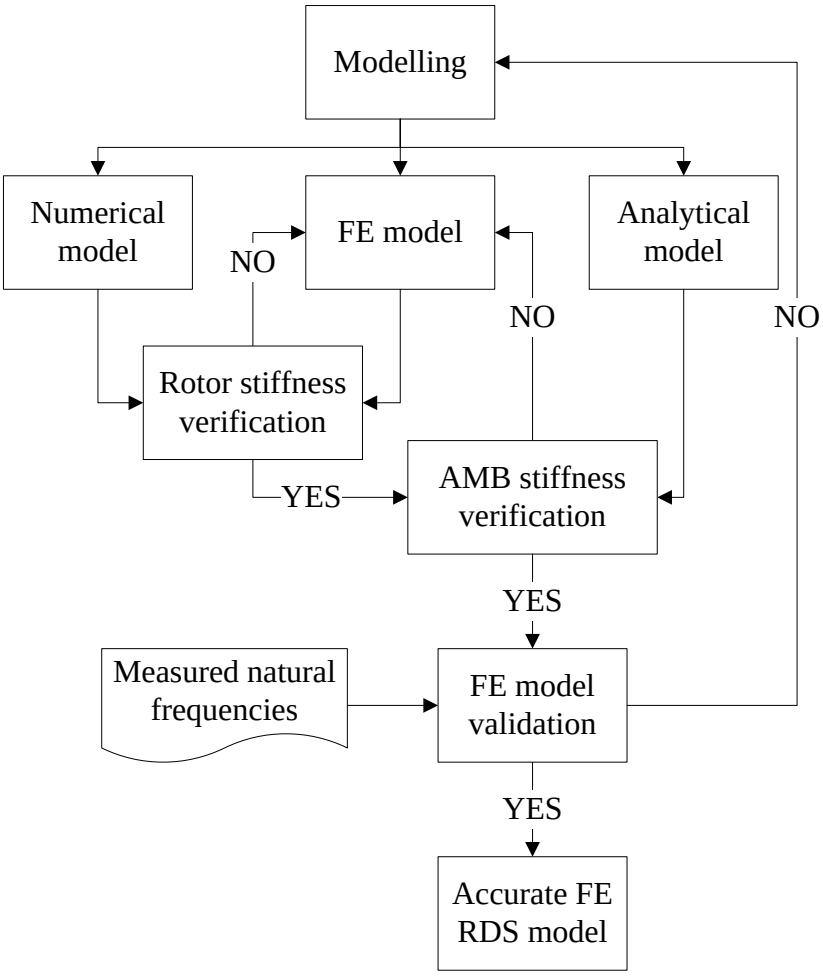

Figure 4-1: RDS model verification and validation flow diagram

4.2.1 RDS FE model verification process

Notice from Figure 4-1, that the numerical model is used to verify the FE model in terms of the rotor lateral stiffness. This is done by comparing the numerically calculated fundamental frequency, also known as the first bending natural frequency, to the simulated first bending natural frequency of the FE model. Correlation between the simulated and calculated first bending natural frequency verifies the RDS FE model in terms of rotor lateral stiffness.

The analytical model is used to verify the FE model in terms of AMB stiffness. This is done by comparing the simulated rigid body natural frequencies of the FE model to the calculated rigid body natural frequencies of the analytical model, as illustrated in Figure 4-1. Correlation between the simulated and calculated rigid body natural frequencies verifies the RDS FE model in terms of AMB stiffness.

4.2.2 RDS FE model validation process

According to Figure 4-1, the validation process of the RDS FE simulation model focuses on the correlation between the simulated and measured natural frequencies. The experimentally measured bending natural frequencies of the rotor, identified in section 3.2, are compared to the simulated bending natural frequencies of the verified FE model. Correlation between the measured and calculated bending natural frequencies validates the RDS FE model. The rigid body natural frequencies are however only simulated in this chapter, since the experimental characterization of these frequencies will commence in Chapter 5. The validation of the RDS FE model, in terms of the AMB stiffness, will also be discussed in Chapter 5.

It should be clear from Figure 4-1, the process used to construct a simulation model of the RDS is an iterative process. This process guarantee an accurate simulation model of the RDS.

4.3 RDS FE model

The FE simulation model of the RDS, constructed within the package *DyRoBeS*®, consists of a rotor held in place by two bearings connected to rigid supports as illustrated in Figure 4-2.

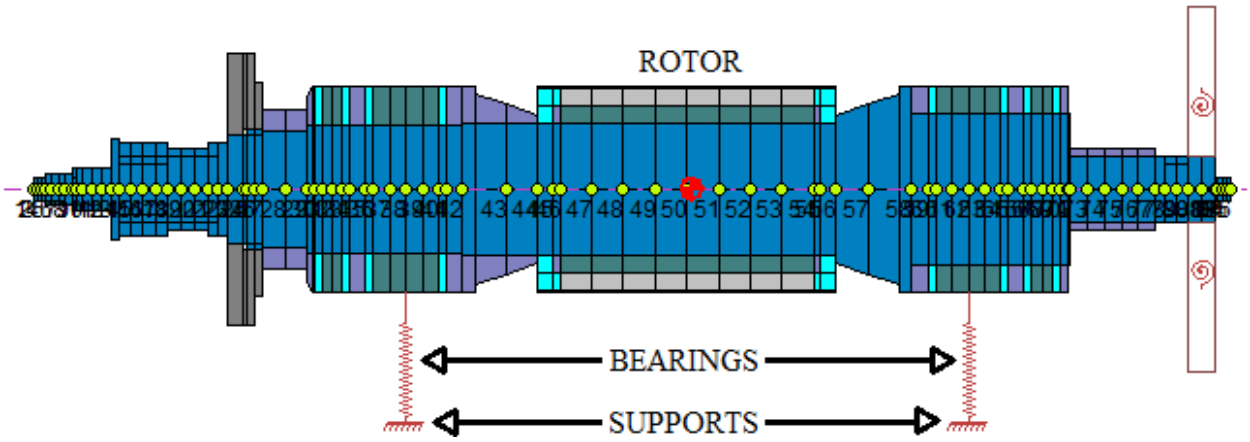

Figure 4-2: RDS rotor-bearing FE model

Figure 4-2 represents the actual complex RDS rotor with all the assembled components and discs. The AMBs are represented by two bearings, connecting the rotor to the foundation. The assumptions used to keep the model conservative can be summarised as:

- Lamination materials used for the AMBs, the IM and shrunk fitted components contribute only to the mass and not to the lateral stiffness of the rotor,
- internal friction between components is ignored,
- the axial AMB thrust runner is simulated as a rigid disc and the blower disc as a flexible disc,

- the AMBs are modelled as linear isotropic bearings, and
- the bearing supports are taken as rigid compared to the low stiffness of AMBs.

The model requires the elastic modulus of every material which contributes to the lateral stiffness of the rotor. The only material contributing to this stiffness according to the assumptions above is AISI 4140. Its properties are documented in various material science textbooks. AISI 4140 has an elastic modulus of 2E+11 Pa and a shear modulus of 7.5E+10 Pa [21].

An approach that can be used to calculate the attachment stiffness of a flexible disc from the theory of elasticity is presented in [10]. For the model it is assumed that the disc can bend. The stiffness of the disc is dependent on the ratio between the outside diameter of the disc and the shaft diameter [10]. From the design of the RDS, the ratio of the blower disc outside diameter to the shaft diameter is greater than the ratio of the AAMB thrust runner outside diameter to the shaft diameter. It is therefore expected that the flexibility of the blower disc will have a greater effect on the rotor dynamics. For this reason only the blower disc is simulated as a flexible disc and the AAMB thrust runner as a rigid disc.

The attachment stiffness of a disc is calculated by using the elastic modulus *E*, disc thickness *t*, shaft diameter $2r_0$, and disc diameter 2a, according to the imperial standard system. The geometric measurements and material properties of the blower disc are summarised in Table 4-1 according to the metric and imperial standard systems.

Table 4-1: Geometric and material properties of blower disc

Disc diameter (2a)	Shaft diameter ($2r_0$)	Thickness (*t*)	Elastic modulus (*E*)
0.2165 m / 8.524 in	0.04 m / 1.575 in	0.0157 m / 0.6181 in	2E+011 Pa / 2.9008E+007 psi

A quadratic equation is fitted to experimental results of several discs by [10]. The quadratic equation is used to identify a shape factor used in the calculation of the attachment stiffness of the disc. The shape factor alpha, as a function of the fraction between the inside radius r_0, and outside radius a, of the disc is illustrated in Figure 4-3 [10].

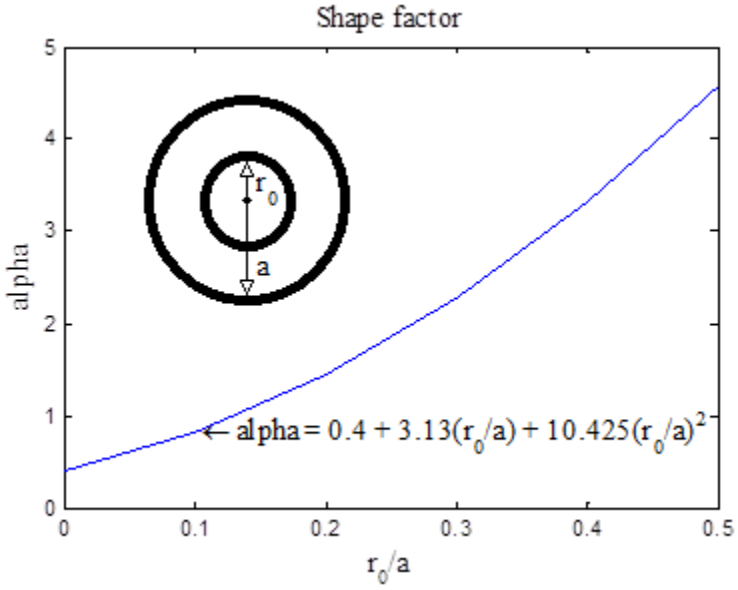

Figure 4-3: Shape factor, alpha, used to calculate attachment stiffness of disc [10]

The attachment stiffness of the blower disc can be calculated using the properties of Table 4-1 and Figure 4-3 [10]:

$$\begin{aligned} K_T &= \alpha E t^3 \\ &= \left[0.4 + 3.13 \cdot \left(1.575 / 8.524\right) + 10.425 \cdot \left(1.575 / 8.524\right)^2\right] \cdot \left(2.9008e+07\right) \cdot \left(0.6181\right)^3 \\ &= \left(1.3342\right) \cdot \left(2.9008e+07\right) \cdot \left(0.6181\right)^3 \\ &= 7.139013e+06 \left[\text{in} \cdot \text{ib} / \text{rad}\right] = 1.032570e+05 \left[\text{Nm} / \text{rad}\right] \end{aligned} \quad (4\text{-}1)$$

A summary of the FE model is included in Appendix D. The following section discusses the simulated rigid body natural frequencies of the RDS.

4.3.1 Simulated rigid body natural frequencies of the RDS FE model

The rigid body natural frequencies are simulated in the package *DyRoBeS*®, by conducting a critical speed analysis[13] of the model shown in Figure 4-2. The stiffness of the linear bearings, used to simulate the AMBs, is set to 1.9E+06 N/m as calculated in [7]. Figure 4-4 and Figure 4-5 illustrate the mode forms of the RDS rotor at the first and second rigid body natural frequencies of 40.82 Hz and 44.99 Hz respectively, as simulated using *DyRoBeS*®.

[13] A critical speed analsysis calculates the natural frequencies of a system [15].

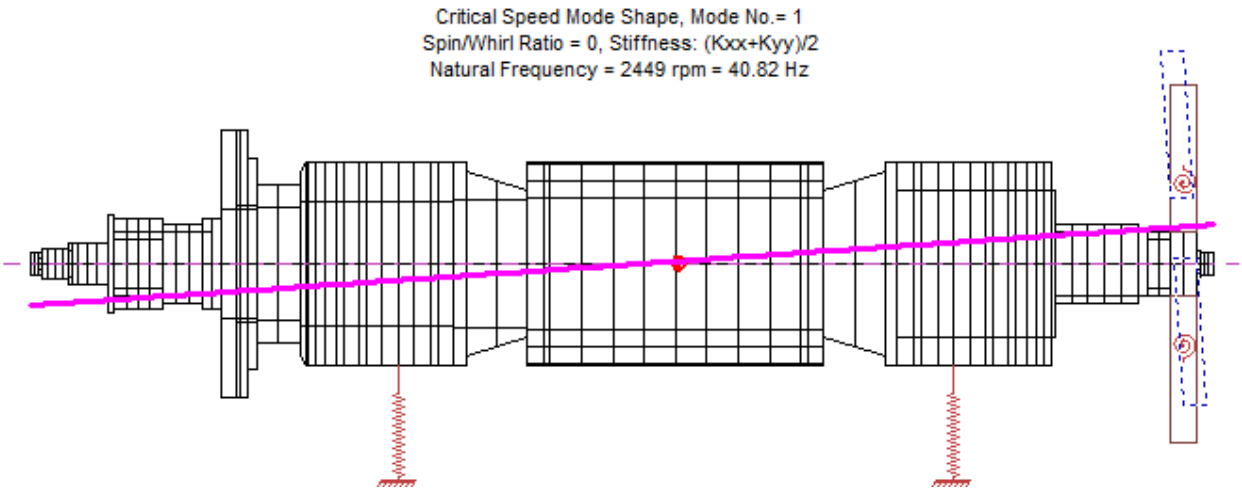

Figure 4-4: Mode form of first rigid body natural frequency of RDS FE model

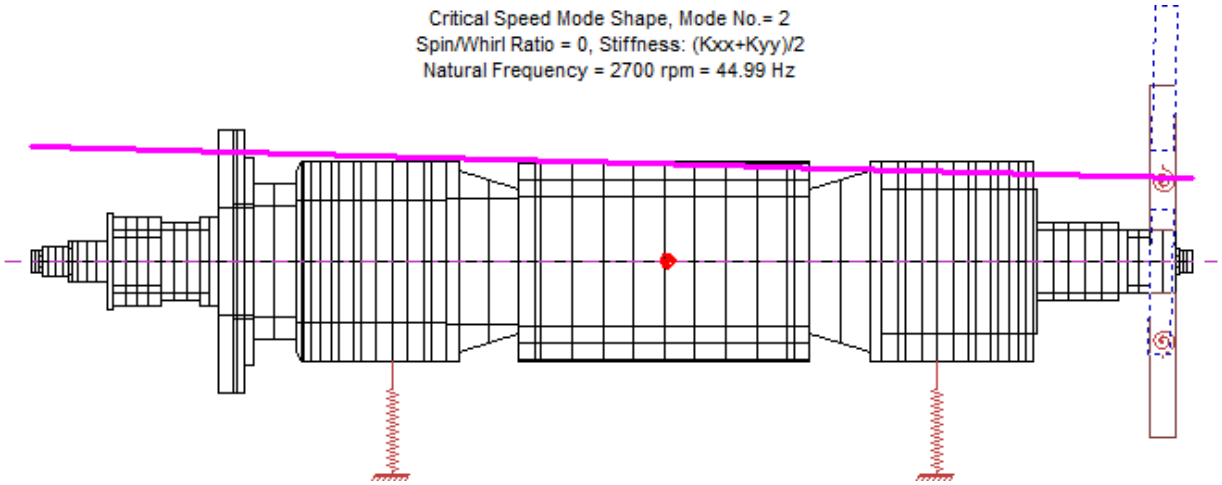

Figure 4-5: Mode form of second rigid body natural frequency of RDS FE model

In order to obtain results that can be compared to the numerical model, the first bending natural frequency of the RDS rotor is also simulated and presented in the following section.

4.3.2 Simulated first bending natural frequency of RDS FE model

Constraints and rigid discs are used in the RDS FE model rather than bearings and flexible discs, when simulating the first bending natural frequency. This will eliminate calculation errors and bearing effects by keeping the numerical model as simple as possible. Constraints are placed at station 29 and 72 of the RDS FE model. This equips the numerical model with uniform diameters over the domain of the rotor. From a critical speed analysis, conducted in the package *DyRoBeS*® the first bending natural frequency of the constrained RDS FE model is simulated at 434.67 Hz as illustrated in Figure 4-6.

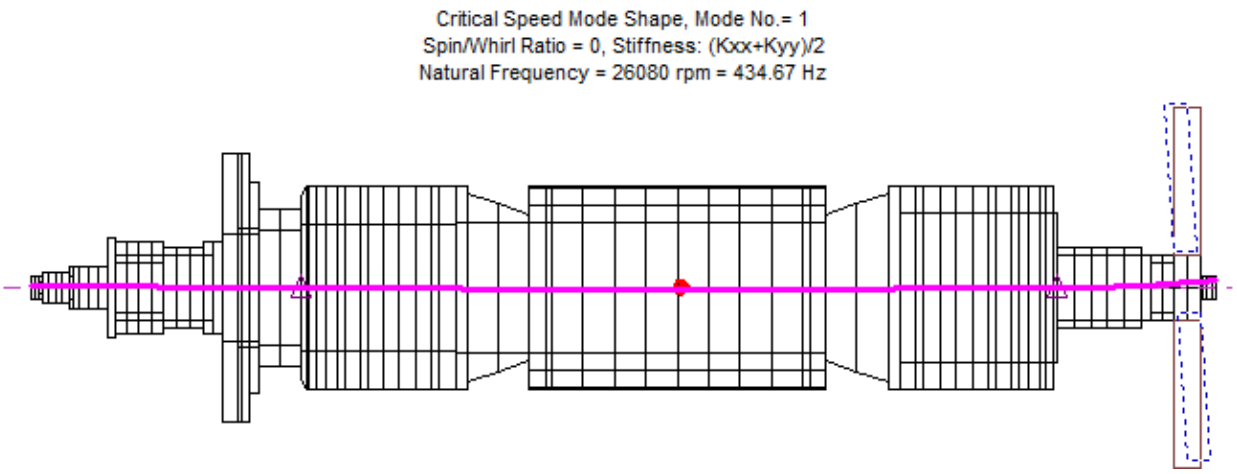

Figure 4-6: First bending natural frequency and mode form of constrained RDS FE rotor model

The numerical model used to verify the RDS FE model, in terms of lateral stiffness, is presented in the following section.

4.4 Numerical model

A simplified model of the RDS rotor illustrated in Figure 4-7(a) is used to construct a numerical model. Note the similarity between the numerical model illustrated in Figure 4-7(a), and the constrained RDS FE rotor model illustrated in Figure 4-6. Figure 4-7(b) illustrates the free-body diagram of the numerical model at the first bending natural frequency of the rotor.

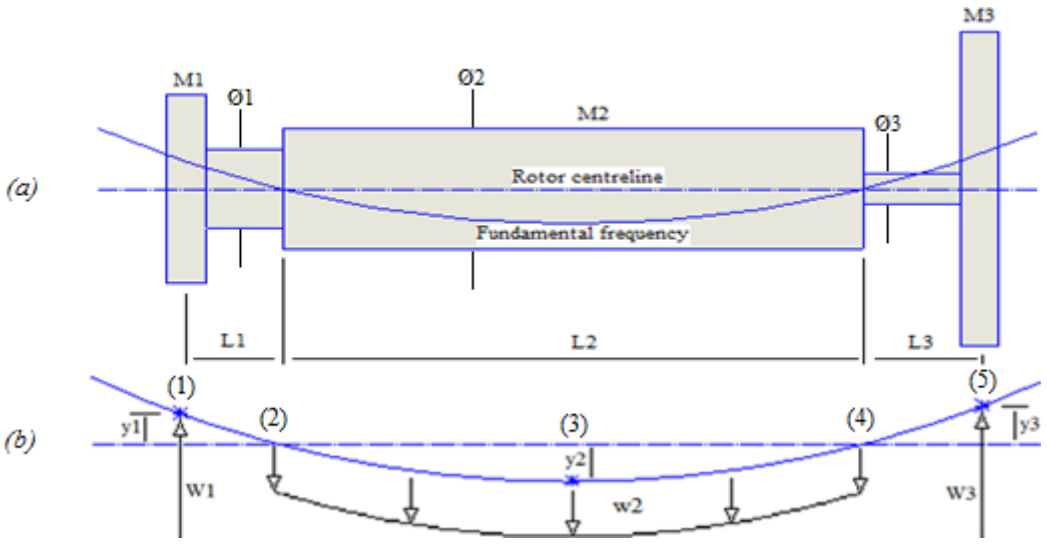

Figure 4-7: (a) Simplified numerical model, (b) Free-body diagram of numerical model

The weight of rotor to the left of the constrained station (2) and the weight of the thrust runner are lumped into the point force W1 of Figure 4-7(b). Using the same principle, the weight of the rotor to the right of

the constrained station (4) and the weight of the blower disc are lumped into the point force W3 of Figure 4-7(b). The weight of the rotor between constrained stations (2) and (4) is represented with the distributed force w2 shown in Figure 4-7(b). The properties of the numerical model illustrated in Figure 4-7(a), are summarised in Table 4-2.

Table 4-2: Properties of numerical model

Section (1) – (2)	**Section(2) – (4)**	**Section (4) – (5)**
L1 = 0.045 m	L2 = 0.445 m	L3 = 0.07 m
Ø1 = 0.056 m	Ø2 = 0.08 m	Ø3 = 0.04 m
W1	**w2**	**W3**
61.782 N	786.123 N/m	43.695 N

The following section calculates the deflection of the numerical model at stations (1), (3) and (5).

4.4.1 Deflection calculations for numerical model

The deflections of the numerical model are calculated by using conventional beam theory and the principle of superposition [22], [21]. The sign convention used to indicate the direction of deflection is taken as negative for downward deflection and positive for upward deflection.

Consider the free-body diagram, illustrated in Figure 4-7(b), with only the force W1 acting on the rotor. To compensate for the different diameters across the length of the rotor, two scenarios are used to determine the deflections of stations (1), (3) and (5) to the force W1. The first scenario approximates the section (1) to (2) as a cantilever beam with the force W1 acting on the beam, as illustrated in Figure 4-8(a). The second scenario approximates the rotor as a pin-supported beam with a bending moment, M1 resulting from the force W1 acting on the beam, as illustrated in Figure 4-8(b).

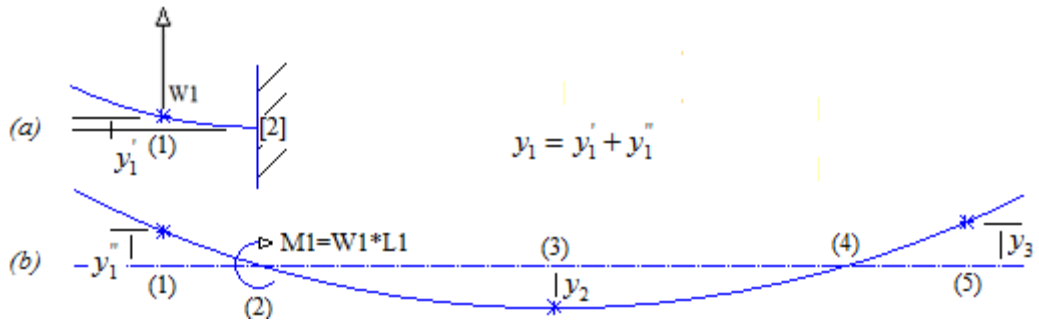

Figure 4-8: Deflection of rotor to force W1. (a) Cantilever beam approach for sections (1)-(2), (b) Pin-supported beam approach for sections (1)-(5)

For the cantilever beam approach in Figure 4-8(a), the partial deflection y_1', of station (1) can be calculated as [22]:

$$\begin{aligned} y_1' &= \frac{Wl^3}{3EI} \\ &= \frac{(W1)\cdot(L1^3)}{3\cdot(EI)_{(1)-(2)}} \\ &= \frac{(61.782)\cdot(0.045)^3}{3\cdot(2e+11)\cdot\left(\frac{\pi}{64}(0.056)^4\right)} \\ &= 1.944e-08 \text{ m} \end{aligned} \tag{4-2}$$

where $(EI)_{(1)-(2)}$ is the product of Young's modulus and moment of inertia of the section (1) to (2). The partial deflection y_1'', of station (1) can be calculated from the pin-supported beam approach as [21]:

$$\begin{aligned} y_1'' &= \theta_{(2)} L1 \\ &= \frac{Ml}{3EI} L1 \\ &= \frac{(M1)\cdot(L2)\cdot(L1)}{3\cdot(EI)_{(2)-(4)}} \\ &= \frac{(2.78019)\cdot(0.445)\cdot(0.045)}{3\cdot(2e+11)\cdot\left(\frac{\pi}{64}(0.08)^4\right)} \\ &= 4.615e-08 \text{ m} \end{aligned} \tag{4-3}$$

where $(EI)_{(2)-(4)}$ is the product of Young's modulus and moment of inertia of the section (2) to (4). The resultant deflection of station (1) to the force W1 can now be calculated as:

$$\begin{aligned} y_1 &= y_1^{'} + y_1^{"} \\ &= (1.944e-08) + (4.615e-08) \\ &= 6.559e-08 \text{ m} \end{aligned} \tag{4-4}$$

The deflection of station (3) to the bending moment M1 can be calculated as:

$$\begin{aligned} y_2 &= -\frac{Mlx}{6EI}\left(1-\frac{x^2}{l^2}\right) \\ &= -\frac{M1\cdot L2\cdot(0.5\cdot L2)}{6\cdot(EI)_{(2)-(4)}}\left(1-\frac{(0.5\cdot L2)^2}{(L2)^2}\right) \\ &= -\frac{(2.78019)\cdot(0.445)\cdot(0.2225)}{6\cdot(2e+11)\cdot\left(\frac{\pi}{64}(0.08)^4\right)}\left(1-\frac{(0.2225)^2}{(0.445)^2}\right) \\ &= -8.557e-08 \text{ m} \end{aligned} \tag{4-5}$$

where $(EI)_{(2)-(4)}$ is the product of Young's modulus and moment of inertia of the section (2) to (4). The deflection of station (5) to the bending moment M1 can be calculated as [22]:

$$\begin{aligned} y_3 &= \theta_{(4)} L3 \\ &= \frac{Ml}{6EI} L3 \\ &= \frac{(M1)\cdot(L2)\cdot(L3)}{6\cdot(EI)_{(2)-(4)}} \\ &= \frac{(2.78019)\cdot(0.445)\cdot(0.07)}{6\cdot(2e+11)\cdot\left(\frac{\pi}{64}(0.08)^4\right)} \\ &= 3.589e-08 \text{ m} \end{aligned} \tag{4-6}$$

where $(EI)_{(2)-(4)}$ is the product of Young's modulus and moment of inertia of the section (2) to (4). After evaluating the deflections to each individual force illustrated in Figure 4-7(b) the deflections can be summarised as in Table 4-3.

Table 4-3: Deflections of numerical model by beam theory

Deflection:	W1	w2	W3
y_1	6.559e-08 m	3.230e-07 m	2.539e-08 m
y_2	-8.557e-08 m	-9.982e-07 m	-9.414e-08 m
y_3	3.589e-08 m	5.025e-07 m	2.778e-07 m

The principle of superposition is used to determine the resultant deflection of each of the stations (1), (3) and (5). Adding the deflections of Table 4-3 gives the resultant deflections as:

$$\begin{aligned} y_1 &= (6.559e-08)+(3.230e-07)+(2.539e-08) \\ &= 4.140e-07 \text{ m} \\ y_2 &= (-8.557e-08)+(-9.982e-07)+(-9.414e-08) \\ &= -1.178e-05 \text{ m} \\ y_3 &= (3.589e-08)+(5.025e-07)+(2.778e-07) \\ &= 8.161e-07 \text{ m} \end{aligned} \tag{4-7}$$

The following section calculates the first bending natural frequency of the numerical model.

4.4.2 Calculated first bending natural frequency of numerical model

Rayleigh's energy method is used to approximate the first bending natural frequency of the system. The first bending natural frequency of the numerical model can be calculated as [16]:

$$\begin{aligned} \omega_n &= \sqrt{\frac{g\sum My}{\sum My^2}} \\ &= \sqrt{\frac{g\left(W1\cdot y_1 + W2\cdot y_2 + W3\cdot y_3\right)}{\left(W1\cdot y_1^2 + (w2\cdot L2)\cdot y_2^2 + W3\cdot y_3^2\right)}} \\ &= \sqrt{\frac{(9.81)\cdot(4.733e-04)}{(5.250e-10)}} \\ &= 2973.723 \text{ r/min} \\ &= 473.287 \text{ Hz} \end{aligned} \tag{4-8}$$

The correlation between this numerically calculated first bending natural frequency and the simulated first bending natural frequency is discussed in section 4.6. The analytical model used to verify the rotor, in terms of AMB stiffness, is presented in the following section.

4.5 Analytical model

The two-degree-of-freedom analytical model approximates the translation and rotation motion of the rotor's centre of mass as two degrees of freedom. This implies that rotor stiffness is ignored for this model. Referring to section 2.5, the system properties used for the analytical model can be summarised as in Table 4-4.

Table 4-4: RDS properties for analytical modelling

m_{eq}	J_{eq}	k_1	k_2	l_1	l_2
47.567 kg	1.595 kg·m^2	1.9E+06 N/m	1.9E+06 N/m	0.169 m	0.163 m

Substituting the values of Table 4-4 into (2-20), the matrix can be rewritten as:

$$\begin{bmatrix} \left(-47.567\omega^2 + 3.8e+06\right) & \left(-11400\right) \\ \left(-11400\right) & \left(-1.595\omega^2 + 104747\right) \end{bmatrix} \begin{Bmatrix} x \\ \theta \end{Bmatrix} = \begin{Bmatrix} 0 \\ 0 \end{Bmatrix} \tag{4-9}$$

The following section calculates the characteristic equation of the analytical model and identifies the rigid body natural frequencies of the analytical model.

4.5.1 Calculated rigid body natural frequencies of the analytical model

The characteristic equation can be defined from the non-trivial solution of the two-degrees-of-freedom as [1]:

$$\det\begin{bmatrix} \left(-47.567\omega^2 + 3.8e+06\right) & \left(-11400\right) \\ \left(-11400\right) & \left(-1.595\omega^2 + 104747\right) \end{bmatrix} = 0 \tag{4-10}$$

$$75.869\omega^4 - 11.044e+06\omega^2 + 3.97909e+11 = 0$$

with the solution of the characteristic equation being the rigid body natural frequencies of the system. The rigid body natural frequencies are calculated from (4-10) as:

$$\omega_1 = \sqrt{(65521.728)} = 255.972 \text{ rad/s} = 40.739 \text{ Hz}$$
$$\omega_2 = \sqrt{(80044.972)} = 282.922 \text{ rad/s} = 45.028 \text{ Hz} \quad (4\text{-}11)$$

where ω_1 is the first and ω_2 is the second rigid body natural frequency of the analytical model. The following section summarises and discusses the results obtained from the three models.

4.6 RDS FE model verification

Table 4-5 summarises the simulated and calculated natural frequencies as identified by the three models.

Table 4-5: Simulated and calculated natural frequencies of RDS

Natural frequency #	FE model	Numerical model	Analytical model
1	40.82 Hz	---	40.739 Hz
2	44.99 Hz	---	45.028 Hz
3	434.67 Hz	473.283 Hz	---

According to Table 4-5 the prevalent error between two of the models occurs at the first bending natural frequency. The numerical model calculated the first bending natural frequency 8.88 % higher than the simulated first bending natural frequency in *DyRoBeS*®. The error can be attributed to the numerical model which does not incorporate shear deformation into the model and lumping the mass to keep the model conservative. None the less, the RDS FE simulation model is verified to an accuracy of 91.12 % at minimum. The following section validates the RDS model.

4.7 RDS FE model validation

The results obtained in section 3.2 are compared to the simulation results to validate the RDS FE model. The simulation results are generated by performing a critical speed analysis of the free-free[14] rotor model in *DyRoBeS*®. Figure 4-9(a) - Figure 4-9(d) illustrate the first four bending natural frequencies and mode forms of the RDS rotor model, as simulated in *DyRoBeS*®. The measured and simulated bending natural frequencies of the RDS rotor as well as the simulation error, are summarised in Table 4-6.

[14] For the free-free analysis of the rotor model in *DyRoBeS*®, the bearings and supports are removed making the simulated natural frequencies totally dependent of the rotor lateral stiffness.

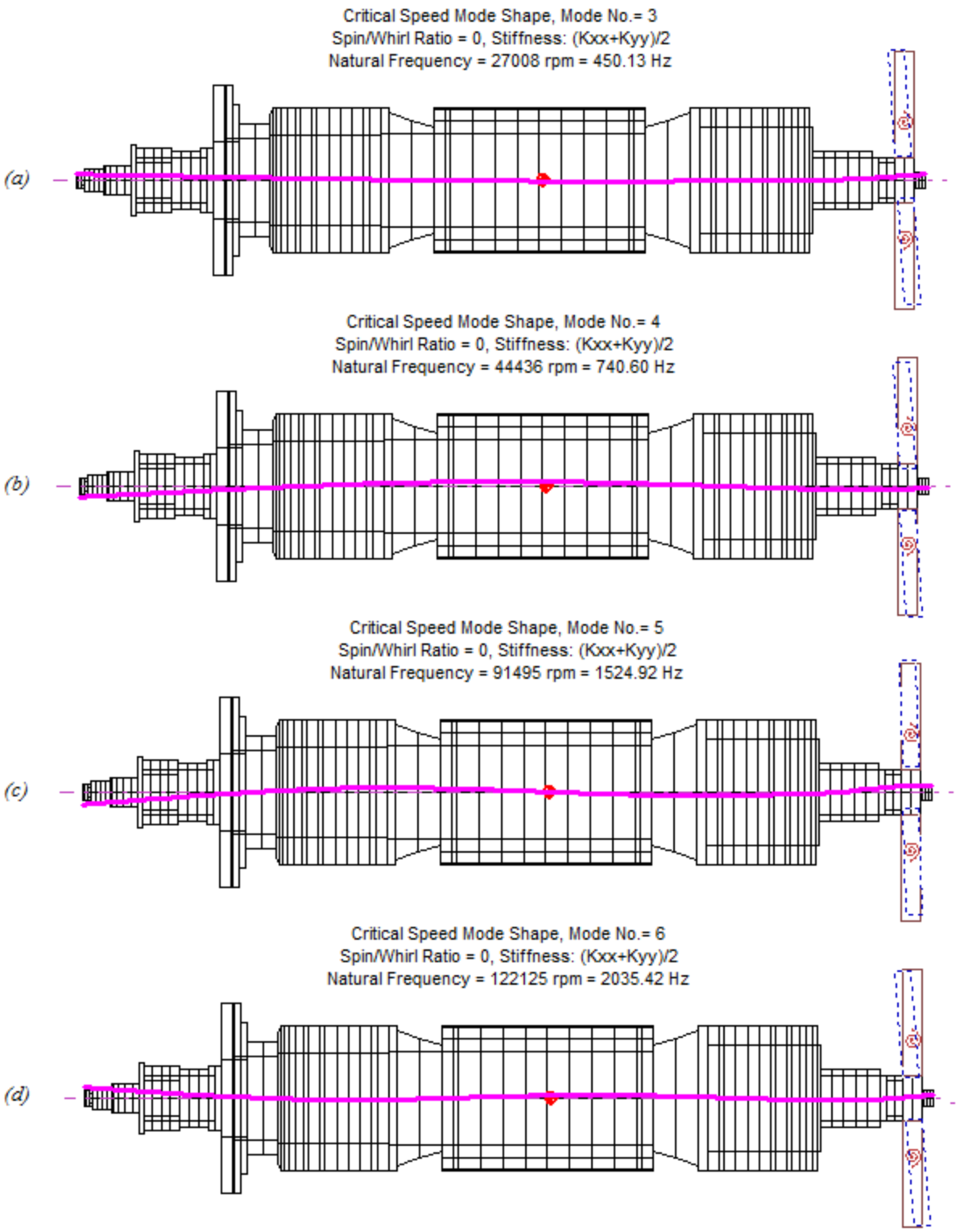

Figure 4-9: Simulated bending mode forms of the (a) first, (b) second, (c) third and (d) fourth bending natural frequency by *DyRoBeS*®

Table 4-6: Measured and simulated bending natural frequencies of the RDS rotor

Technique used	First bending natural frequency [Hz]	Second bending natural frequency [Hz]	Third bending natural frequency [Hz]	Fourth bending natural frequency [Hz]
Experimentally measured	443.333	774.091	1432.014	2270.190
Simulated	450.13	740.60	1524.96	2035.42
Error %	1.53	4.33	6.49	10.34

Table 4-6 clearly indicates that the highest simulation error is 10.34 % according to the experimentally measured bending natural frequencies. This validates the simulation model of the RDS rotor in the FE package *DyRoBeS*®. The following section verifies the experimentally measured first and second bending mode forms of the RDS rotor.

4.8 Verification of first two RDS rotor bending mode forms

As mentioned in section 3.2, insufficient data was available to identify the first and second bending mode forms of the RDS rotor. This phenomenon can be illustrated by plotting the simulated and measured bending mode forms on a single graph. Figure 4-10 and Figure 4-11 compare the simulated (blue) and measured (red) mode forms of the RDS rotor at the first and second bending natural frequencies, respectively.

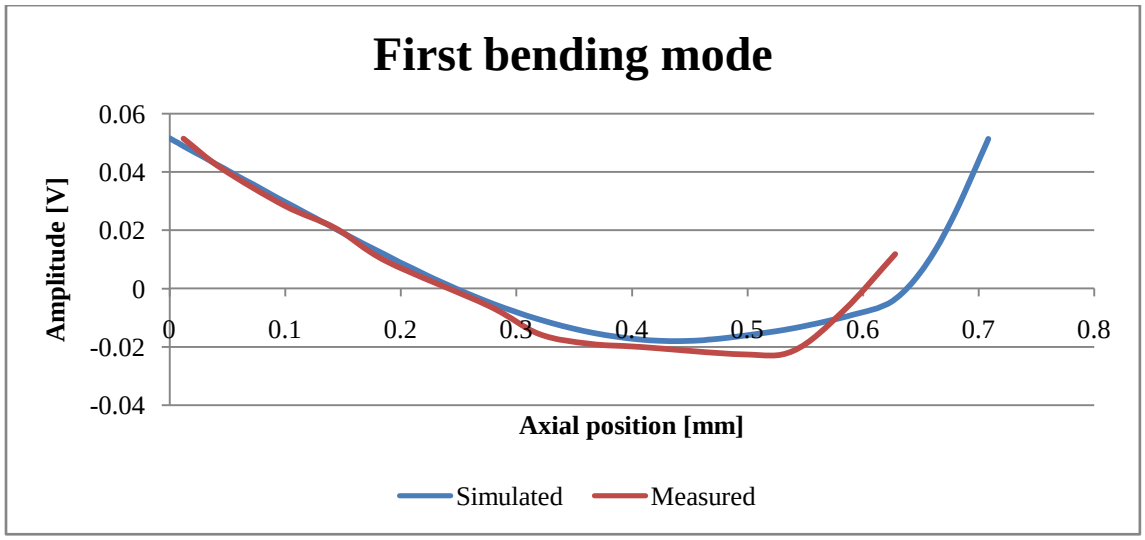

Figure 4-10: Simulated and measured mode form of RDS rotor at the first bending natural frequency (443.3 Hz)

Notice, the correlation between the slopes of the simulated and measured mode forms for both Figure 4-10 and Figure 4-11. This verifies that the simulated mode forms correlate with the measured mode forms. Referring back to the definition of rotor bending mode forms, in section 2.3, it should be clear from Figure 4-10 and Figure 4-11 that the first bending natural frequency of the RDS rotor is situated at a frequency of approximately 443.33 Hz.

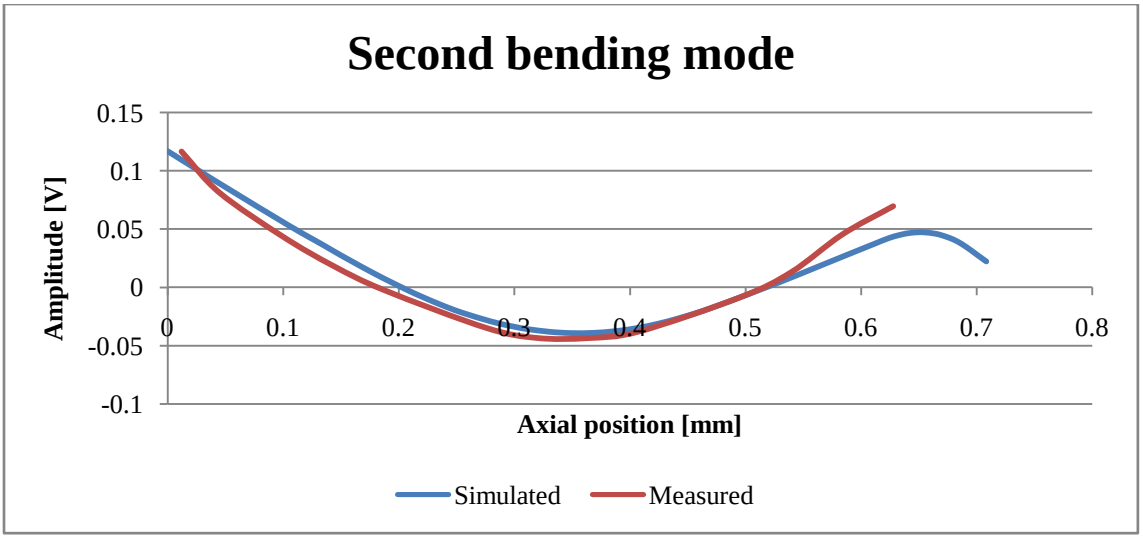

Figure 4-11: Simulated and measured mode form of RDS rotor at the second bending natural frequency (774.09 Hz)

The findings of [7], given in section 2.7 identified the first bending natural frequency of the RDS rotor at a frequency of 775 Hz. Figure 4-10 and Figure 4-11 thus this finding inaccurate.

4.9 Concluding remarks

A verified and validated FE simulation model of the RDS was presented throughout this chapter. The numerical and analytical model used to verify the FE model in terms of rotor and bearing stiffness were discussed. The correlation between the simulated and measured bending natural frequencies used to validate the FE model, in terms of rotor stiffness, were also discussed. The model could however not be validated in terms of bearing system, as the rigid body natural frequencies of the RDS have not yet been experimentally identified. The FE model also identified the inadequacy of the rotor modal analysis process presented in section 3.2, to identify the change in phase angle over the blower disc when characterizing the mode forms of the bending natural frequencies.

This chapter discussed a verified and validated finite element simulation model of the RDS. The models and processes used to verify and validate the model were also discussed. The next chapter provides the vibration characterization of the integrated RDS.

Chapter 5 System characterization

This chapter aims to provide the vibration characterization of the integrated RDS. The procedures and results of various experiments used to identify the rigid natural frequencies and force frequencies of the RDS are presented in this chapter. The correlation between the simulation model and the actual system response in terms of the rigid natural frequencies is also discussed. The chapter concludes with a rotor dynamic diagnostic investigation used to characterize the synchronous vibration harmonics of the RDS and remarks summarising the findings of the chapter.

5.1 RDS natural frequencies

In Chapter 3 the bending modes, as well as the geometric and material specifications of the rotor were characterized. Chapter 4 presented a simulation model of the RDS in the package *DyRoBeS*®. The simulation model validated the bending natural frequencies of the RDS rotor. As mentioned in section 2.3, the rigid body natural frequencies can only be characterized once the bearings are included in the experiments. This section investigates the natural frequencies of the integrated RDS.

5.1.1 Experimental procedure

Only two lateral measuring locations are available for measuring the response of the RDS rotor in the integrated system. The locations are embedded in the retainer bearing housings of the RDS. Two eddy-current probes (position transducer sensors) are available for measuring the response. The same experimental principles used in section 3.2 are used to characterize the natural frequencies of the integrated system. The test procedure described in section 3.2, is adapted to accommodate the measuring instrumentation. The test procedure used to identify the integrated RDS natural frequencies can be defined as:

1. Suspend the rotor of the RDS with the AMBs by using the drive electronic system (ADES),
2. excite the rotor by hitting the blower disc of the rotor laterally with an object (preferably a plastic hammer to prevent double tapping),
3. measure and capture the response of the RDS rotor with the eddy-current probes,
4. calculate the FFT of each measured signal separately,
5. calculate the modulus of the complex FFT values,
6. construct the vibration spectrum of the RDS by plotting the modulus of the FFT values against frequency,
7. calculate the phase angles at every natural frequency, and

8. calculate the mode form of the rotor at each natural frequency.

For the integrated system response, the stator is connected rigidly to the foundation. This implies that forced vibration induced by the stator is neglected.

5.1.2 Experimental setup

Figure 5-1 illustrates the test setup that is used to identify the natural frequencies of the RDS.

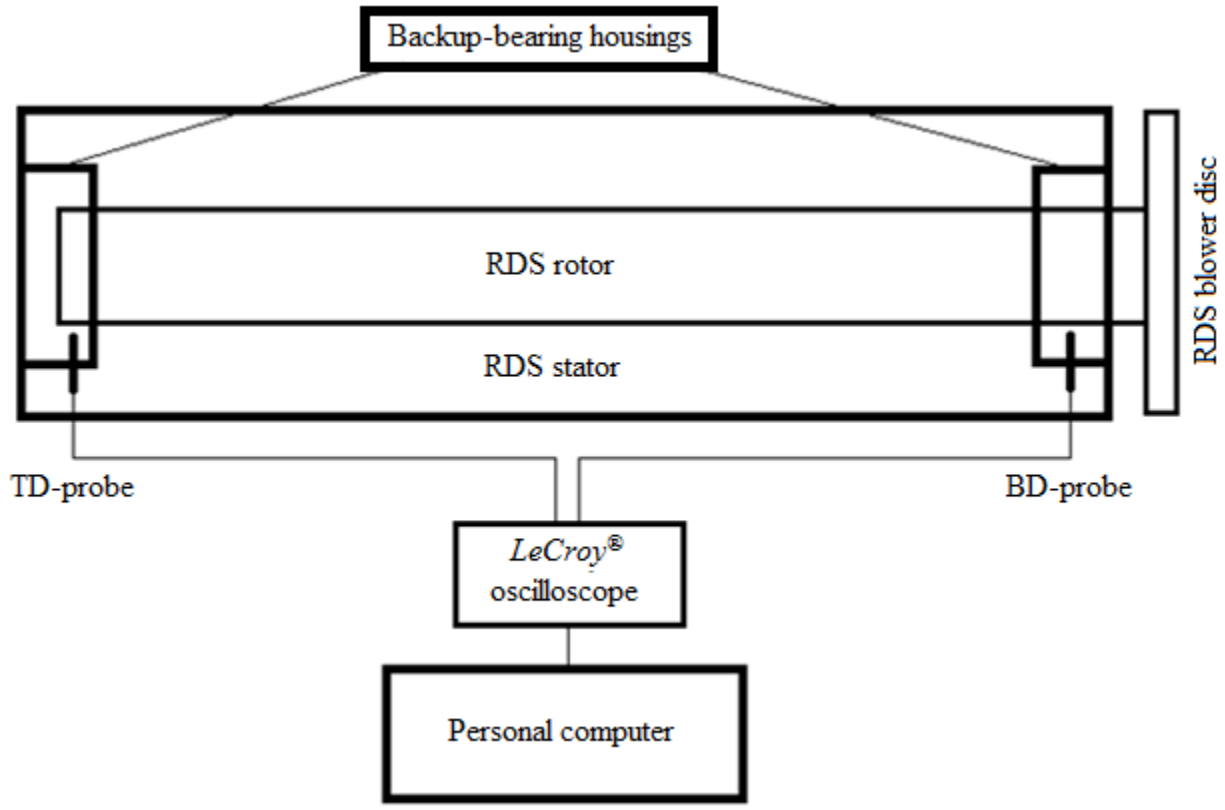

Figure 5-1: Schematic illustration of RDS investigation experimental setup

The experimental setup illustrated in Figure 5-1, consists of the integrated RDS, two CMSS 68-002-00-12-5A eddy-current probes mounted in the backup-bearing housings, a *LeCroy*® oscilloscope used for data sampling and capturing, and a personal computer for data analysis.

The CMSS 68-002-00-12-5A eddy-current probe exhibits a low pass characteristic with the 3 dB cut off at 10 kHz. The probes are calibrated to a linear spectrum of ± 25.4 μm of best straight line over 2.3 mm range with a sensitivity of 7.87 mV/ micron. The data sheet of the eddy-current probes can be found in Appendix C.

The oscilloscope used is from the *WaveRunner*-series from *LeCroy*®. This is a digital oscilloscope with sampling capability of 2.5 gigasamples per second and a bandwidth of 250 MHz.

The ADES used to suspend the rotor is an in-house developed digital control system designed for high-speed machinery. It constitutes an embedded controller that generates a reference to induce current in the electromagnetic actuators, according to the positions measured by the sensors. This control system is based on the typical layout of an AMB system discussed in section 1.1 [18].

5.1.3 RDS modal investigation results

For evaluation purposes, any frequency component noted higher than 10 kHz is ignored, since the attenuation of the eddy-current probes are higher than 3 dB. Also, the control parameters used for the operation of the system are chosen the same as in the design documentation of the AMBs discussed in [23]. The first step in the data analysis process entails calculating the FFT of the data sampled by each eddy-current probe. This is done by using the built in FFT-function of *MATLAB*®.

The vibration spectrum of the first test calculated in *MATLAB*®, is illustrated in Figure 5-2. The graph titles TD-probe and BD-probe refer to the position of the eddy-current probes during testing. The eddy-current probe on the left side in Figure 5-1, nearest to the thrust disc, is referred to as the TD-probe. The eddy-current probe on the right side in Figure 5-1, nearest to the blower disc, is referred to as the BD-probe. The peaks noted in Figure 5-2 correspond to the natural frequencies of the integrated RDS.

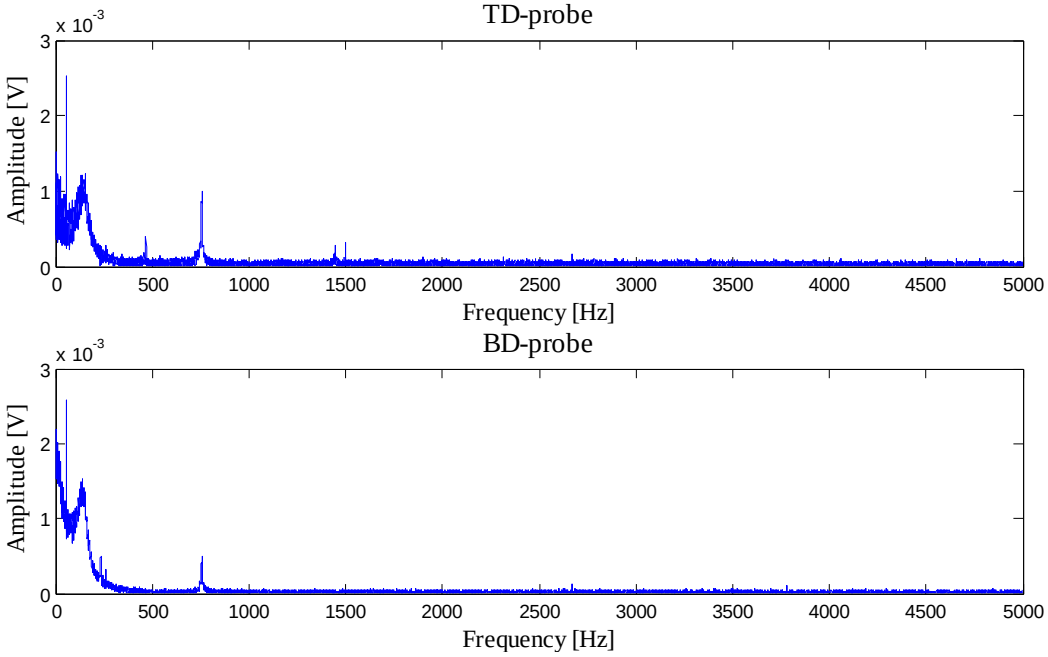

Figure 5-2: Vibration spectrum of the first test of the RDS to an impulse excitation

Figure 5-2 clearly indicates that no natural frequencies are measured above 1600 Hz. In order to ease the process of identifying the natural frequencies, the spectrum of Figure 5-2 is limited to 1600 Hz and illustrated in Figure 5-3.

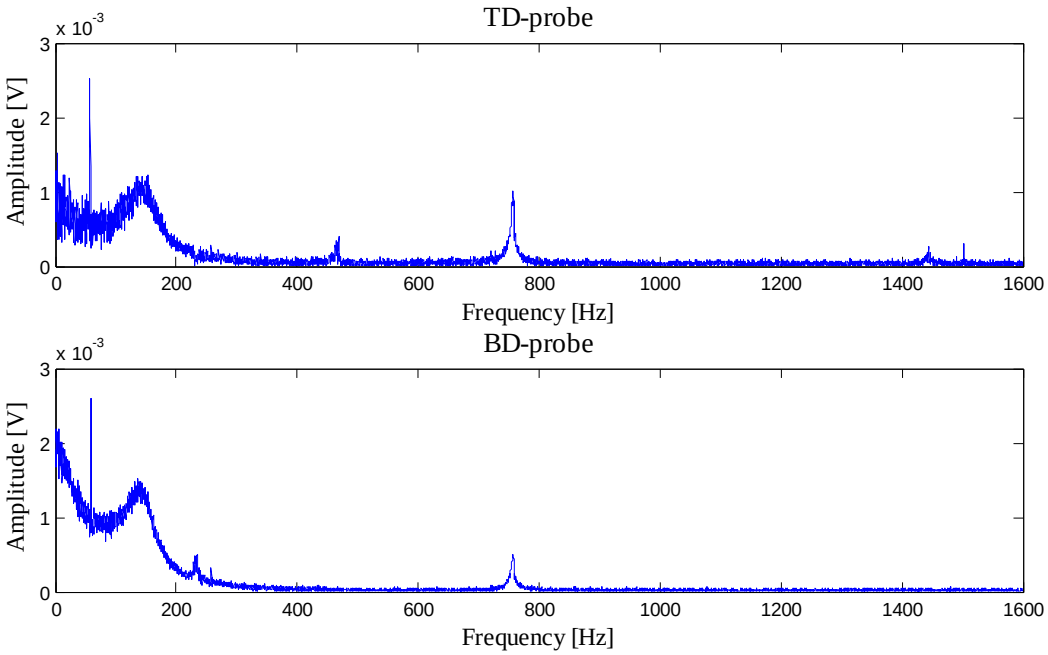

Figure 5-3: Limited vibration spectrum of Figure 5-2

The first and second bending natural frequencies of the RDS rotor, measured in section 3.2 and simulated in section 4.7, are clearly noticeable in Figure 5-3 at 464.8 Hz and 756.8 Hz. There is, however, a difference between these bending natural frequencies and the frequencies measured in section 3.2. The simulated rigid natural frequencies, discussed in section 4.3, do not correlate with the low frequency peaks in Figure 5-3. Two low-frequency peaks are visible in Figure 5-3, at approximately 59 Hz and 140 Hz. Whether these peaks represent the first or second rigid natural frequencies or forced frequencies are unclear due to the contradiction with the simulated natural frequencies of Chapter 4.

As mentioned previously, the rigid body natural frequencies of a system are directly influenced by the stiffness of the bearings. If the stiffness of the bearings were to change, the rigid body natural frequencies will also change. The low-frequency peaks of the vibration spectrum will shift accordingly on the frequency axis. The stiffness of the bearings can be altered because the RDS utilises AMBs. This enables the evaluation of the shift in the rigid body natural frequencies caused by stiffness variations.

The design of the AMBs documented in [23], states that the stiffness of the AMBs is governed by PD (proportional gain and differential gain) control parameters. For the radial AMB design, the relationship between the AMB stiffness and PD control parameters is defined as [23], [24]:

$$k_{eq} = 2K_P k_i - 2k_s \tag{5-1}$$

where k_{eq} is the equivalent bearing stiffness, K_P is the proportional gain control parameter, k_i is the slope of the linearized force-current relation of the AMB and k_s is the slope of the linearized force-displacement relation of the AMB[15]. The AMB stiffness can be altered by decreasing or increasing the proportional gain control parameter in (5-1). The proportional gain control parameter is limited to a minimum and maximum value to ensure the stability of the system.

Damping in a system decreases the vibration amplitudes at the natural frequencies of a system [11]. By minimising the damping in a system, the natural frequencies of the system become more prominent in the vibration spectrum. This eases the process of identifying the natural frequencies. In the case of the RDS, the equivalent damping of the AMBs is also governed by the PD control parameters [23]. The relationship between the PD control parameters and the equivalent damping of the AMB is defined as [23], [24]:

$$b_{eq} = 2K_D k_i \tag{5-2}$$

where b_{eq} is the equivalent damping of the AMB and K_D is the differential gain control parameter. The differential gain control parameter also has a minimum and maximum value to ensure the stability of the system. The damping of the AMBs is thus minimised by implementing the lowest allowable value of the differential control parameter. From experimental investigation, it was established that the minimum and maximum values of the PD control parameters for the RDS radial AMBs can be summarised as in Table 5-1.

Table 5-1: RDS PD control parameter limits

Limit	Proportional gain control parameter (K_P)	Differential gain control parameter (K_D)
Maximum	20000	40
Minimum	10000	10

To evaluate the effect of bearing stiffness on the low frequency-response of the RDS, the test procedure discussed in section 5.1.1 is repeated. For each repetition different control parameters are implemented to suspend the rotor of the RDS. Six PD control configurations, each with a decremented value of the proportional gain control parameter, are implemented. The differential gain control parameter is kept to the minimum value as illustrated in Table 5-2.

[15] Refer to [24], [23] and [5] for a detailed discription on the design of the AMBs.

Table 5-2: Control parameters for stiffness variation investigation

Test #	Proportional gain control parameter (K_P)	Differential gain control parameter (K_D)
1	20 000	10
2	18 000	10
3	16 000	10
4	14 000	10
5	12 000	10
6	10 000	10

The vibration spectrum of each PD control configuration was calculated in *MATLAB*® and can be seen in Figure 5-4. The blue curve represents the response measured by the TD-probe and the green curve the response measured by the BD-probe.

From Figure 5-4, it should be evident that for the RDS with the lowest amount of damping, a natural frequency is measured at approximately 62 Hz. The frequency shifts across the frequency axis as the stiffness of the system decreases. This indicates that the frequency is a rigid body natural frequency of the system according to section 2.3. A dominant frequency is measured at approximately 59 Hz, even though this frequency does not shift as the stiffness varies. This implies that it is not a rigid body natural frequency of the RDS.

The rigid body natural frequency measured in Figure 5-4 can be validated by performing mass variation tests [1]. The mass variation tests comprise the addition of extra mass to the RDS rotor while measuring the frequency-response of the system. This is made possible by bolting additional mass onto the rotor at the blower disc. To evaluate the effect of mass variation on the frequency-response of the RDS, the test procedure discussed in section 5.1.1 is repeated, while incrementing the mass of the RDS rotor. Additional mass up to 5 kg is available to be added in increments of 1 kg resulting in a number of six mass tests.

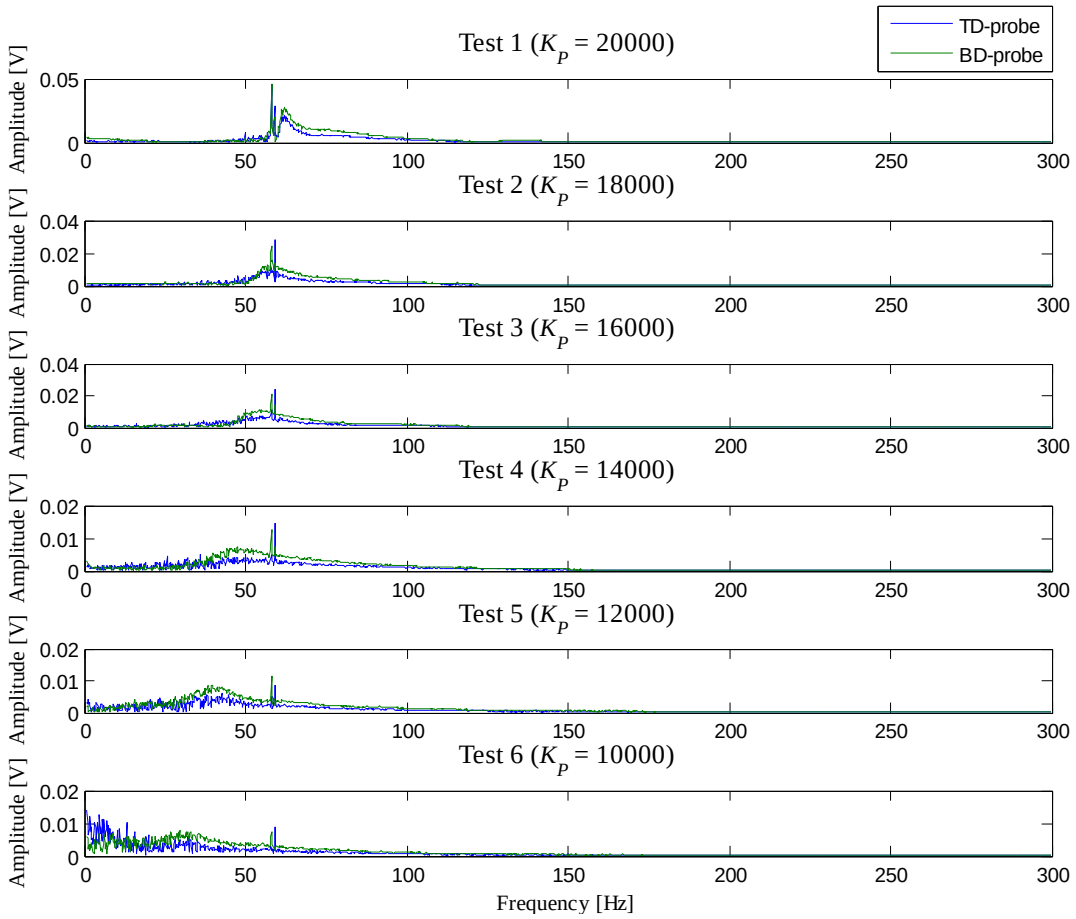

Figure 5-4: Vibration spectra of stiffness variation investigation with the blue response the measurement of the TD-probe and the green response the measurement of the BD-probe

The vibration spectrum of each incremented mass test calculated in *MATLAB*®, is illustrated in Figure 5-5. The blue curve represents the response measured by the TD-probe and the green curve the response measured by the BD-probe.

It should be clear from Figure 5-5 that a natural frequency of the RDS is excited originally at approximately 62 Hz, and shifts across the frequency axis as the mass of the RDS rotor increases. This correlates with the stiffness variation tests illustrated in Figure 5-4. The results presented in Figure 5-5 verifies the excited rigid body natural frequency measured in Figure 5-4. A dominant peak is measured at approximately 59 Hz in Figure 5-5, which does not shift as the mass of the RDS rotor increases. This verifies that the 59 Hz measured frequency in Figure 5-4, is not a rigid body natural frequency of the RDS but rather a forced frequency that may be induced by the electronics used in the RDS. The low-amplitude peaks noted in the vicinity of 100 Hz for test 5 and test 6 result from the elasticity of the bolt used to equip the RDS rotor with additional mass.

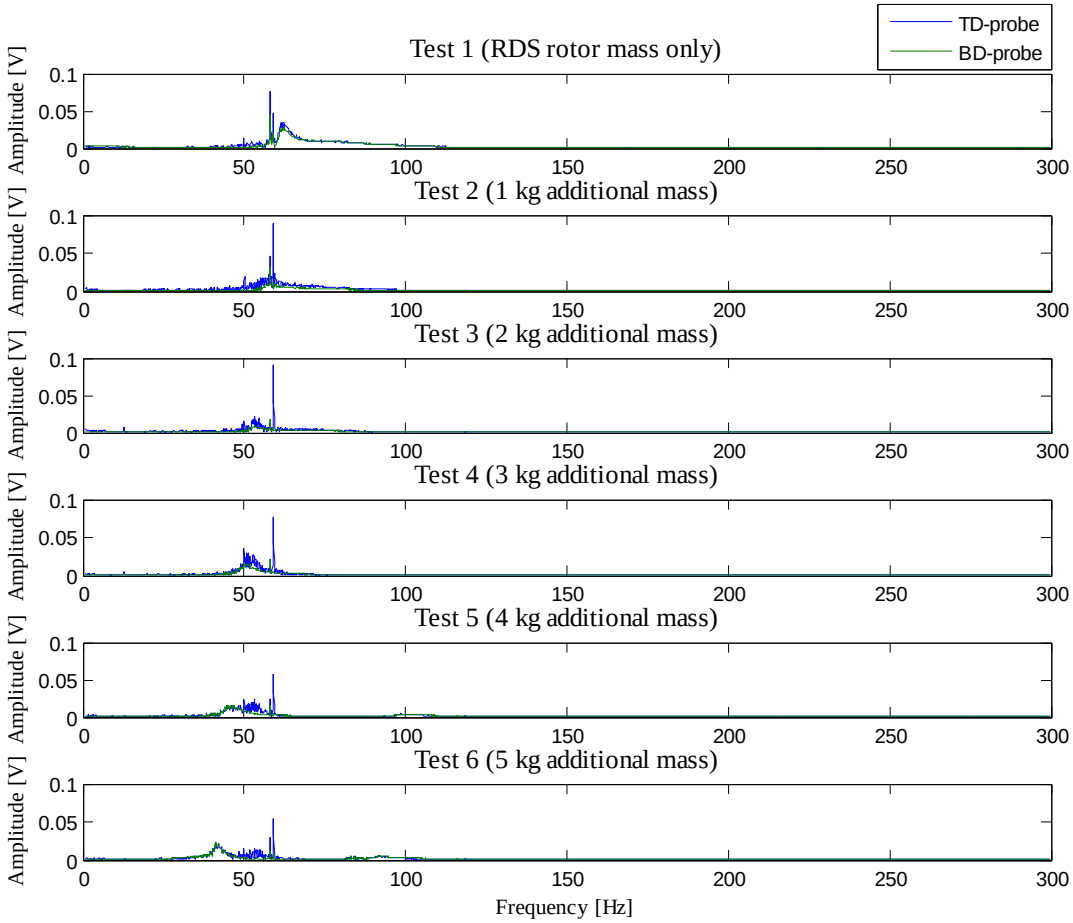

Figure 5-5: Vibration spectra of the mass variation investigation with the blue response the measurement of the TD-probe and the green response the measurement of the BD-probe

In order to identify the mode form of the excited rigid body natural frequency, the phase of the two eddy-current probes are used. Figure 5-6 illustrates the bode plot[16] of the RDS to an impulse excitation. Notice the phase difference of 3.1 radians between the two eddy-current probes at a frequency of approximately 62 Hz in Figure 5-6. This indicates that the probes are 180° out of phase implying the conical or first rigid mode of the RDS according to the simulated results of section 4.3.

The results, presented in Figure 5-4, Figure 5-5 and Figure 5-6, identified the rigid body natural frequency of the RDS for the minimum amount of damping and maximum amount of stiffness. However, this does not represent the actual operating conditions of the RDS. During operation of the RDS, the proportional and differential gain control parameters are set to the maximum. According to (5-2), the maximum limit of the differential gain control parameter will result in the maximum amount of damping in the system. An increase in damping will result in a decrease in the damped frequency. It is therefore necessary to investigate the effect of added damping on the response of the RDS.

[16] A bode plot of a system refers to the pair of plots of amplitude vs. frequency and phase vs. frequency [8].

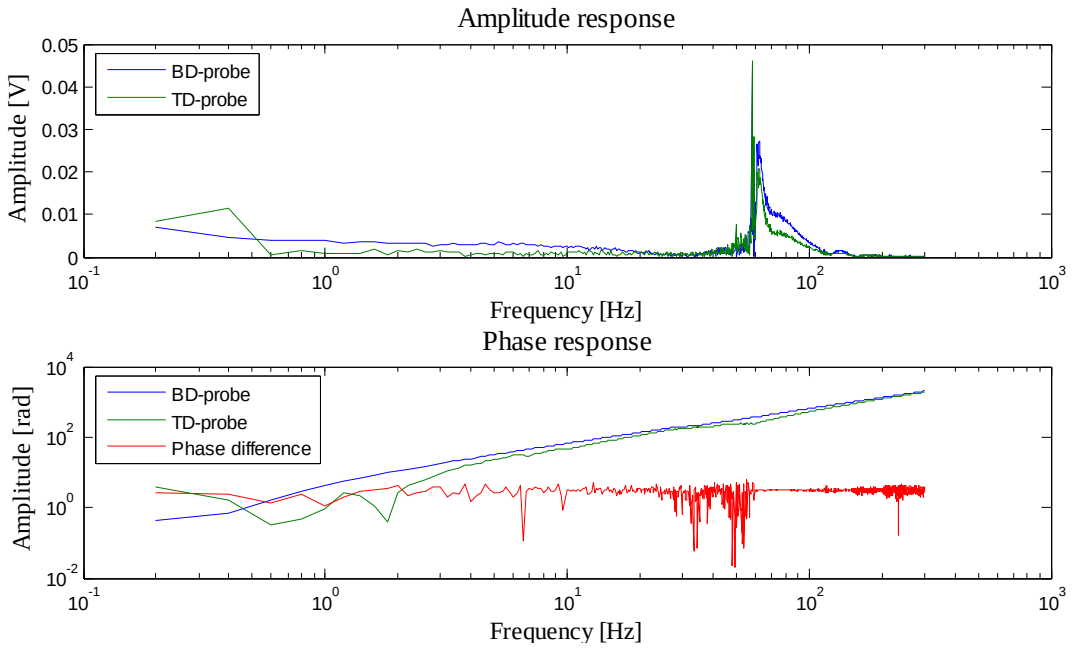

Figure 5-6: Bode plot for RDS with control parameters K_P = 20 000 and K_D = 10

The effect of damping on the response of the RDS is investigated by repeating the experimental procedure discussed in section 5.1.1 while incrementing the differential gain control parameter for each test. Table 5-3 summarises the control parameters used during the investigation.

Table 5-3: Control parameters for damping variation test setups

Test #	Proportional gain control parameter (K_P)	Differential gain control parameter (K_D)
1	20 000	10
2	20 000	14
3	20 000	20
4	20 000	26
5	20 000	30
6	20 000	34
7	20 000	40

The vibration spectra for each test was calculated in *MATLAB*®, and can be seen in Figure 5-7 and Figure 5-8 for the TD-probe and BD-probe respectively.

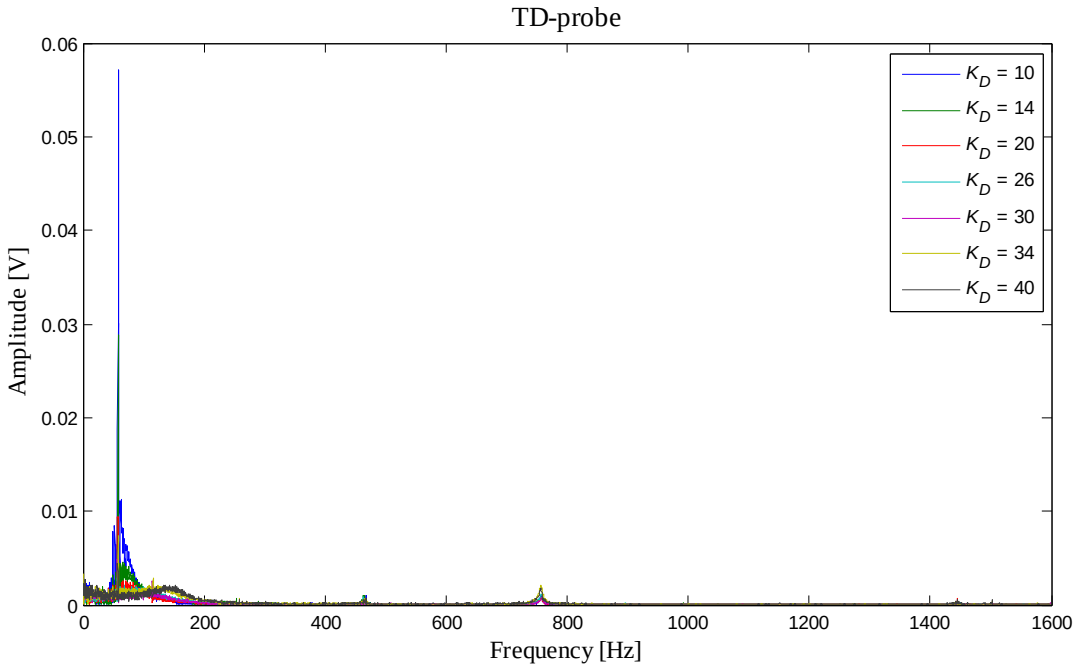

Figure 5-7: Vibration spectra of the damping variation investigation measured at TD-probe

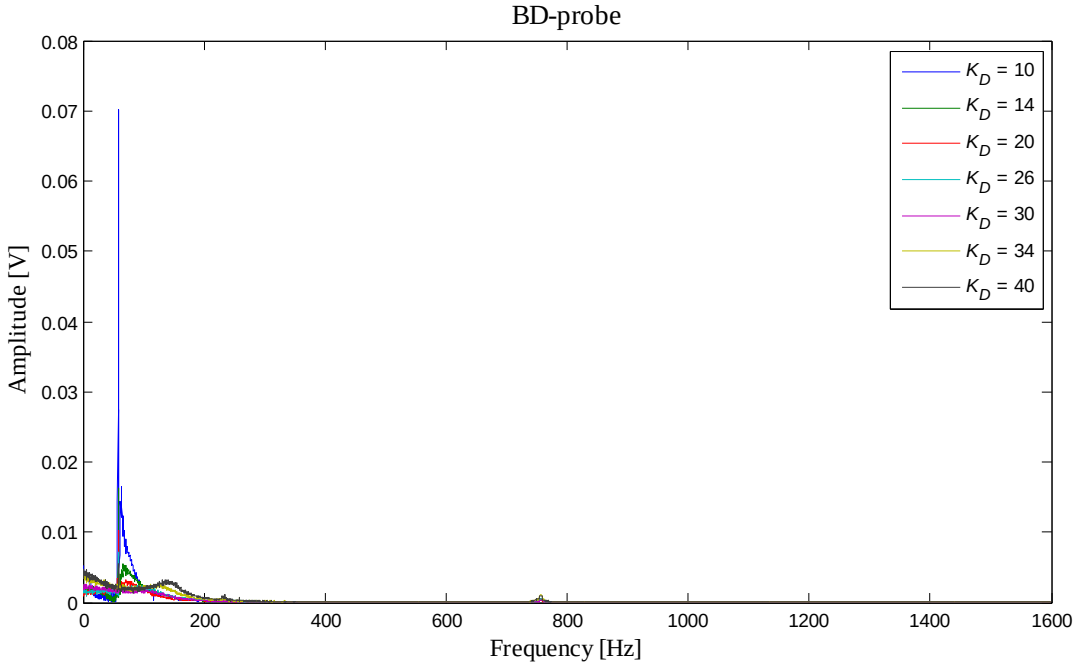

Figure 5-8: Vibration spectra of damping variation investigation measured at BD-probe

The receptance or compliance of a system is determined by taking the relation between the measured response to the excitation input [9]. As a unit impulse excitation is used to excite the RDS rotor, the response of the system illustrated in Figure 5-7 and Figure 5-8, represents the receptance of the system at the measuring stations.

It should be clear from Figure 5-7 and Figure 5-8 that variation in damping affects only the frequency-response below 400 Hz. In order to display the affect of damping variation more clearly, the vibration spectra of Figure 5-7 and Figure 5-8 is limited to 400 Hz and illustrated in Figure 5-9 and Figure 5-10 respectively.

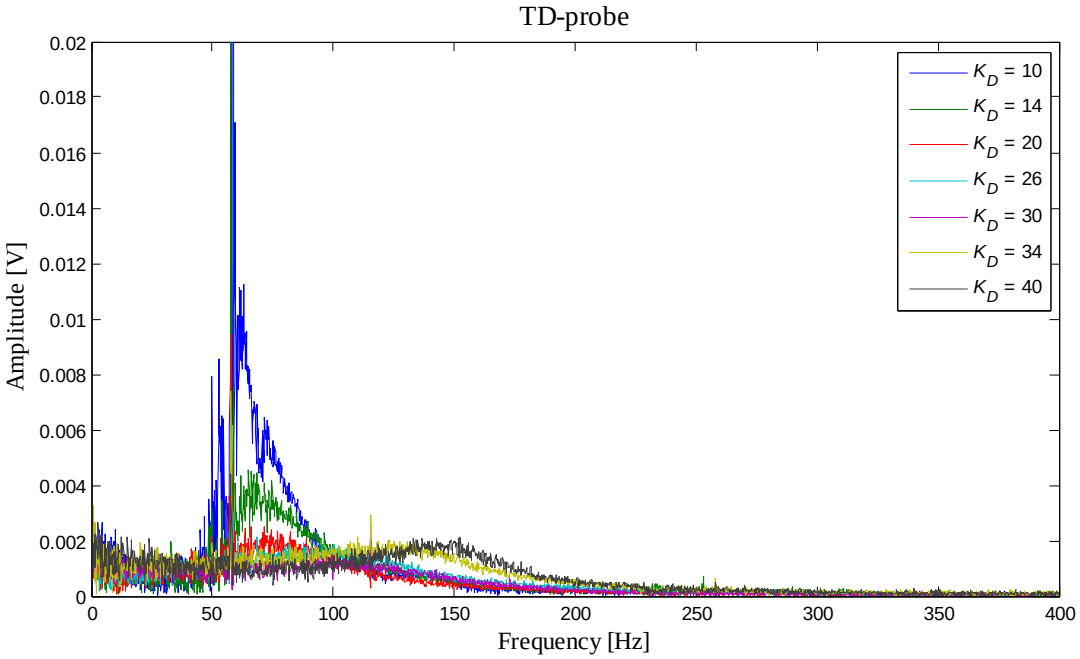

Figure 5-9: Limited vibration spectra of Figure 5-7

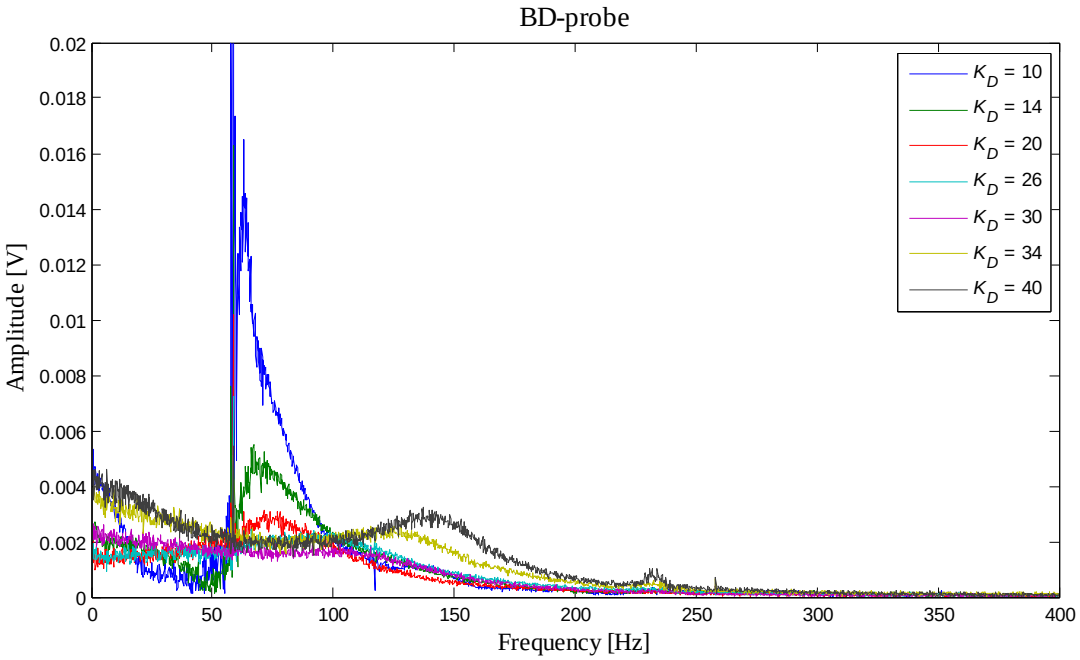

Figure 5-10: Limited vibration spectra of Figure 5-8

Figure 5-9 and Figure 5-10 shows that as the differential gain control parameter increases, the damping increases and the vibration amplitudes decrease. The damping reaches a maximum when the differential control parameter is in the vicinity of K_D = 30. For tests with the differential control parameter higher than K_D = 30, higher vibration amplitudes are noted. In order to investigate this phenomenon more thoroughly, the position data is used to determine the damping ratio for the system for each test. The damping ratio of the AMBs is determined by using the logarithmic decrement method. The position data of three tests with the differential control parameter K_D = 14, measured at the BD-probe, are illustrated in Figure 5-11.

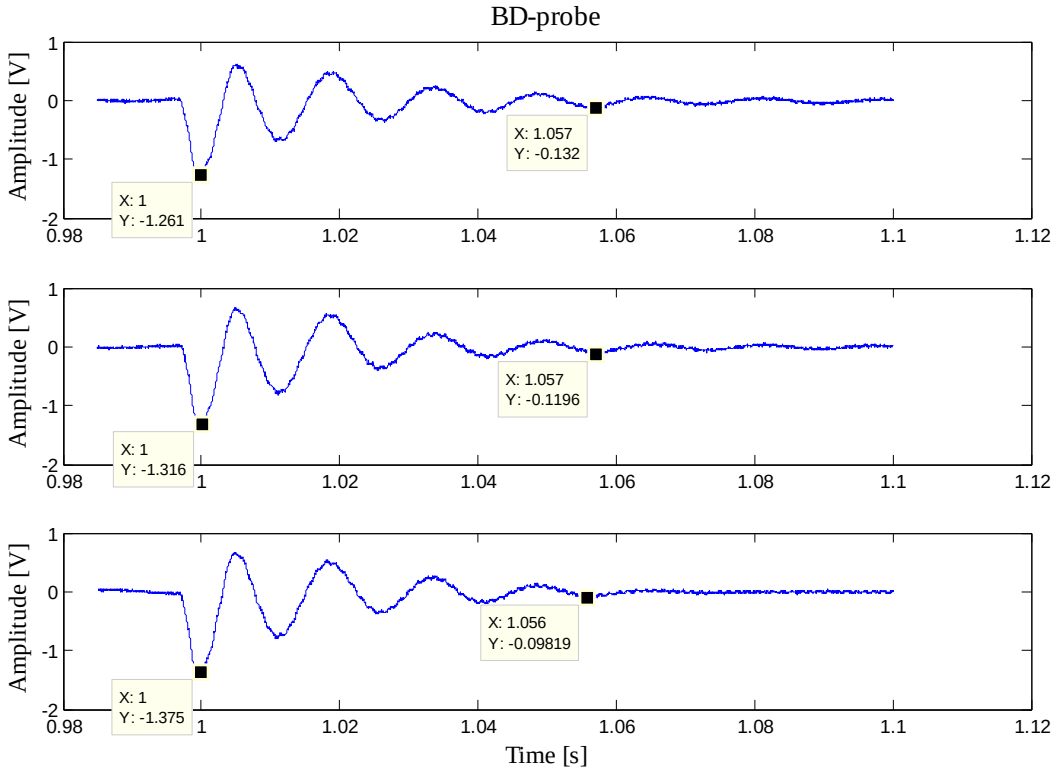

Figure 5-11: Position data for three tests measured at the BD-probe with K_D = 14

The damping of the system is determined by taking the average of the damping, calculated from each of the three tests. Five cycles are used to measure the damping as quantified in Figure 5-11. The average logarithmic decrement δ_{avg} of the three tests can be calculated as [9]:

$$\delta_{avg} = \left[\frac{1}{4}\ln\left(\frac{1.261}{0.132}\right)+\frac{1}{4}\ln\left(\frac{1.316}{0.1196}\right)+\frac{1}{4}\ln\left(\frac{1.375}{0.09819}\right)\right]/3 = 0.636846 \quad (5\text{-}3)$$

The average damping ratio, ζ_{avg}, can now be calculated as:

$$\zeta_{avg} = \frac{1}{\sqrt{1+\left(2\pi/0.636846\right)^2}} = 0.094554 \quad (5\text{-}4)$$

This technique is used to identify the average damping ratio at the TD-probe and BD-probe for each differential control parameter test. The results are summarised in Table 5-4. The average damping ratios are graphically illustrated in Figure 5-12.

Table 5-4: Average damping ratios for differential control parameter test setups measured at TD-probe and BD-probe

Differential control parameter (K_D)	ζ_{avg} measured at TD-probe	ζ_{avg} measured at BD-probe
10	0.01727	0.02200
14	0.08562	0.09455
20	0.17564	0.20733
26	0.23910	0.24481
30	0.25427	0.24254
34	0.17434	0.20921
40	0.13957	0.15527

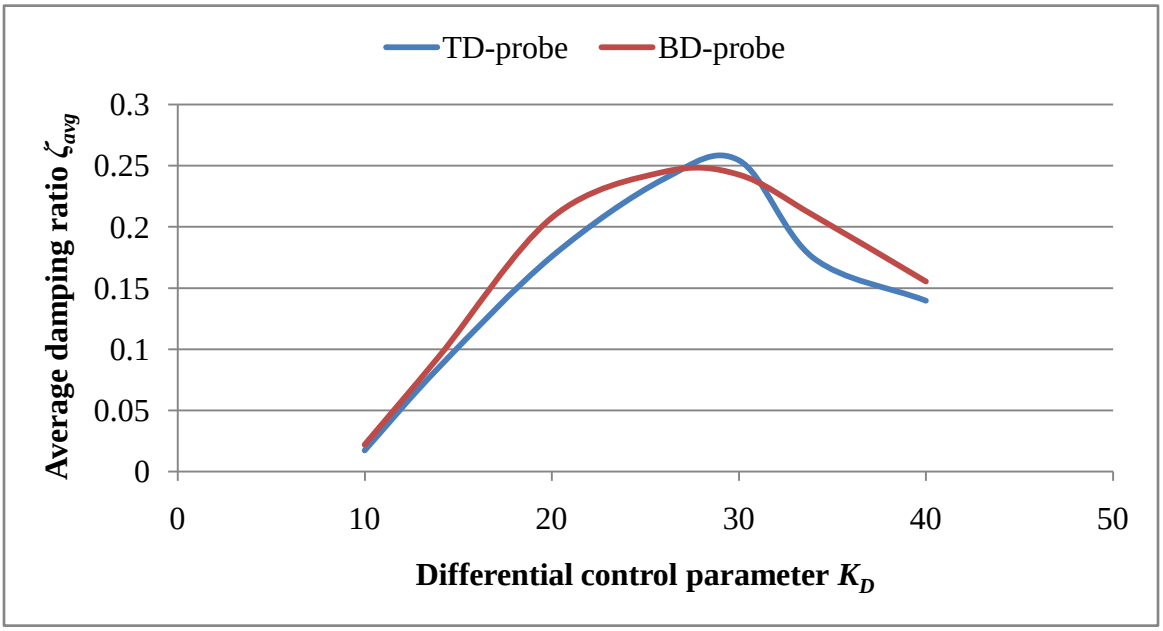

Figure 5-12: Average damping ratio ζ_{avg} as a function of differential control parameter K_d measured at the TD-probe and BD-probe

Figure 5-12 indicates that the damping ratio of the system increases as the differential control parameter increases, but only up to a maximum. This maximum value is approximately K_D = 26. For the differential control parameter higher than K_D = 26, the damping ratio decreases. This correlates with the information illustrated in Figure 5-9 and Figure 5-10. The frequency-response amplitudes increases for differential gain control parameter higher than K_D = 26. Figure 5-13 also illustrates the maximum vibration amplitude as a function of the differential control parameter measured at the TD-probe and BD-probe.

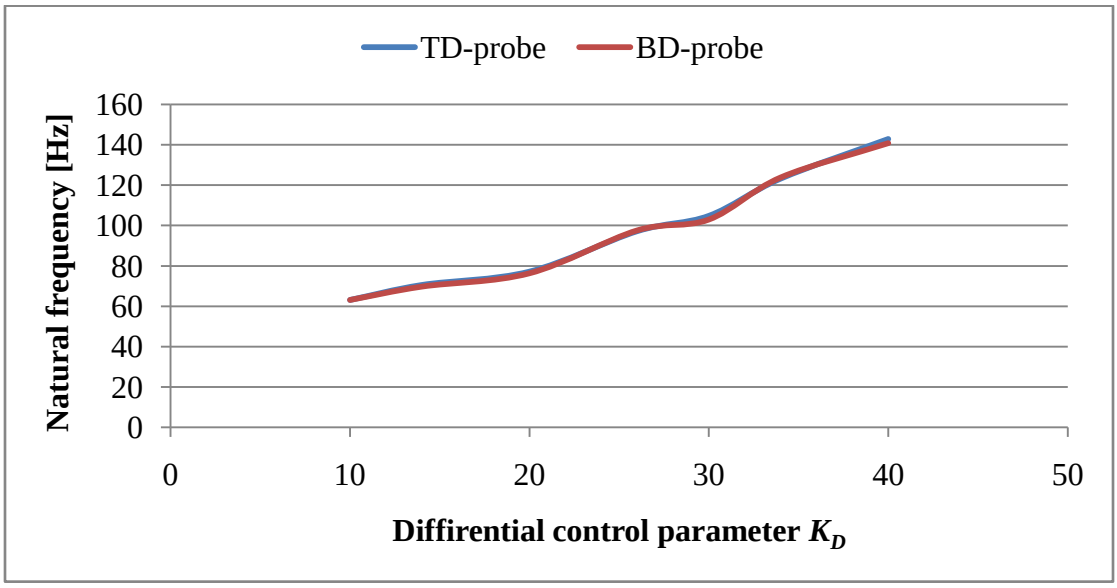

Figure 5-13: Natural frequency as a function of differential control parameter K_d measured at the TD-probe and BD-probe

It should be clear that the natural frequency originally measured at approximately 62 Hz, increases linearly to a frequency of approximately 140 Hz as the differential control parameter increases, as illustrated in Figure 5-13. This contradicts with the definition of damped frequency which should decreases as the damping increases.

In order to verify that the rigid body natural frequency, originally measured at 62 Hz, increases linearly to 140 Hz; the mode form of the natural frequency, measured at 140 Hz, is identified by using the phase difference of the probes relative to each other. The phase difference between the probes is 3.23 radians at a frequency of 140 Hz, implying that this frequency represents the conical mode. This verifies that this frequency is in fact the first rigid body natural frequency, originally measured at 62 Hz in Figure 5-6. This also verifies that added damping in the system increases the first rigid body natural frequency linearly up to a frequency of 140 Hz. This also identifies the unknown natural frequency of 140 Hz measured by [7].

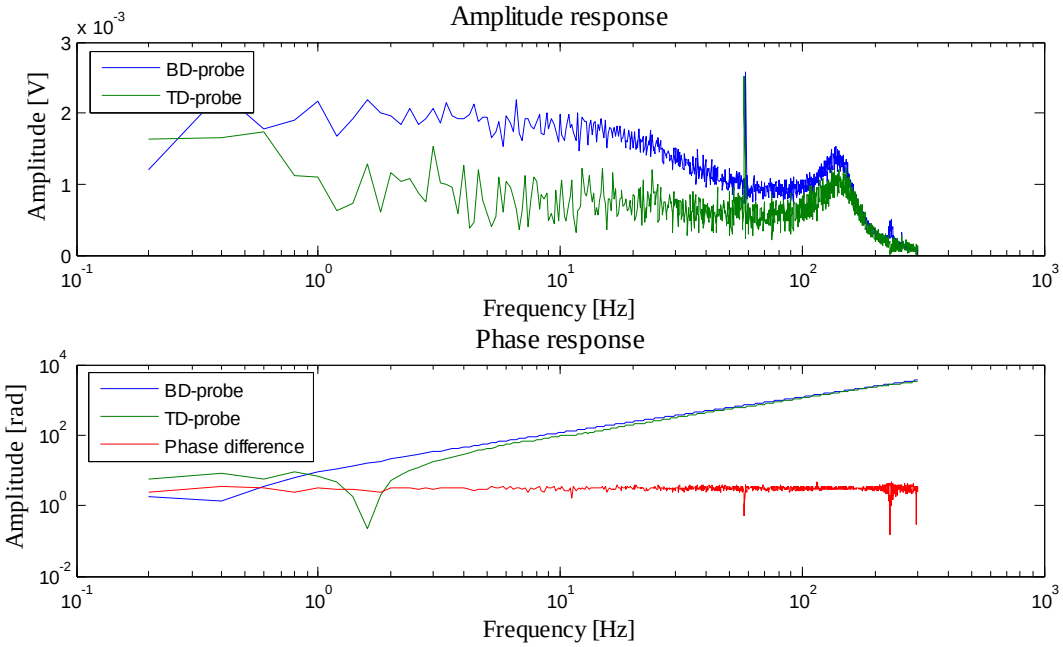

Figure 5-14: Bode plot for RDS with control parameters K_P = 20 000 and K_D = 40

5.2 Simulated rigid body natural frequencies

The simulated rigid body natural frequencies, presented in section 4.3, do not correlate with the measured rigid body natural frequency discussed in the previous section. For this reason, a critical speed map of the simulation model is constructed in the package *DyRoBeS*® and illustrated in Figure 5-15. According to Figure 5-15, the stiffness of the AMBs need to be chosen approximately 4.4E+006 N/m to simulate the first rigid body natural frequency at 62 Hz. This stiffness value does not correlate with the value chosen by [7], but does correlate with the value calculated by [18]. The rigid body natural frequencies of the model with the bearing stiffness set to 4.4E+006 N/m, are simulated in *DyRoBeS*® and illustrated in Figure 5-16(a) and Figure 5-16(b).

Figure 5-16(a) and (b) validates that the bearing stiffness of the RDS is in the vicinity of 4.4E+006 N/m. This means that the stiffness used by [7] to simulate the AMBs is inaccurate and that the stiffness of the AMBs calculated by [18] should be used when simulating the AMBs.

Notice from Figure 5-15, that both rigid body natural frequencies are presented from the critical speed analysis conducted in *DyRoBeS*®. In the previous section it was shown that only one rigid body natural frequency is excited. It should be mentioned that the critical speed analysis toolbox in *DyRoBeS*® only uses the stiffness of the bearing and rotor, and ignores the damping when simulating the natural frequencies. For this reason the model identifies the second rigid body natural frequency, even though the frequency may never be excited in the actual system.

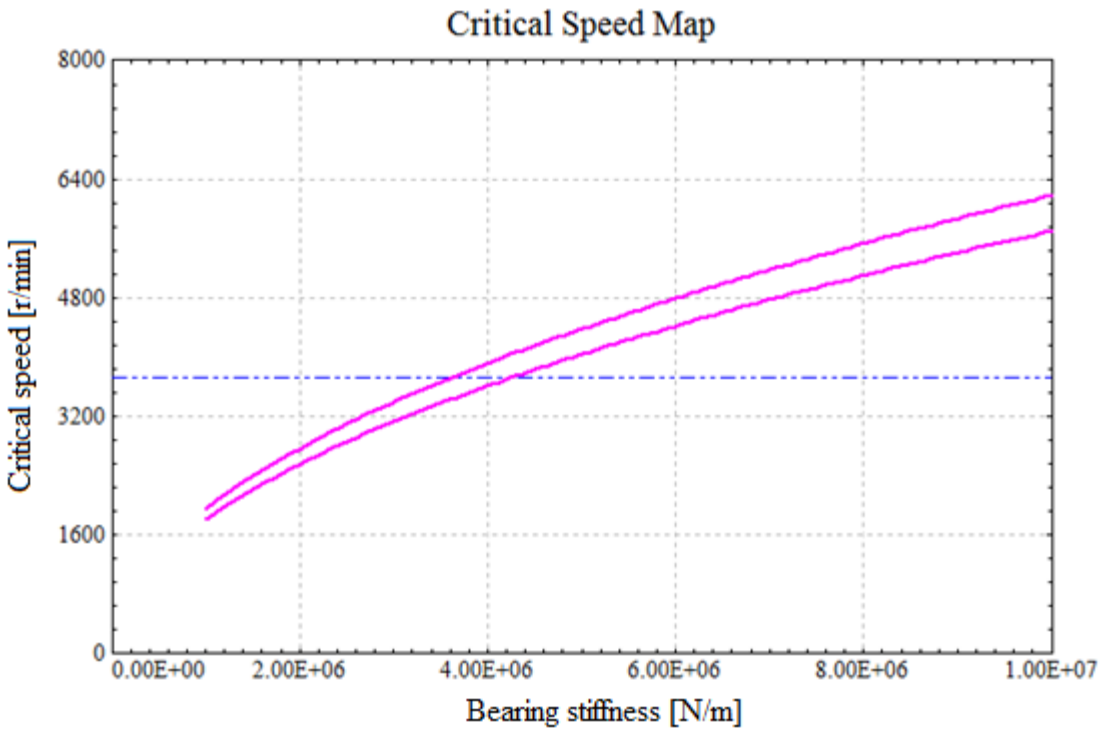

Figure 5-15: Critical speed map for the two simulated rigid natural frequencies

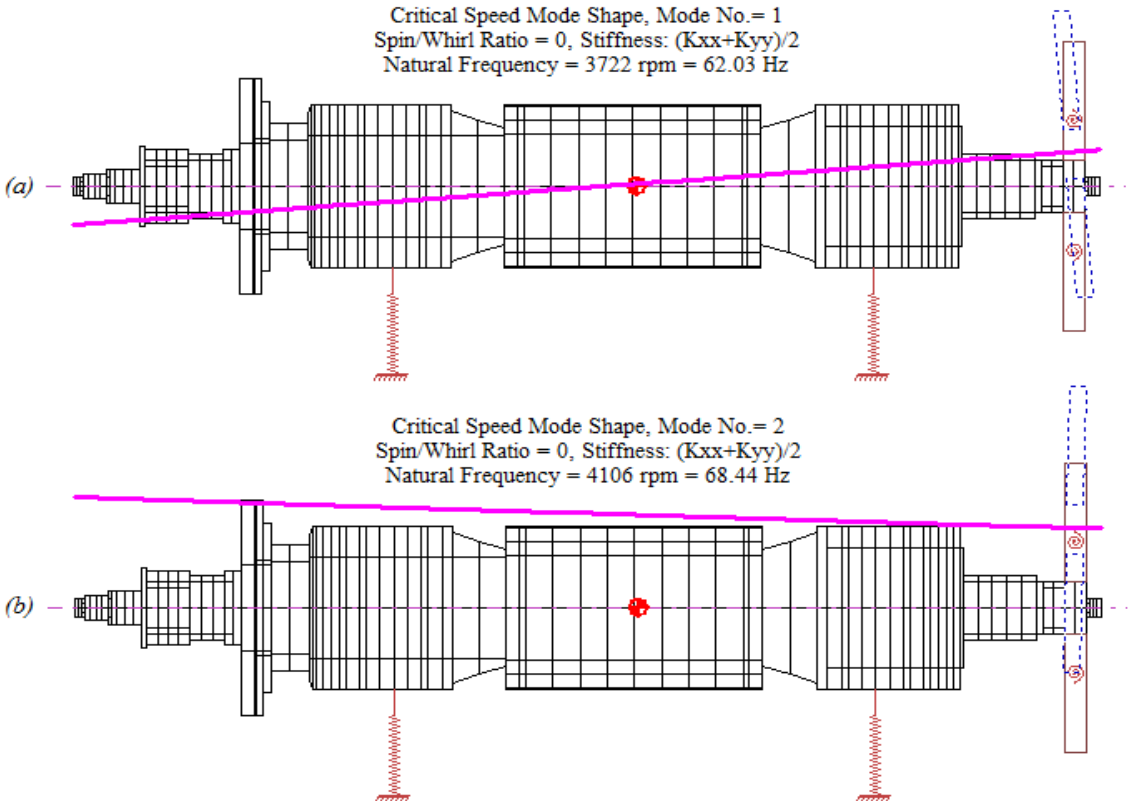

Figure 5-16: Simulated (a) first rigid natural frequency and (b) second rigid natural frequency of the RDS FE model with the bearing stiffness set to 4.4E+006 N/m

5.3 **Rotor dynamic diagnostics**

Section 2.8, critically evaluated the rotor dynamic faults associated with the RDS. It was established that a rotor crack or rotor non-circularity could be the cause of the synchronous vibration harmonics measured by [7]. In order to evaluate these two rotor dynamic faults, two hypotheses are formulated as follow:

- A rich spectrum of synchronous vibration harmonics are excited by a transverse RDS rotor crack according to [12],[13] and [3], and
- the non-circularity of the RDS rotor at the measuring positions generates foundation vibrations resulting in harmonics of the RDS rotor synchronous vibration [17].

If one of these hypotheses can be verified, it is accurate to assume that the mentioned source is the origin of the synchronous vibration harmonics. The first hypothesis is evaluated by implementing rotor orientation tests on the RDS. The second hypothesis is evaluated by identifying the orbits of the rotor at the measuring stations using the eddy-current probes.

The rotor orientation tests consists of suspending the RDS rotor with the AMBs and measuring the response of the rotor to an impulse excitation. This process is repeated while changing rotating the rotor 30° for each test. If a rotor crack exists, the response of the rotor will vary as the orientation varies.

The non-circularity tests comprise of suspending the rotor with the ADES and using the eddy-current probes to measure the air gap between the rotor and sensing interface at various rotor orientations. It should be mentioned that the ADES does not utilise the eddy-current probes for suspending the rotor. If the measured air gaps have varying orbit radii, the diameter of the rotor at the measuring positions are non-circular.

The experimental setup for both the rotor orientation tests and the rotor non-circularity tests are the same as the setup discussed in section 5.1.2. The experimental procedure is only adapted to accommodate the different orientations of the rotor.

The experimental procedure for the rotor orientation tests consists of:

- Suspend the rotor of the RDS with the AMBs by using the drive electronic system (ADES),
- rotate the rotor to the desired orientation,
- excite the rotor by hitting the blower disc of the rotor laterally with an object (preferably a plastic hammer to prevent double tapping),
- measure and capture the response of the RDS rotor with the eddy-current probes,
- calculate the FFT of each measured signal separately,
- calculate the modulus of the complex FFT values, and

- construct the vibration spectrum of the RDS by plotting the modulus of the FFT values against frequency.

The experimental procedure for the rotor non-circularity tests consists of:

- Suspend the rotor of the RDS with the AMBs by using the drive electronic system (ADES),
- rotate the rotor to the desired orientation,
- measure and capture the response of the RDS rotor with the eddy-current probes,
- calculate the dc value of each measured signal, and
- construct the orbit of the rotor at the measuring stations.

A number of twelve orientations is used to locate the rotor crack and identify the non-circularity of the rotor. This is accomplished by fitting the blower disc with a protractor and rotating the rotor 30^{o} for each repeated test. After performing all twelve tests, the rotor circulates through one revolution covering all orientations of the rotor.

5.3.1 RDS rotor crack hypothesis evaluation

The first step in the data evaluation process entails calculating the FFT of the data sampled by each eddy-current probe. This is done by using the built in FFT-function of *MATLAB*®. The vibration spectra of the orientation tests are illustrated in Figure 5-17 and Figure 5-18 for the TD-probe and BD-probe respectively.

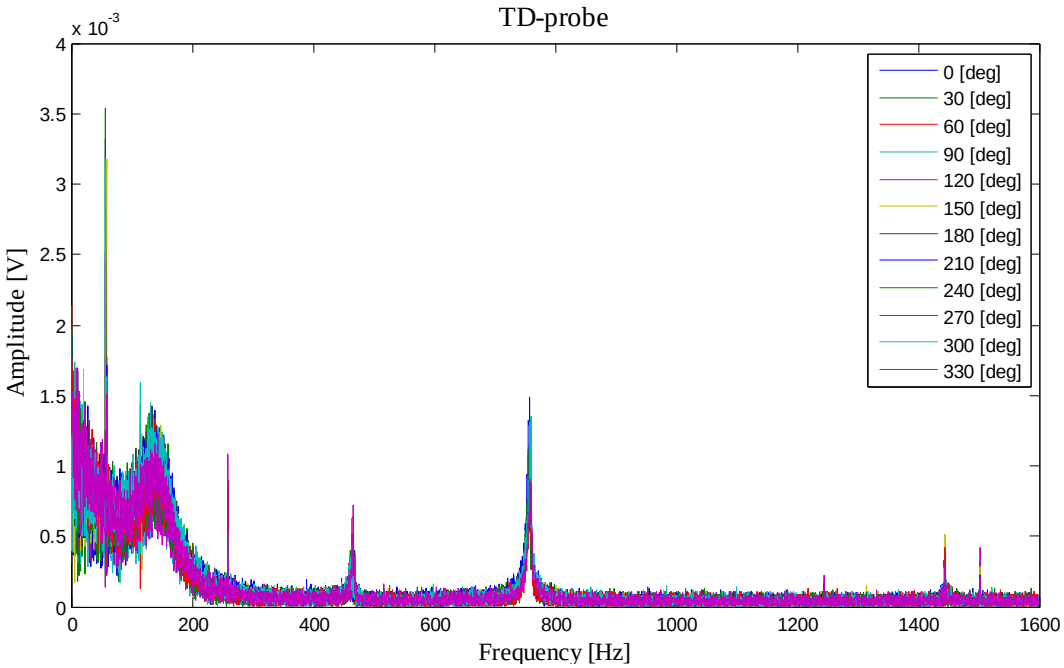

Figure 5-17: Vibration spectrum measured at the TD-probe for each orientation test

Notice from Figure 5-17 and Figure 5-18 that no significant difference is visible between the vibration spectra of any of the orientation tests. This contradicts the hypothesis stating that a transverse RDS rotor crack excites a rich spectrum of synchronous vibration harmonics. This hypothesis is thus rejected implying the second hypothesis needs to be evaluated.

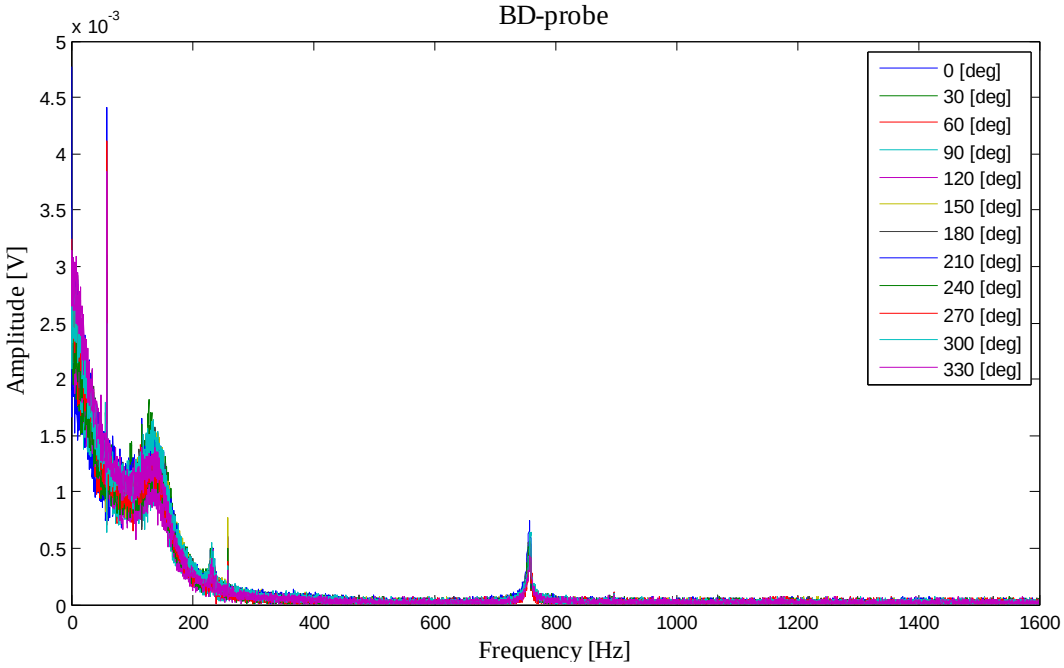

Figure 5-18: Vibration spectrum measured at the TD-probe for each orientation test

5.3.2 RDS rotor non-circularity hypothesis evaluation

The first step in the data evaluation process entails calculating the average value of the data sampled by each eddy-current probe for every rotor orientation. This is done by using the built-in "*mean*"-function in *MATLAB*®. Each rotor orientation test was repeated five times with a sample size of 150 000 readings. Table 5-5 summarises the average measurement and standard deviation of the data sampled by the TD-probe and BD-probe for twelve different rotor orientations.

Table 5-5: Average measurement and standard deviation of TD-probe and BD-probe at different rotor orientations

Orientation (˚)	TD-probe average (V)	Standard deviation (mV)	BD-probe average (V)	Standard deviation (mV)
0	-8.5357	11.0235	-7.6181	7.29875
30	-8.606	9.8668	-7.6161	7.343683
60	-8.643	9.7496	-7.6071	7.250383
90	-8.6163	10.3645	-7.61	7.220233

Orientation (˚)	TD-probe average (V)	Standard deviation (mV)	BD-probe average (V)	Standard deviation (mV)
120	-8.6366	9.7933	-7.6127	7.248567
150	-8.5464	10.09533	-7.6507	7.3638
180	-8.5676	13.61162	-7.6547	14.96582
210	-8.5359	14.231	-7.6775	15.87625
240	-8.503	10.57433	-7.6379	7.915317
270	-8.5216	10.1475	-7.5955	8.382133
300	-8.517	13.89133	-7.6072	15.59697
330	-8.5938	9.87155	-7.5868	8.301367
Overall average:	-8.568575	11.1017	-7.622858333	9.563606

The average measurements for the TD-probe and BD-probe are converted to microns (µm) by using the sensitivity of the eddy-current probes. This is done by dividing the average measurement by 7.87 mV/micron. By subtracting the overall average from the converted average measurement the data is normalised and summarised in Table 5-6.

Table 5-6: Converted and normalised measurements for the TD-probe and BD-probe at different rotor orientations

Orientation (˚)	TD-probe measurements (µm)	BD-probe measurements (µm)
0	4.177255	0.604617
30	-4.7554	0.858746
60	-9.4568	2.00233
90	-6.06417	1.633842
120	-8.64358	1.290767
150	2.817662	-3.5377
180	0.123888	-4.04596
210	4.151842	-6.94303
240	8.332274	-1.91127
270	5.968869	3.476281
300	6.553367	1.989623
330	-3.20521	4.581745

The average values (in µm) are then presented in polar form[17] against the incremented orientation (in °). In order to ease the interpretation of the polar plot, a constant value of 100 µm is added to the average values. The RDS rotor orbits at the TD-probe (blue) and BD-probe (magenta) were identified in *MATLAB*® and are illustrated in polar form (µm vs angle) in Figure 5-19 and in linear form (µm vs angle) in Figure 5-20. Note that the linear plot does not contain a constant value because the plot is easily interpreted as it is.

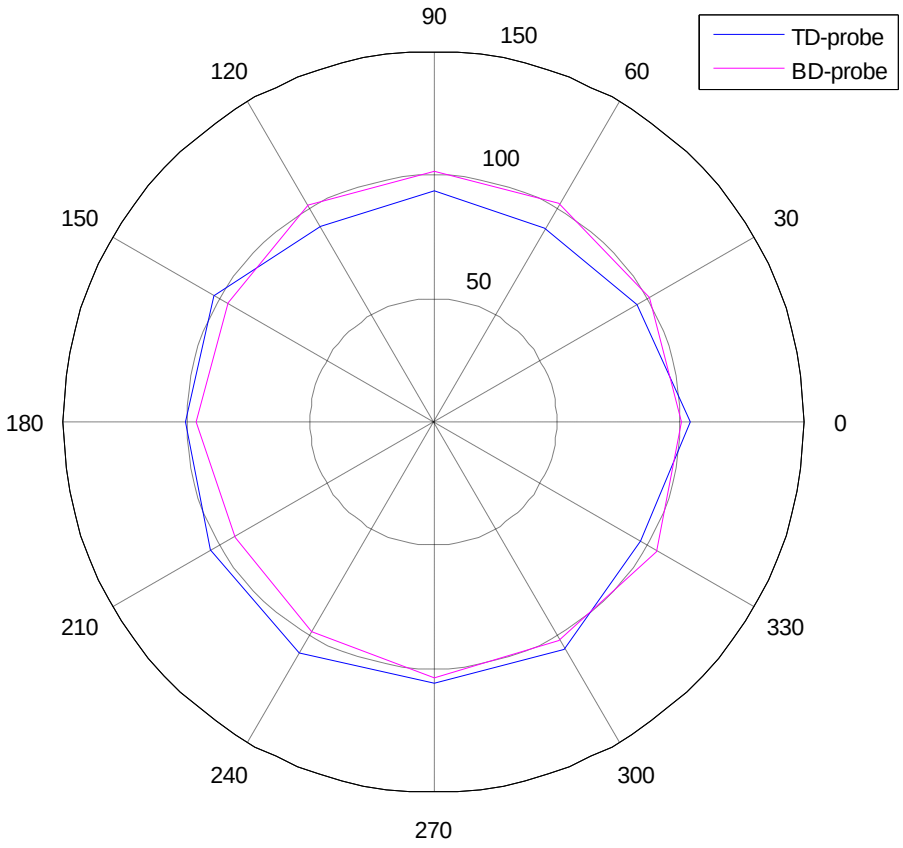

Figure 5-19: RDS rotor orbits measured at TD-probe (blue) and BD-probe (magenta) in polar form

According to Figure 5-19 and Figure 5-20, the orbits of the RDS rotor measured at the TD-probe and BD-probe do not have a constant radius. A fluctuation of approximately 17 µm at the TD-probe and 9 µm at the BD-probe is measured over one revolution of the rotor. During rotation of the rotor, the position sensors will pick up the fluctuations and the controllers will aim to compensate. This will cause the rotor to vibrate at the frequency of the fluctuating position measurements which will be directly proportional to the running speed of the rotor.

[17] A polar plot refers to a two-dimensional figure where each point on the figure is defined with a fixed distance and angle with respect to a reference point.

This supports the hypothesis: the non-circularity of the RDS rotor at the measuring positions generates foundation vibration resulting in harmonics of the RDS rotor synchronous vibration. It can thus be assumed that the synchronous vibration harmonics measured in [7], are a result of non-circularity of the rotor at the measuring stations.

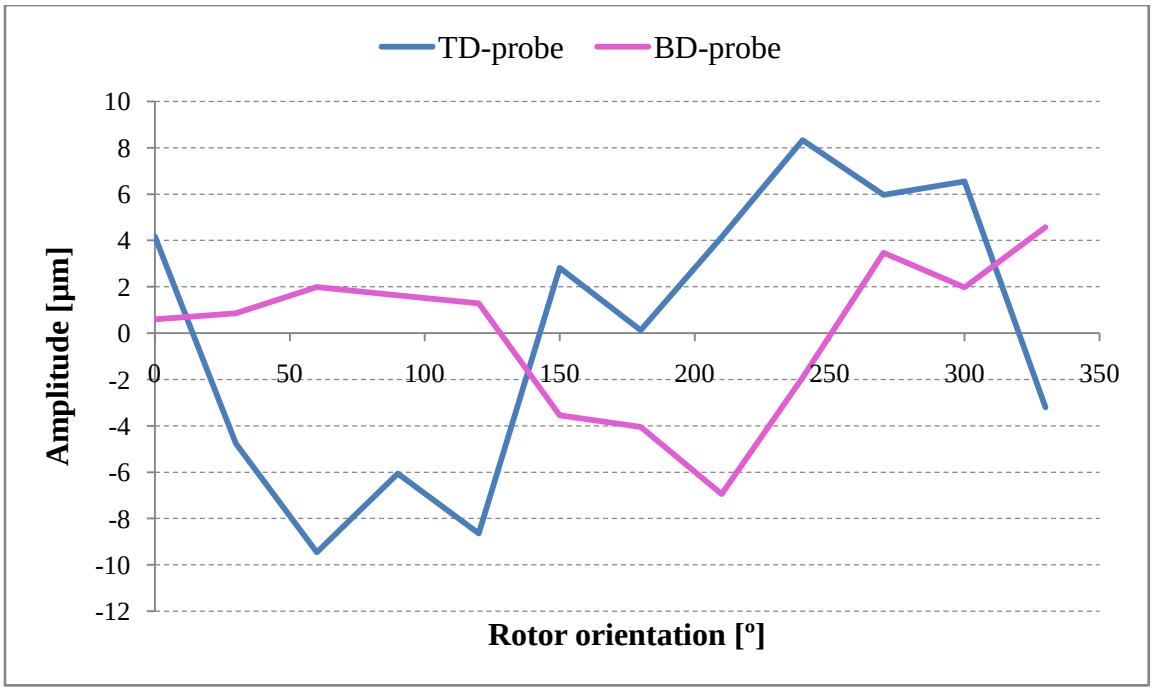

Figure 5-20: RDS rotor orbits measured at TD-probe (blue) and BD-probe (magenta) in linear form

5.4 Concluding remarks

This chapter characterized the vibrations of the integrated RDS. The bending natural frequencies of the integrated system were identified and compared to the bending natural frequencies measured in section 3.2. A difference in the frequencies were observed. It was proven that only one rigid natural frequency of the RDS, the conical mode, is excited at approximately 140 Hz. From a modal analysis process presented in section 5.1.3, it was proven that the excited rigid natural frequency originally situates at approximately 62 Hz although damping increases the natural frequency up to 140 Hz.

The difference in the simulated and measured rigid natural frequencies proved the simulation model inaccurate. A critical speed map of the simulation model proved the stiffness of the bearings used to simulate the AMBs by [7] to be inaccurate. From the critical speed map, it was established that a stiffness of 4.4E+006 N/m should be used to simulate the AMBs, because it results in good correlation with the results [18].

The two rotor dynamic faults defined in section 2.8 were investigated according to a rotor dynamic diagnostic process. Two hypotheses were formulated and tested. It was established that no RDS rotor cracks exist and that non-circularity of the RDS rotor at the measuring stations is the cause of the synchronous vibration harmonics measured by [7].

This chapter characterized the integrated system vibrations of the RDS. The next chapter concludes this dissertation with conclusions made from the results obtained throughout the dissertation and provides recommendation for further research.

Chapter 6 Conclusions and recommendations

This chapter concludes this dissertation with an overview of the conclusions drawn from the results presented in the previous chapters with reference to the problem statement formulated in section 1.2. Shortfalls associated with the research investigation are presented and discussed. Recommendations and proposed solutions are given based upon the experience gained during the research investigations. A concluding statement ends the chapter.

6.1 Conclusions

The problem statement formulated in section 1.2 stated that the purpose of the project was the vibration characterization of an active magnetic bearing supported rotor system. Emphasis was placed on characterizing the natural response of the RDS rotor, stator and integrated system. This led to a number of research objectives defined in section 1.3. The scientific methods used to investigate, validate and verify the research objectives were presented in Chapter 3 through Chapter 5.

The main research focus during the vibration characterization of the RDS was placed on:

- A rotor and stator characterization process,
- an integrated system characterization process, and
- a rotor dynamic diagnostic process.

Overall the natural frequencies and rotor dynamic phenomena were successfully characterized and validated. Various discrepancies and unexplained phenomena arose from the empirical and numerical procedures used to verify and validate the scientific methods. Valuable insight was gained which will streamline vibration characterization processes in the future. The following sub-sections present conclusions on these discrepancies and unexplained phenomena.

Rotor and stator characterization

The geometric measurements and material densities of the RDS rotor were validated in section 3.1.1 and 3.1.2. The experimentally identified material density of M270-35A presented a significant error when compared to the documented density. This is due to the thickness deviations of the sheets during manufacturing. This results in different material densities for each of the sheets. An error is thus most likely to be encountered when comparing the experimental density to the documented density. The modulus of elasticity of the materials could not be validated due to instrumentation and budget constraints.

In sections 3.2 and 3.3 two modal analysis processes were presented to identify the bending natural frequencies of the RDS rotor and stator as well as the mode forms of the RDS rotor. The modal analysis processes successfully validated the RDS rotor and stator bending natural frequencies although insufficient data was available to accurately validate the mode forms of the RDS rotor. This can be explained by the results from the FE simulation model.

A FE simulation model of the RDS rotor was presented in section 4.3. The model was successfully verified in terms of rotor lateral stiffness and bearing stiffness and validated in terms of the bending natural frequencies of the RDS rotor. The model also identified that insufficient measuring stations were located on the RDS rotor during the modal analysis. The experimental setup of the rotor modal analysis illustrated in Figure 3-4 located the last measuring station to the inside of the blower disc. Measuring the difference in phase angle to the outside of the blower disc was thus impossible. This was verified with the correlation between the simulated and measured mode form slopes for the first two bending natural frequencies illustrated in Figure 4-10 and Figure 4-11.

The findings of [7], stated that the natural frequency measured at approximately 471 Hz was a blower disc natural frequency and that the first bending natural frequency of the RDS rotor is situated at a frequency of approximately 778 Hz. This proved to be inaccurate. It was validated in section 3.2 that the 443.33 Hz natural frequency is in fact a lateral natural frequency. It was also proven with Figure 4-10 that this natural frequency is the first bending natural frequency. Figure 4-11 showed that the natural frequency measured at 774.09 Hz is the second bending natural frequency of the RDS rotor. The difference between the corresponding natural frequencies measured by [7] and identified in section 3.2 is due to the thrust runner being excluded from the modal analysis process.

Integrated system characterization

Section 5.1 presented several modal analysis processes used to identify and validate the rigid body natural frequencies of the integrated RDS. The modal analysis processes successfully identified the integrated RDS natural frequencies, even though unexplained phenomena were noted.

The modal analysis processes proved that for the system with minimum damping, only one rigid body natural frequency was excited at approximately 62 Hz. The other rigid body natural frequency disappeared due to sufficient internal damping of the system. A bode plot of the response of the system to an impulse excitation identified the excited rigid body natural frequency to be from the conical mode. A dominant frequency component was also measured at 59 Hz. This frequency was proven to be of non-mechanical form.

From a modal analysis process implementing incremented differential gain control parameters on the system, it was observed that the excited rigid body natural frequency increases linearly up to a maximum frequency of approximately 140 Hz. This characterized the unaccounted for natural frequencies mentioned in [7]. The damping of the AMBs also increased as the differential gain control parameter increased up to a maximum where after the damping decreased again. These phenomena cannot be explained at this moment.

From a critical speed map presented in section 5.2, it was pointed out that the stiffness of the bearings used to simulate the AMBs by [7] was an inaccurate approximation. According to the critical speed map illustrated in Figure 5-15, the stiffness value of the AMBs calculated by [18] is an acceptable approximation of the stiffness.

Rotor dynamic diagnostics

Two hypotheses defining the origins of the synchronous vibration harmonics were formulated in section 5.3. The first hypothesis stating that: a rich spectrum of synchronous vibration harmonics are excited by a transverse RDS rotor, was proven to be false according to an experimental investigation presented in section 5.3.1. The second hypothesis stating that: the non-circularity of the RDS rotor at the measuring positions generates foundation vibrations resulting in harmonics of the RDS rotor synchronous vibration was proven true according to an experimental investigation presented in section 5.3.2.

From the experimental investigation it was shown that the orbit of the rotor at the measuring station is non-circular. This results in base vibrations on the unbalance response of the rotor producing multiple components of the running speed vibration according to Table 2-3. For this reason it is acceptable to identify the origins of the synchronous vibration harmonics as being due to the non-circularity of the RDS rotor.

6.2 **Recommendations and future work**

Recommendations to improve the outcomes of the dissertation as well as proposed future work are discussed in this section.

Rotor and stator characterization

Future work on the characterization of the RDS rotor bending natural frequencies are recommended to experimentally validate the mode forms of the bending natural frequencies. This can be done by repeating the rotor modal analysis presented in section 3.2, with one of the stationary accelerometers mounted on the outside of the blower disc.

Integrated system characterization

From the modal analysis process implementing various differential gain control parameters on the system, a number of unexplained phenomena arose that ensures opportunity for future work.

The first issue is the excited rigid body natural frequency that linearly increased as the differential gain control parameter increased. As a starting point, it is recommended that the stiffness of the AMBs is evaluated as a function of the differential gain control parameter.

The second issue is the damping of the AMBs that increased to a maximum and then decreased again for an increase in the differential gain control parameter. This phenomenon creates an investigation opportunity into the mechanical characteristics influenced by the controller of the AMBs.

Finally, there is an issue relating to the inaccurate stiffness approximation of the AMBs. It is recommended that the stiffness of the AMBs is determined from an experimental investigation. This can be done by suspending the rotor and applying a known force load to the rotor while measuring the deflection of the rotor at the AMBs.

Rotor dynamic diagnostics

From the evaluation of the hypotheses formulated in section 5.3, it was established that non-circularity of the RDS rotor at the measuring stations is the origin of the synchronous vibration harmonics measured during operation. It is recommended to verify this hypothesis with further research.

6.3 **Closure**

The focus of this research project was the vibration characterization of an active magnetic bearing supported rotor. Emphasis was placed on characterizing the natural response of the RDS rotor, stator and integrated system. The natural frequencies of the RDS rotor, stator and integrated system were successfully characterized.

The unaccounted for natural frequency of 140 Hz identified in [7], was also characterized. A FE simulation model of the RDS was presented in the computer software package known as *DyRoBeS*®. The model pointed out the inability of the experimental modal analysis used to identify the mode forms of the RDS rotor bending natural frequencies.

This research project formed an integral part in the successful vibration characterization of AMB supported rotor systems. It produced several modal analysis processes that assist in vibrational analysis of rotor-bearing systems as well as a process assisting in the development of a reliable simulation model of

AMB supported rotor systems. These processes can also be used for various rotor-bearing systems to verify and validate rotor dynamic phenomena.

A great knowledge base has been formed in the field of vibration characterization at the McTronX research group. Although the characterization processes presented in this project have some shortcomings and may be optimised, the scientific approach implemented to formalise and address the problem statement was successful.

Appendix A

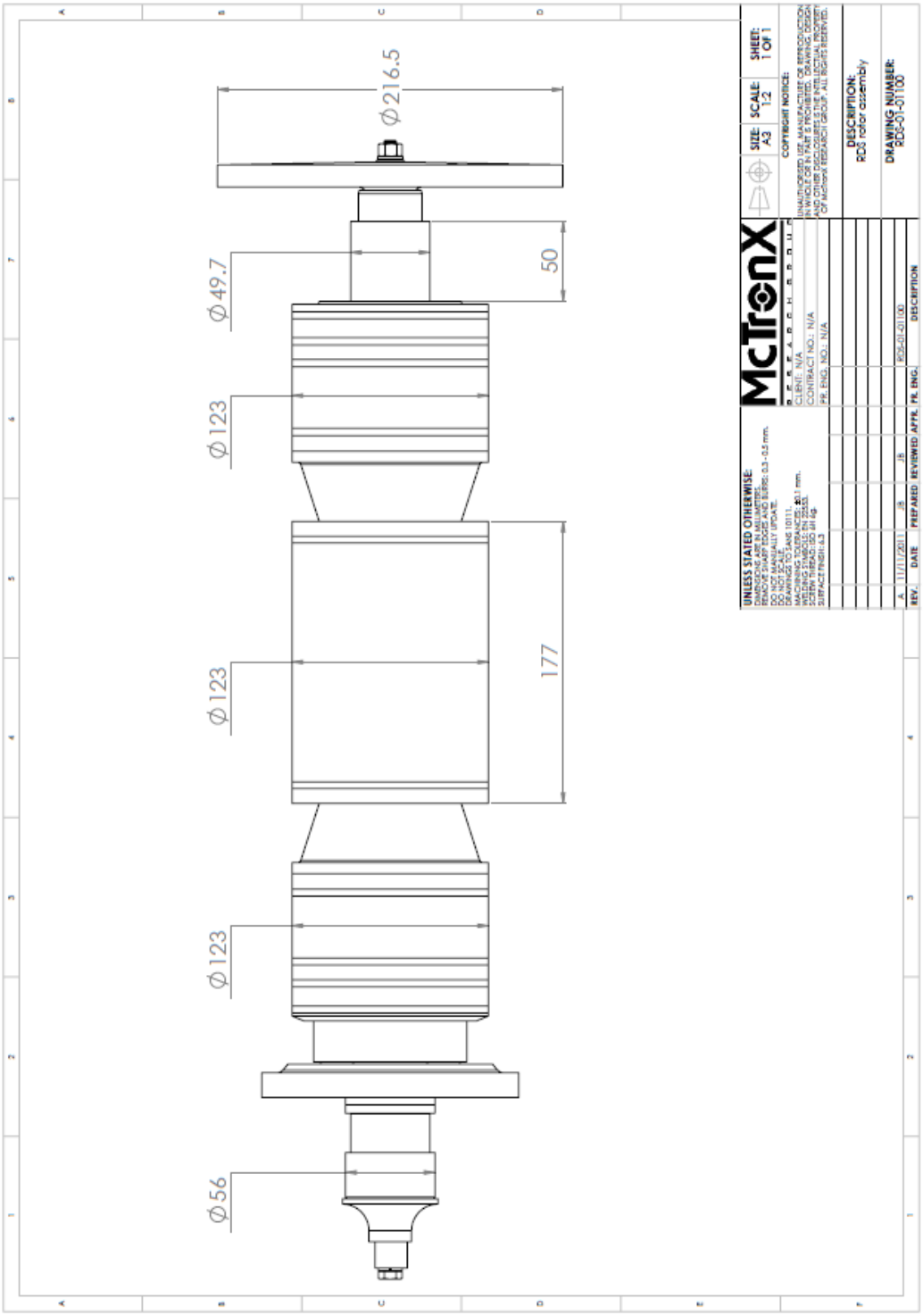
Ø216.5
50
Ø49.7
Ø123
Ø123
177
Ø123
Ø56
McTronX
RESEARCH GROUP
SIZE: A3
SCALE: 1:2
SHEET: 1 OF 1
COPYRIGHT NOTICE:
UNAUTHORIZED USE, MANUFACTURE OR REPRODUCTION OF THIS DRAWING IS PROHIBITED BY LAW AND OTHER DEALINGS ARE SUBJECT TO INTELLECTUAL PROPERTY OF McTronX RESEARCH GROUP. ALL RIGHTS RESERVED.
DESCRIPTION:
RD0 rotor assembly
DRAWING NUMBER:
RD0-01-01100
UNLESS STATED OTHERWISE:
REMOVE SHARP EDGES AND BURRS: 0.3 - 0.5 mm.
DO NOT MANUALLY UPDATE.
DO NOT SCALE DRAWING
MACHINING TOLERANCES: ±0.1 mm.
SCREW THREADS ISO 68
SURFACE FINISH: 6.3
CLIENT: N/A
CONTRACT NO.: N/A
PR. ENG. NO.: N/A
REV. DATE PREPARED REVIEWED APPR. PR. ENG. DESCRIPTION
A 11/11/2011 JB JS RD0-01-01100

Data CD

The following appendixes can be found on the attached data CD.

Appendix B

Contains the documented geometric sketches of the RDS rotor as well as a complete *SolidWorks*® model of the RDS.

Appendix C

Contains the data sheets of the accelerometers, eddy-current probes and RDS materials as well as the *MATLAB*® program codes used to evaluate the data.

Appendix D

Contains the three different FE *DyRoBeS*® models as well as the model summaries.

Bibliography

[1] Singiresu S Rao, *MECHANICAL VIBRATIONS*, 4th ed., Marcia J Horton, Ed. New Jersey, United States of America: Pearson Prentice Hall, 2004.

[2] Douglas E Adams. (2002, November) College of Engineering, Purdue University. [Online]. https://engineering.purdue.edu/FEND2/research_doc/notes_71802.pdf

[3] JR. Maurice L. Adams, *Rotating Machinery Vibration: From Analysis To Troubleshooting*, 1st ed., L L Faulkner, Ed. New York, United States of America: Crc Press, 2001.

[4] Clive L Dyn and J P Den Hartog. (2007) AccessScience, ©McGraw-Hill Companies. [Online]. http://accessscience.com/content/Mechanical%20vibration/412200

[5] Benjamin Crowell. (2011, August) lightandmatter. [Online]. http://www.lightandmatter.com/html_books/me/ch09/ch09.html

[6] Gerhard Shweitzer, Hannes Bleuler, and Alfons Traxler, *Active Magnetic Bearings: Basics, Properties and Applications of Active Magnetic Bearings*, 1st ed. Zürich, Switzerland: Authors reprint, 2003.

[7] N Bessinger, The adaption of a rotor for active magnetic bearing levitation and the corresponding auxiliary bearing design, November 2009, Masters' dissertation.

[8] Jan J Janse van Rensburg, Development of a flywheel energy storage system - Uninterrupted power supply (FLY-UPS), December 2007, Masters' dissertation.

[9] Frank Kreith, *Vibration and Shock Handbook*, Clarence W de Silva, Ed. Boca Raton, United States of America: Taylor & Francis Group, 2005.

[10] John M Vance, *Rotordynamics of Turbomachinery*. New York, Unitred States of America: John Wiley & Sons, 1988.

[11] A. V. Ruddy, "ROTOR DYNAMICS OF TURBO-MACHINERY," *INDUSTRIAL LUBRICATION AND TRIBOLOGY*, no. March/April, March 1984.

[12] Paresh Girdhar and Cornelius Scheffer, *Machenery Vibration Analysis & Predictive Maintenance*,

Cornelius Scheffer, Ed. Burlington, United States of America: ELSEVIER, 2004.

[13] Agnieszka Muszynska, *Rotordynamics*, L L Faulkner, Ed. Boca Raton, United States of America: Taylor & Francis Group, 2005.

[14] Erik Swanson, Chris D Powell, and Sorin Wiessman, "A Practical Review of Rotating Machinery Critical Speeds and Modes," *SOUND AND VIBRATION*, vol. 39, no. 5, pp. 11-12, May 2005.

[15] Wen J Chen and Edgar J Gunter, *Introduction to Dynamics of Rotor-Bearing Systems*. Victoria, BC, Canada: Trafford Publishing, 2005.

[16] Hamilton Horth Mabie and Fred W. Ocvirk, *MECHANISMS AND DYNAMICS OF MACHINERY*, 3rd ed. Virginia, United States of America: John Wiley & Sons, 1987.

[17] Vernon Helmut Habermann, Maurice Brunet, and Jacques LeClere, "RADIAL DISPLACEMENT DETECTOR DEVICE FOR A MAGNETIC BEARING," Device 4,114,960, January 31, 1977.

[18] Rikus R Le Roux, An embedded controller for an active magnetic bearing and drive electronic system, November 2009, Masters' dissertation.

[19] Dennis H Shreve. (1995, November) IRDBalancing. [Online]. http://www.irdbalancing.com/downloads/SIGCOND2_2.pdf

[20] Anon. (S.A.) C. D. Wälzholz. [Online]. http://www.cdw.de/Products/Electrical%20steel%20strip/1_331.html

[21] Robert C Juvinall and Kurt M Marshek, *Fundamentals of Machine Component Design*, 4th ed., Joseph Hayton et al., Eds. United States of America: John Wiley & Sons, 2006.

[22] Robert W Fitzgerald, *MECHANICS OF MATERIALS*, 2nd ed. Reading, Massachusetts, United States of America: Addison-Wesley, 1982.

[23] E.O. Ranft, "REPORT NO. RDS-01-01240-715-02," McTronX Research Group, Potchefstroom, RDS AMB Designs McTronX, 2009.

[24] Eugén O Ranft, The Development of a Flexible Rotor Active Magnetic Bearing System, May 2005, Masters' dissertation.